Destruction of Invariant Tori in Volume-Preserving Maps

by

Adam M. Fox

B.S., University of Vermont, 2007

M.S., University of Colorado at Boulder, 2011

A thesis submitted to the

Faculty of the Graduate School of the

University of Colorado in partial fulfillment

of the requirements for the degree of

Doctor of Philosophy

Department of Applied Mathematics

2013

This thesis entitled:
Destruction of Invariant Tori in Volume-Preserving Maps
written by Adam M. Fox
has been approved for the Department of Applied Mathematics

James D. Meiss

Professor Juan Restrepo

Date

The final copy of this thesis has been examined by the signatories, and we find that both the content and the form meet acceptable presentation standards of scholarly work in the above mentioned discipline.

Fox, Adam M. (Ph.D., Applied Mathematics)

Destruction of Invariant Tori in Volume-Preserving Maps

Thesis directed by Professor James D. Meiss

Invariant rotational tori play an important role in the dynamics of volume-preserving maps. When integrable, all orbits lie on these tori and KAM theory guarantees the persistence of some tori upon perturbation. When these tori have codimension-one they act as boundaries to transport, and therefore play a prominent role in the global stability of the system. For the area-preserving case, Greene's residue criterion is often used to predict the destruction of tori from the properties of nearby periodic orbits. Even though KAM theory applies to the three-dimensional case, the robustness of tori in such systems is still poorly understood. This dissertation begins by extending Greene's residue criterion to three-dimensional, reversible, volume-preserving maps.

The application of Greene's residue criterion requires the repeated computation of periodic orbits, which is costly if the system is nonreversible. We describe a quasi-Newton, Fourier-based scheme to numerically compute the conjugacy of a torus and demonstrate how the growth of the Sobolev norm or singular values of this conjugacy can be used to predict criticality. We will then use this method to study both reversible and nonreversible volume-preserving maps in two and three dimensions. The near-critical conjugacies, and the gaps that form within them, will be explored in the context of Aubry-Mather and Anti-Integrability theory, when applicable. This dissertation will conclude by exploring the locally and globally most robust tori in area-preserving maps.

Dedication

For my parents, whose love and support never wavered,

and my brother, who taught me to love math and science.

Acknowledgements

This dissertation would not have been possible without the support of my advisor and mentor, Professor James Meiss. He has been an exceptional resource, providing continual guidance throughout my graduate career. I am in his debt.

I am also very grateful to Elizabeth Bradley, James Curry, Keith Julien, and Juan Restrepo for their service on my doctoral committee and assistance throughout the dissertation process. Dr. Julien was also extremely helpful in identifying and correcting the aliasing errors.

There are many others who contributed to this dissertation. Rafael de la Llave, Renato Calleja, Gemma Huguet, Holger Dullin, Hector Lomelí, and Robert Easton all provided invaluable advice and suggestions. My brother, Daniel Fox, regularly shared his expertise in the C-programming language. Their assistance was invaluable.

Finally, I would like to thank my friends and family for their support and encouragement.

Contents

Chapter

Tables

Table

Figures

Figure

Chapter 1

Introduction

A dynamical system consists of a state space M along with a rule f that describes the evolution of any point in that space with respect to time. The nature of the system is largely dependent upon the time variable. When time is continuous, the evolution rule f is generally expressed by a system of differential equations. Hamiltonian flows, for example, are defined on the canonical coordinates (p, q) as

$$\dot{q} = \frac{\partial H}{\partial p} \qquad\qquad \dot{p} = -\frac{\partial H}{\partial q} \tag{1.1}$$

where the Hamiltonian $H(p, q, t)$ corresponds to the total energy in the system. Alternatively, when time is a discrete variable, the evolution of the system is described by a map,

$$x' = f(x).$$

Discrete systems are in many ways simpler than continuous ones; most notably, they do not require the solution of a system of differential equations. Maps are also more general as every continuous system induces a discrete one through a stroboscopic map or Poincaré section.

We will consider families of real analytic maps f_ε on $M = \mathbb{T}^d \times \mathbb{R}^k$ of the form

$$\begin{aligned} x' &= x + \Omega(z) - \varepsilon h(x, z, \varepsilon) \mod 1, \\ z' &= z - \varepsilon g(x, z, \varepsilon). \end{aligned} \tag{1.2}$$

where x are period-one **angle** variables and the z coordinates represent the **action**. It is often convenient to **lift** this map from M to $\mathbb{R}^d \times \mathbb{R}^k$. A suitable lift F_ε can be obtained by removing the mod 1 from (1.2).

We will further restrict our inquiry to invertible maps of the form (1.2) that preserve the standard Euclidean volume form; the preimage of every set has the same volume as the original set. An important consequence of this property is that whenever f_ε is differentiable the Jacobian matrix

$$Df_\varepsilon = \begin{pmatrix} \frac{\partial f_1}{\partial x_1} & \cdots & \frac{\partial f_1}{\partial x_n} \\ & \ddots & \\ \frac{\partial f_n}{\partial x_1} & \cdots & \frac{\partial f_n}{\partial x_n} \end{pmatrix}$$

has determinant ± 1.

An **orbit** of (1.2) is a sequence $\{x_t\}_{t=0}^{\infty}$ such that

$$x_{t+1} = f_\varepsilon(x_t).$$

The orbits of the lift are often classified by their **rotation number** $\omega \in \mathbb{R}^d$,

$$\omega(x_0, z_0) = \lim_{t\to\infty} \frac{1}{t}(x_t - x_0) \tag{1.3}$$

if this limit exists. This quantity can be thought of as the average increase in the angles per iteration.

The **frequency map**

$$\Omega : \mathbb{R}^k \to \mathbb{R}^d$$

plays an important role in the dynamics of (1.2). In particular, every orbit of f_0 will obey

$$(x_t, z_t) = (x_0 + t\omega, z_0). \tag{1.4}$$

where $\omega = \Omega(z_0)$. From (1.4) we can conclude that every orbit lies on a d-dimensional torus, $\mathcal{T}_z = \mathbb{T}^d \times \{z\}$ that is invariant under the action of the map, $f_0(\mathcal{T}_z) = \mathcal{T}_z$. We call any torus that is homotopic to $\mathcal{T}_z$ **rotational**.

When ω is **incommensurate**,

$$\{(p, q) \in \mathbb{Z}^d \times \mathbb{Z} : p \cdot \omega = q\} = \{(0, 0)\}, \tag{1.5}$$

the orbits of f_0 are dense on $\mathcal{T}_z$. The orbits of f_0 with rational rotation vectors, $\omega \in \mathbb{Q}^d$, are periodic. More generally, each periodic orbit of (1.2) can be assigned a rotation vector by lifting the map to $\mathbb{R}^d \times \mathbb{R}^k$. The lift of a period-$n$ orbit obeys

$$(x_n, z_n) = (x_0 + m, z_0), \tag{1.6}$$

for $m \in \mathbb{Z}^d$, and thus has rotation vector $\omega = m/n$. We call these (m, n)-periodic orbits, see §2.2.1. A periodic orbit of a volume-preserving map is said to be spectrally **stable** if every eigenvalue of the Jacobian $Df^n(x, z)$ has unit modulus. A sequence of periodic orbits $\{(m_i, n_i)\}_{i=1}^{\infty}$ **approximates** the torus with rotation vector ω if $\lim_{i\to\infty} \frac{m_i}{n_i} \to \omega$.

The map f_0 is **integrable**, namely all of its orbits lie on tori on which the action is preserved and the dynamics on each torus is conjugate to a rigid rotation with some rotation vector ω [3]. KAM theory studies the persistence of the rotational tori of perturbations of integrable systems like f_0 [16, 100, 34]. The application of this theory requires that f_ε preserve some structure, is smooth enough, has a nondegenerate frequency map, and finally that the rotation vector of the torus be sufficiently irrational, e.g., be Diophantine, $\omega \in \mathcal{D}_s$, where

$$\mathcal{D}_s = \left\{ \omega \in \mathbb{R}^d : \exists\, c > 0 \ \text{ s.t. } |p \cdot \omega - q| > \frac{c}{|p|^s} \right\}, \tag{1.7}$$

for some $s \geq d$. The dynamics on the tori that persist will remain conjugate to rigid rotation,

$$\begin{aligned} x_t &= k_x(\theta + t\omega) \\ z_t &= k_z(\theta + t\omega). \end{aligned} \tag{1.8}$$

where $k : \mathbb{T}^d \to M$ such that $k_x(\theta + m) = k_x(\theta) + m$ and $k_z(\theta + p) = k_z(\theta)$ for any $m \in \mathbb{Z}^d$, $p \in \mathbb{Z}^k$. In other words, k_x is a degree-one circle map while k_z has degree zero. Since f_ε is real analytic the conjugacy k will be as well.

1.1 Two-Dimensional Maps

A frequently studied example of (1.2) with $d = k = 1$ is the generalized standard map

$$\begin{aligned} x' &= x + \Omega(z + \varepsilon g(x)) \mod 1, \\ z' &= z + \varepsilon g(x). \end{aligned} \tag{1.9}$$

When the **force** g and frequency map $\Omega : \mathbb{R} \to \mathbb{R}$ are differentiable (1.9) is a diffeomorphism with inverse

$$f^{-1}(x, z) = (x - \Omega(z), z - g(x - \Omega(z))). \tag{1.10}$$

We will further assume that $g(x)$ is a periodic function with period one and has zero average, so that (1.9) has zero net flux, a necessary condition for the existence of rotational circles when ε is nonzero [87]. The Jacobian of (1.9),

$$Df = \begin{pmatrix} 1 + \varepsilon Dg(x) D\Omega(z + \varepsilon g(x)) & D\Omega(z + \varepsilon g(x)) \\ \varepsilon Dg(x) & 1 \end{pmatrix}$$

has determinant $1 + \varepsilon Dg(x) D\Omega(z + \varepsilon g(x)) - \varepsilon Dg(x) D\Omega(z + \varepsilon g(x)) = 1$, implying (1.9) is area-preserving. Note that Ω is a function of $z + \varepsilon g(x)$ in (1.9) and that if we replaced this term with z the determinant would no longer equal one, and (1.9) would not be area-preserving.

The generalized standard map (1.9) can be applied to many physical models, including a charged particle in electrostatic waves, the adsorption of a layer of atoms on a crystal surface, and the motion of a particle in a relativistic cyclotron [87]. For example, when

$$\Omega = \Omega_1(z) = z \tag{1.11}$$

the resulting map is closely related to the Frenkel-Kontorova model [6], which describes a one-dimensional chain of point masses connected by springs and placed in a spatially periodic potential $\varepsilon V(x)$. If the spring constant is one then the spring potential energy has the form $\frac{1}{2}(x' - x)^2$ for each pair of neighboring particles at positions $x, x' \in \mathbb{R}$. The total local potential energy between the two neighbors is then

$$E(x, x') = \tfrac{1}{2}(x' - x)^2 + \varepsilon V(x) \tag{1.12}$$

and the formal total energy of the sequence $\{x_t : t \in \mathbb{Z}\}$ is the sum $H(\{x_t\}) = \sum_t E(x_t, x_{t+1})$. If the system is in equilibrium then

$$\frac{\partial H}{\partial x_i} = (-x_{i+1} - x_{i-1} + 2x_i) + \varepsilon DV(x_i) = 0. \tag{1.13}$$

Aubry [6] demonstrated that by defining $z_{i+1} = x_{i+1} - x_i$ the solution to (1.13) is equivalent to an orbit of (1.9) with (1.11) and $g(x) = DV(x)$.

The frequency map $\Omega : \mathbb{R} \to \mathbb{R}$ plays a key role in (1.9). When the twist condition

$$\frac{\partial \Omega}{\partial z} \neq 0 \tag{1.14}$$

is satisfied (1.9) is a nondegenerate twist map [87, 6], and the rotation number is a monotone function of z. Chirikov's map,

$$\begin{aligned} x' &= x + z' \\ z' &= z + \frac{\varepsilon}{2\pi} \sin(2\pi x) \end{aligned} \tag{1.15}$$

is an oft-studied example. Chirikov initially derived this system as a normal form for the behavior near a resonance in a symplectic or Hamiltonian system [30], however there are many other physical applications. For example, this map describes the dynamics of a kicked rotor with angular position x, angular momentum z, and kicking strength $\frac{\varepsilon}{2\pi}$.

When $\varepsilon = 0$ every orbit of the generalized standard map (1.9) lies on a circle on which the dynamics is conjugate to rigid rotation, recall (1.4), implying that the system is integrable. Whenever (1.9) is a real analytic nondegenerate twist map KAM theory guarantees the persistence of rotational circles with $\omega \in \mathcal{D}_1$ for $|\varepsilon| < \varepsilon_0$, for some $\varepsilon_0 > 0$. The dynamics on these circles will remain conjugate to rigid rotation (1.8) with k analytic.

When the frequency map satisfies the twist condition (1.14), the powerful theory of Aubry and Mather implies the existence of "minimizing" invariant sets for each rotation number ω [85, 6]. The notion of "minimizing" arises from the Frenkel-Kontorova interpretation. The minimizing sets are the solutions to (1.13) with globally minimal total energy with respect to all other variations with compact support [6]. By a theorem of Birkhoff, these invariant sets always lie on a Lipschitz

graph over x, and when ω is irrational they are either rotational invariant circles or invariant Cantor sets, what Percival called **cantori** [97].

Thus a Diophantine invariant circle for a twist map persists up to a critical parameter value, ε_{cr}, where it loses smoothness, and then for larger ε becomes a cantorus. Of course, it may reform for larger values of ε, and indeed the boundary of existence of an invariant circle for multi-parameter maps is often quite complex [18, 116, 61]. The formation of the family of gaps resulting in the creation of a cantorus is most easily understood by consideration of the ideas of the anti-integrable (AI) limit [7]. As ε increases, the potential energy in (1.12) will begin to dominate the spring energy and particles in the minimizing state will tend to fall into potential wells. For large enough ε, there are no particles in a neighborhood of the maxima of V, opening gaps in the circle. The orbits of each of these gaps form a bi-infinite family of gaps in the cantorus that Baesens and MacKay called a **hole** [9]. More formally, the AI theory studies the continuation of the critical points of $\lim_{\varepsilon\to\infty} \frac{1}{\varepsilon}H$, to finite ε. In the limit, the particles simply sit on any sequence of critical points of V. If these critical points are nondegenerate and the "acceleration" of the sequence is bounded, then such states may be continued to finite, large enough ε. Ordered, AI states with irrational ω continue to cantori [80]. Although initially developed for twist maps, AI theory has been extended to various other volume-preserving and dissipative systems.

However, neither Aubry-Mather theory nor the Frenkel-Kontorova energy (1.12) apply when the frequency map does not satisfy the twist condition. Thus, it is not known, though often assumed, whether invariant circles of nontwist maps are destroyed by the formation of a family of gaps, nor whether there are remnant Cantor sets that remain.

One well-studied example is the so-called standard nontwist map of Howard and Hohs [57], where

$$\Omega = \Omega_2(z) = z^2 - \delta. \tag{1.16}$$

When the twist vanishes, KAM theory still applies, providing—as for (1.16)—the curvature of Ω does not simultaneously vanish [38]. The nontwist map has rotational invariant circles that are

meandering, in the sense that they are not graphs over x, and the breakup of these circles has been extensively studied [2, 1, 51, 118].

1.2 Three-Dimensional Maps

Three-dimensional volume-preserving maps are generally less well understood than their two dimensional counterparts, although significant theory has been developed. We will consider a family of maps f_ε on $M = \mathbb{T}^2 \times \mathbb{R}$ of the form

$$\begin{aligned} x' &= x + \Omega(z - \varepsilon g(x), \delta) \mod 1, \\ z' &= z - \varepsilon g(x). \end{aligned} \tag{1.17}$$

that have an integrable limit when $\varepsilon = 0$. In this case $x \in \mathbb{T}^2$ represents two angles with unit period, $z \in \mathbb{R}$ represents an action-like variable, and δ is some parameter in the frequency map Ω, see §2.2. When g and Ω are differentiable then (1.17) is a diffeomorphism with inverse

$$f_\varepsilon^{-1}(x, z) = (x - \Omega(z, \delta), z + \varepsilon g(x - \Omega(z, \delta))). \tag{1.18}$$

Once again, we require that $g(x)$ be a periodic function of the angles x with period one and have zero average, otherwise f_ε will have no rotational tori [87]. Maps of this nature can be used to model the motion of a passive scalar in an incompressible fluid [99, 22], as well as granular mixing [86], and magnetic field-line flows [109].

At the integrable limit $\varepsilon = 0$, every orbit of (1.17) lies on a two-dimensional torus on which the dynamics is conjugate to rigid rotation (1.4) with $\omega = \Omega(z_0) \in \mathbb{R}^2$. KAM theory has been extended to guarantee the existence of some δ such that the tori with rotation vectors $\omega \in \mathcal{D}_2$ persist for $|\varepsilon| < \varepsilon_0$, for some $\varepsilon_0 > 0$, provided that the forcing is sufficiently smooth and the frequency map satisfies a nondegeneracy condition [28, 119]. However, so far neither Aubry-Mather theory nor the concepts of the AI limit have been applied successfully to general volume-preserving maps.

An often studied example of (1.2) is the ABC map,

$$\begin{aligned} x' &= x + \frac{A}{2\pi}\sin(2\pi z) + \frac{C}{2\pi}\cos(2\pi y) \\ y' &= y + \frac{B}{2\pi}\sin(2\pi x') + \frac{A}{2\pi}\cos(2\pi z) \\ z' &= z + \frac{C}{2\pi}\sin(2\pi y') + \frac{B}{2\pi}\cos(2\pi x'), \end{aligned} \tag{1.19}$$

a diffeomorphism on $M = \mathbb{T}^3$ with $A, B, C \in \mathbb{R}$ [45, 92]. This map is a natural discretization of the Arnold-Beltrami-Childress flow, a solution of the Euler equation as well as the Navier-Stokes equation with appropriate forcing [45]. To maintain consistent notation we will consider the integrable limit at $B = C = 0$ and lift the map to $M = \mathbb{T}^2 \times \mathbb{R}$, for which x and y are angles and z becomes an action-like variable.

The more recently developed standard volume-preserving map, to be introduced in §2.2, models the typical dynamics near a rank-one resonance [43]. Recall that Chirikov's map can be thought of as a normal form for the behavior near a resonance in a symplectic or Hamiltonian system [30]. In a similar way the standard volume-preserving map models near-resonant behavior in volume-preserving systems. Both maps are obtained from the general case by expansion around resonance and averaging over fast, nonresonant angles [43].

1.3 Reversibility

In many dynamical systems one cannot determine, from simple observation, if an object is moving forward or backward in time. Consider, for example, the motion of a pendulum. If the pendulum experiences friction the amplitude of the swing will decline over time. This change in amplitude provides a frame of reference-it allows us to determine if we are watching a movie of the pendulum forward or backward in time. However, if the pendulum is frictionless, no such reference frame exists, and it is impossible to discern the direction of time.

Systems that exhibit this type of symmetry are called **reversible**. For example, autonomous Hamiltonian systems with $H(p, q) = H(-p, q)$ are reversible as the equations of motion (1.1) are invariant under the transformation $(p, q, t) \to (-p, q, -t)$ [68]. These systems are ubiquitous in

nature. For example, Birkhoff exploited reversibility when investigating the restricted three-body problem [11].

More precisely, a map is reversible if there exists a homeomorphism S, called the reversor, such that

$$f \circ S = S \circ f^{-1} \tag{1.20}$$

[68, 69, 101]. The existence of reversors in the generalized standard map (1.9) depends on Ω and g, as described in App. E. The standard volume-preserving map is also reversible in some cases, as detailed in §2.2.2. The ABC map is only reversible when two of the parameters are equal [45].

An orbit Γ is **symmetric** with respect to the reversor S if $S(\Gamma) = \Gamma$. It is fortuitous that every symmetric periodic orbit of (1.9) and (1.17) must have points on two distinct fixed sets of the reversors, $\text{Fix}(S) = \{\xi : S(\xi) = \xi\}$, separated by half the period.

Lemma 1. *If $f : \mathbb{T}^d \times \mathbb{R}$ is a $d+1$ dimensional map with reversor S and Γ is a symmetric, (m,n)-periodic orbit of the lift F to the universal cover $\mathbb{R}^{d+1}$, then Γ has points on two fixed sets of the reversors.*

This standard lemma, which is reproven in App. A, implies that symmetric orbits can be found by looking for orbits that start on the fix set of one reversor, and "half" a period later end on the fix set of a different reversor, see Fig. 1.1. These periodic orbits can be located with a $d/2$-dimensional root-finding algorithm, resulting in greater speed and accuracy, see §2.3.

1.4 Breakup of Tori

In this dissertation we are concerned with the destruction of invariant rotational tori under perturbation in two- and three-dimensional volume-preserving maps. KAM theory guarantees the persistence of some of these tori for small ε, however does not say anything about what happens when $\varepsilon = \mathcal{O}(1)$. Rotational tori play a fundamental role in the dynamics of (1.2) whenever $d = 1$. In this case the tori have codimension-one and act as a boundary to transport, blocking orbits from moving from one region of phase space to another, shown for Chirikov's Map in Fig. 1.2. This

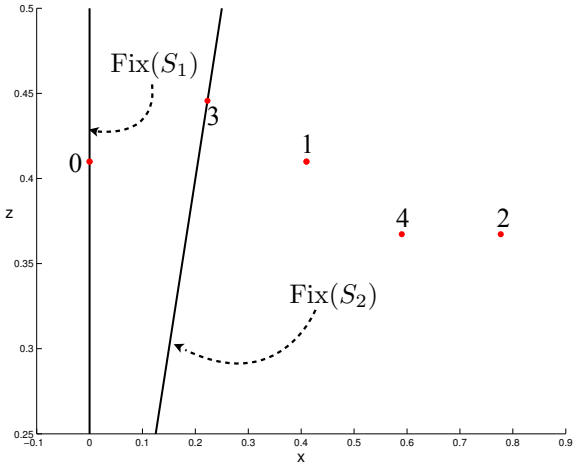

Figure 1.1: A symmetric (2,5) periodic orbit of (1.15) at $\varepsilon = 0.5$ emanating from Fix(S_1) (E.1) and landing on Fix(S_2) (E.2) $\frac{n+1}{2} = 3$ iterates later. The values alongside the points indicate the time along the orbit.

property follows from the continuity of the map and the invariance of the torus, see [45, App. B]. Knowledge of the existence or nonexistence of tori is therefore paramount when studying mixing and transport in volume-preserving maps.

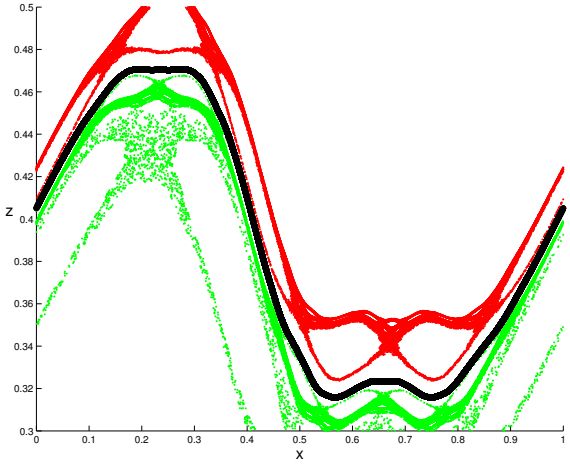

Figure 1.2: Orbits of Chirikov's standard map (1.15) for $\varepsilon = 0.971$. The chaotic orbits, shown in red and green, cannot mix due to the presence of the circle, plotted in black.

John Greene [54] exploited the periodic orbits in area-preserving maps to develop the first quantitative method to study the persistence of rotational circles. Greene conjectured that periodic orbits in the neighborhood of an invariant circle should be stable. Indeed, a sequence of periodic

orbits should limit upon a circle only if they remained stable in the limit. Conversely, if the limit of a family of periodic orbits is unstable, then the invariant circle should no longer exist. This method is known as **Greene's residue criterion** [54], see §2.1.

In Chapter 2 we extend Greene's residue criterion to reversible, three-dimensional volume-preserving maps with one action and two angles. This method exploits the additional structure of the symmetric periodic orbits to obtain a natural generalization of Greene's residue. We will demonstrate that this residue undergoes a dramatic shift from very small to exponentially large as ε grows, allowing us to predict the destruction of a torus with reasonable accuracy. However, the generalized residue that we use is only defined for symmetric periodic orbits, hence this method can only be applied to reversible maps.

Reversibility also plays an important role in the study of circles in the generalized standard map, (1.9). The application of Greene's criterion requires accurate computation of periodic orbits and then the linearization of the map about these orbits to determine their stability. When the force g is odd the generalized standard map (1.9) has a reversor whose fixed sets intersect every rotational circle, see App. E. A consequence is that every rotational circle is symmetric and can be approximated by a sequence of symmetric periodic orbits, recall §1.3. Since these orbits can be computed with greater speed and accuracy than asymmetric periodic orbits, all previous studies have examined the standard map with odd forcing, see, for example [54, 62, 55]. The mechanism for breakup of invariant circles in nonreversible maps remains an open question, first posed by MacKay in his thesis [78]

The reversibility requirement can be circumvented by studying the tori directly, rather than the periodic orbits that approximate them. In Chapter 3 we describe a Fourier-based quasi-Newton scheme to compute the embedding for an invariant torus with given frequency in volume-preserving maps, adapted from the algorithm for area-preserving maps derived in [59]. We will then demonstrate how the smoothness of these embeddings can be used to predict the destruction of a torus, as shown by [20, 21] for area-preserving maps. We exploit this method to study the tori of both reversible and nonreversible three-dimensional volume-preserving maps in Chapter 6.

In Chapter 4 we explore the breakup of the tori by analyzing the deformation of the conjugacy. We begin with the relatively simple case of area-preserving twist maps, for which both Aubry-Mather and Anti-Integrability theory hold. We will demonstrate that cantori predicted by these theories are observable in the conjugacy of the tori for these maps. We will then explore the conjugacies of tori in both nontwist standard maps and volume-preserving maps, for which Aubry-Mather theory does not apply.

Chapter 5 investigates the locally and globally most robust circles in area-preserving maps. We begin by establishing a relationship between the discriminant of the rotation number and the local robustness of the corresponding circle. We then analyze the critical function of the locally most robust circles to establish which is globally most robust for a variety of generalized standard maps.

The conclusion, in the seventh chapter, will summarize the original accomplishments of this dissertation and outline areas of future research.

Chapter 2

Greene's Residue Criterion for the Breakup of Invariant Tori of Volume-Preserving Maps

In this chapter we generalize Greene's residue criterion to reversible volume-preserving maps. We will study a two-angle, one-action map, see §2.2, that models the typical dynamics near a rank-one resonance [43]. As we discuss in §2.2.2, our model—like Chirikov's map (1.15)—is reversible, and this makes finding periodic orbits especially easy: a two-dimensional secant method suffices, see §2.3. Another important consequence of reversibility is that one of the three multipliers of a symmetric orbit is always 1; we use this to obtain a natural generalization of Greene's residue for reversible maps, see §2.2.4.

One complicating feature of (1.2) is that the image of the frequency map $\Omega(z)$ is at most a one-dimensional subset of the two-dimensional space of rotation vectors; a consequence is that orbits with given rotation vectors typically do not exist for fixed parameters. In our three-dimensional model, we get around this by adding a new parameter, δ, to Ω so that $\Omega : (z, \delta) \mapsto (\omega_1, \omega_2)$ is a diffeomorphism. With this modification, we observe, in §2.3, that for any ε and any $m/n \in \mathbb{Q}^2$ one can find (z, δ) for which there is a symmetric, (m, n)-orbit on each symmetry line.

We will show in §2.4 that the residues of high period orbits appear to undergo a rapid transition from "nearly zero" to "exponentially large" as ε grows, just like for the standard map (1.15). In §2.5 we use this transition to get a reasonably sharp estimate for a critical set of parameters at which a given torus is apparently destroyed.

The tori that we study in §2.5 have rotation vectors that are integral bases for the cubic

algebraic field $\mathbb{Q}(\sigma)$, where σ is the "spiral mean" [64], see §2.5.1. It has long been conjectured that simple cubic irrationals like the spiral mean could be the analogue of the golden mean for the standard map (1.15). Indeed, most of the previous studies of Greene's criteria for multidimensional tori have used vectors in $\mathbb{Q}(\sigma)$, though there have been several that studied other cubic irrationals [111, 120, 121] and even quartic irrationals [115, 66].

Another remarkable conjecture in [54] is that the last invariant circle of (1.15) has the golden mean rotation number. There is strong numerical support for this conjecture, and more generally for the conjecture that circles with "noble" rotation vectors appear to be locally most robust [84], see Chapter 5. Do these notions have a higher-dimensional generalization? We are not aware of any previous progress on this question. In §2.7 we look for the last torus for our model by finding the critical parameter values, $(\varepsilon_{cr}(\omega), \delta_{cr}(\omega))$, for a set of tori whose rotation numbers ω are integral bases of $\mathbb{Q}(\sigma)$. We use Kim and Ostlund's generalization of the Farey tree, reviewed in App. B, to systematically generate sets of Diophantine rotation vectors.

2.1 Greene's Residue Criterion

John Greene studied the persistence and destruction of rotational invariant circles of the standard map (1.15) [53, 54] by approximating them with sequences of periodic orbits. The Poincaré-Birkhoff theorem implies that the standard map has at least two (m, n)-periodic orbits for any choice of rational rotation number $\frac{m}{n}$ [87]. These orbits, which exist for all ε, are often called the **Birkhoff orbits**. Since the standard map is area-preserving, the product of the multipliers of any period-n orbit is 1, and so its stability can be completely characterized by a quantity Greene called the residue:

$$R \equiv \tfrac{1}{4}(2 - \tau), \quad \text{where } \tau \equiv \operatorname{tr}(Df^n(x, z)). \tag{2.1}$$

The residue conveniently encodes the stability of an orbit: it is elliptic (complex, unit modulus multipliers) when $0 < R < 1$, hyperbolic (real, positive multipliers) when $R < 0$, and reflection hyperbolic (real, negative multipliers) when $R > 1$. One of the two Birkhoff orbits of (1.15) has

positive residue while the other has negative residue, and Greene showed that for a period-n orbit of (1.15),

$$R = \mathcal{O}(\varepsilon^n), \tag{2.2}$$

both for $\varepsilon \ll 1$ and for $\varepsilon \gg 1$.

Greene's 6^{th} assertion, now known as **Greene's Residue Criterion**, is perhaps the most astonishing of the conjectures in [54]. In particular, consider an irrational rotation number $\omega \in \mathbb{R}\backslash\mathbb{Q}$, with continued fraction $\omega = [k_0, k_1, \ldots] = k_0 + 1/(k_1 + 1/(\ldots))$, and let

$$\frac{m_\ell}{n_\ell} = [k_0, k_1, \ldots, k_\ell] \tag{2.3}$$

be its ℓ^{th} convergent. Thus the (m_ℓ, n_ℓ)-Birkhoff orbits, with residues $R_\ell^\pm$, have rotation numbers that converge to ω. One formulation of Greene's criterion is:

> **Greene's Residue Criterion**: A rotational invariant circle of an area-preserving twist map with a given irrational rotation number ω exists if and only if the residues of its convergent Birkhoff orbits, $R_\ell^\pm$, remain bounded as $\frac{m_\ell}{n_\ell} \to \omega$.

A stronger version of this criterion asserts that when there is an invariant circle, the mean residue,

$$\mu(\omega) = \lim_{\ell\to\infty} \frac{1}{n_\ell} \log |R_\ell|, \tag{2.4}$$

exists and is negative for any sequence of (m_ℓ, n_ℓ)-orbits whose rotation number converges to ω.

Greene studied in particular the invariant circle with golden mean rotation number

$$\phi = \tfrac{1}{2}(1 + \sqrt{5}) = [1, 1, 1, \ldots]. \tag{2.5}$$

For the convergents to ϕ, numerical studies show that there is a parameter value $\varepsilon_{cr}(\phi)$ such that $R_\ell^\pm \to 0$ as $\ell \to \infty$ whenever $\varepsilon < \varepsilon_{cr}(\phi)$. Conversely, whenever $\varepsilon > \varepsilon_{cr}(\phi)$ the residues grow exponentially with the period, and there appears to be no golden invariant circle. Greene estimated ε_{cr} by computing a sequence of parameter values for which $|R_l^\pm|$ reaches some fixed value $R_{th} > 0$, obtaining

$$\varepsilon_{cr}(\phi) \approx \frac{1}{2\pi} 0.97163540631. \tag{2.6}$$

The value of the threshold R_{th} is irrelevant, but Greene found that $R_{th} \approx 0.25$ gave the most rapid convergence. Details for the implementation of this method can be found in App. D

Some aspects of Greene's residue conjecture have been proven.

Theorem 2 (Residue Criterion for Twist Maps [77, 44])**.** *Suppose f_ε is an analytic, area-preserving twist map, and the sequence of (m_ℓ, n_ℓ)-orbits converges to an analytic invariant circle on which the dynamics is analytically conjugate to rigid rotation with rotation number $\omega \in \mathcal{D}_s$, then there are constants $C, K > 0$ such that*

$$|R_l| < C \exp\left(-K|\omega - m_\ell/n_\ell|^{-1/(1+s)}\right)$$

In particular since $|\omega - m_\ell/n_\ell| < c/n_\ell^2$ for continued fraction convergents, this implies that $R_l \to 0$ exponentially in the period. The residue criterion also applies to twist-reversing maps [38], as studied numerically by [37, 2].

Aspects of the converse statement of the residue criterion have also been proven for area-preserving twist maps. From Aubry-Mather theory, these maps have a set of "minimizing" orbits for each ω, and when ω is irrational this set is either a circle or a Cantor set—a cantorus. If the cantorus has a positive Lyapunov exponent, then there exists a sequence (m_ℓ, n_ℓ) such that the mean residue (2.4) is positive and has the value of this exponent [44]. Moreover, if the cantorus is uniformly hyperbolic, then this sequence can be taken to be the sequence of minimizing orbits (the negative residue Birkhoff orbits) [77].

The residue criterion has also been generalized to higher dimensions. Tompaidis generalized Greene's criterion to higher-dimensional symplectic and quasiperiodically-forced symplectic maps [110]. Indeed, the residue criterion has been applied to study the breakup of two-tori for several four-dimensional models, e.g., the Froeshlé map [14, 15, 111, 66, 112, 120, 121, 24], and a quadratic map [115]. For example, a $2d$ dimensional symplectic map has **partial residues**

$$R^{(j)} = \tfrac{1}{4}(2 - \lambda_j - \lambda_j^{-1}) \,, \quad j = 1, \ldots, d$$

for each of the reciprocal pairs of multipliers of a given orbit [65].

Tompaidis [110] proved that if f_ε is a C^r symplectic map with $r > 1$, and the twist, $D\Omega$, is nondegenerate then, when there is a C^r, Diophantine, invariant d-torus, the partial residues of any (m, n)-periodic orbits with rotation numbers sufficiently close to ω obey the bound

$$|R^{(j)}| < Cn|n\omega - m|^k$$

for any positive integer $k < (r-1)/2s$. His results also apply to the rotating standard map of [5].

We are not aware of previous use of the residue criterion for volume-preserving maps apart from a quasiperiodically-forced, area-preserving map [4, 5, 111], a three-dimensional map with one of the components of Ω set to a fixed irrational value. Thus we turn to numerical investigations of a model.

2.2 One-Action Maps: A Three-Dimensional Model

In the remainder of this chapter, we will study the rotational tori of a three-dimensional map of the form (1.2) introduced by [43]. Just as Chirikov's standard map (1.15) describes the generic dynamics of a Hamiltonian system near a "rank-one" resonance, the normal form derived in [43] represents the local dynamics near a rank-one resonance of a $(d+1)$-dimensional volume-preserving map. The resulting local dynamics of (1.2) is strongly influenced by whether the curve $\Omega(z)$ is transverse to or tangent to such a resonance. The normal form of [43], with the frequency map

$$\Omega(z, \delta) = (z + \gamma, \beta z^2 - \delta), \tag{2.7}$$

applies to both cases. Indeed, the first component of this frequency map has the "twist" property of (1.15), representing transverse crossing, while the second has the twist-reversal property of the standard nontwist map (1.16) [37], representing tangency. This combination arises from expansion and averaging transformations in the neighborhood of resonance for a $(d+1)$-dimensional volume-preserving map [43]. Of course, rotational tori near a resonance are typically fragile. Nevertheless, when $\beta \neq 0$, (2.7) satisfies the nondegeneracy condition

$$\det(D_z\Omega, D_z^2\Omega, \ldots, D_z^d\Omega) \neq 0 \tag{2.8}$$

that is sufficient for KAM theory [28, 119].

For fixed (γ, β, δ), the image $\Omega : z \mapsto \omega$ is a parabola. However, when thought of as a map $\Omega : (z, \delta) \mapsto (\omega_1, \omega_2)$, Ω becomes bijective. The parameter δ is also important in another sense: it unfolds a tangency with the $(0, 1, 0)$ resonance (at $z = \delta = 0$). As was shown in [43], near a resonant tangency, even though the "twist" condition (2.8) applies, the dynamics is like that of nontwist maps. Consequently, we will take δ to be an essential parameter, but will fix β and γ. Indeed, in some sense, δ could be also be regarded as a dynamical variable, by adjoining trivial dynamics to the map:

$$(x', z', \delta') = (f(x, z, \delta), \delta). \tag{2.9}$$

In this sense, one could think of the map as a diffeomorphism on $\mathbb{T}^2 \times \mathbb{R}^2$. In particular, to find periodic orbits and tori, we not only need to find an appropriate the initial condition (x, z), but also must determine the appropriate "initial condition" for δ, see §2.2.1. Of course since δ is constant for the dynamics (2.9), we will simply regard this value as a necessary parameter in the specification of an orbit.

A requirement for the preservation of the rotational tori of (1.2) for nonzero ε is that the map satisfy an "intersection property". A necessary condition is that the force has zero average,

$$\int_{\mathbb{T}^d} g(x, z, \varepsilon) dx = 0. \tag{2.10}$$

Indeed, if (2.10) is not satisfied, then f_ε may have no invariant tori; for example, when $g(x, z, \varepsilon) = const \neq 0$, then the z coordinates of (1.2) drift and there are no recurrent orbits for any $\varepsilon \neq 0$. We will use the simple form

$$g(x) = a \sin(2\pi x_1) + b \sin(2\pi x_2) + c \sin(2\pi(x_1 - x_2)), \tag{2.11}$$

for the force, which satisfies (2.10). The three terms in g represent resonant forcing for $(p, q) = (1, 0, q)$, $(0, 1, q)$ and $(1, -1, q)$, respectively, for each $q \in \mathbb{Z}$. The last term explicitly couples the two angles (x_1, x_2); however, note that even when $c = 0$ these are coupled through the frequency map (2.7).

As a final simplification, we will choose the perturbation h in (1.2) so that $\varepsilon h \equiv \Omega(z) - \Omega(z')$, giving the model of [43]

$$f_\varepsilon : \begin{cases} x' = x + \Omega(z', \delta) \mod 1, \\ z' = z - \varepsilon g(x). \end{cases} \tag{2.12}$$

An advantage of this form is that it is always a homeomorphism; indeed, it has the inverse (1.18). In addition, this map is an exact-volume-preserving diffeomorphism whenever Ω and g are C^1 and g satisfies (2.10).

Following [90], we will typically use the "standard" set of parameters

$$a = b = c = 1,\ \beta = 2,\ \gamma = \tfrac{1}{2}(\sqrt{5} - 1), \tag{2.13}$$

and think of ε and δ as the parameters that govern the strength of the forcing and the unfolding of the tangency, respectively. Unless otherwise mentioned, all the computations below are for (2.12) with the frequency map (2.7), the force (2.11), and the standard parameters (2.13).

2.2.1 Periodic Orbits

Rotational periodic orbits of (2.12) are partially classified by their rotation vectors. Let F_ε be the lift of f_ε to the universal cover $\mathbb{R}^3$ of M obtained by simply removing the mod 1 from (2.12). A sequence

$$\Gamma = \{(x_t, z_t) = F_\varepsilon(x_{t-1}, z_{t-1}) : t \in \mathbb{Z}\} \tag{2.14}$$

is a type $(m, n) \in \mathbb{Z}^2 \times \mathbb{N}$ periodic orbit of F_ε if it obeys (1.6). Alternatively, noting that the rigid translation operator

$$T_m(x, z) = (x + m, z), \tag{2.15}$$

is a symmetry of F_ε, then the periodicity condition becomes $T_{-m}F_\varepsilon^n(x, z) = (x, z)$. If m and n are coprime, i.e., $gcd(m_1, m_2, n) = 1$, the projection of each such orbit onto M is a period-n orbit of f_ε.

An (m,n)-orbit of (2.12) with the frequency map (2.7) must satisfy the three equations

$$\begin{aligned} m = \sum_{t=0}^{n-1} \Omega(z_t,\delta) \Rightarrow \begin{cases} m_1 = n\gamma + \sum_{t=0}^{n-1} z_t \\ m_2 = -n\delta + \beta \sum_{t=0}^{n-1} z_t^2 \end{cases}, \\ 0 = \sum_{t=0}^{n-1} g(x_t). \end{aligned} \tag{2.16}$$

with $(x_t, z_t) = F_\varepsilon^t(x_0, z_0)$. Ideally a system of three equations in three unknowns has isolated solutions; however, we recall again that for any fixed δ and a given (m,n), there are typically no solutions of (2.16). For example, when $\varepsilon = 0$, the curve $\Omega(z,\delta)$ will typically not intersect the point $\frac{m}{n}$, and there will be no (m,n)-orbit. However, including the parameter δ in (2.7), there is an orbit when $\varepsilon = 0$ at

$$(z^*, \delta^*) = \left(\frac{m_1}{n} - \gamma, \beta z^{*2} - \frac{m_2}{n} \right), \tag{2.17}$$

and any value for x. This corresponds to a two-torus of (m_1, m_2, n)-orbits of f_0.

More generally, if an orbit satisfies the first and last equations in (2.16), then the value of δ is completely determined by the second of these equations, which can be rewritten as

$$\delta = \frac{\beta}{n} \sum_{t=0}^{n-1} z_t^2 - \omega_2 \equiv \left\langle z^2 \right\rangle - \omega_2. \tag{2.18}$$

Thus δ is fixed by the mean-square time average of the action along the orbit. Of course the system (2.16) cannot be solved independently of δ, since the iterates of (2.12) depend on its value. As we will see below, with δ included as a varying parameter, it appears that f_ε has orbits for all $(m,n) \in \mathbb{Z}^2 \times \mathbb{N}$.

For example, fixed points of (2.12) occur with (z^*, δ^*) given by (2.17) upon setting $n = 1$. Thus these values are uniquely determined for any (m_1, m_2). The angles are then determined by $g(x^*) = 0$, which generically has a one-dimensional set of solutions that projects to circles on $\mathbb{T}^2$. For example, if $a = b = c$ fixed points occur on the three circles $x_1 = 0$, $x_2 = \frac{1}{2}$, and $x_1 - x_2 = \frac{1}{2}$. More generally there is at least a pair of circles of fixed points; an example is shown in Fig. 2.1.

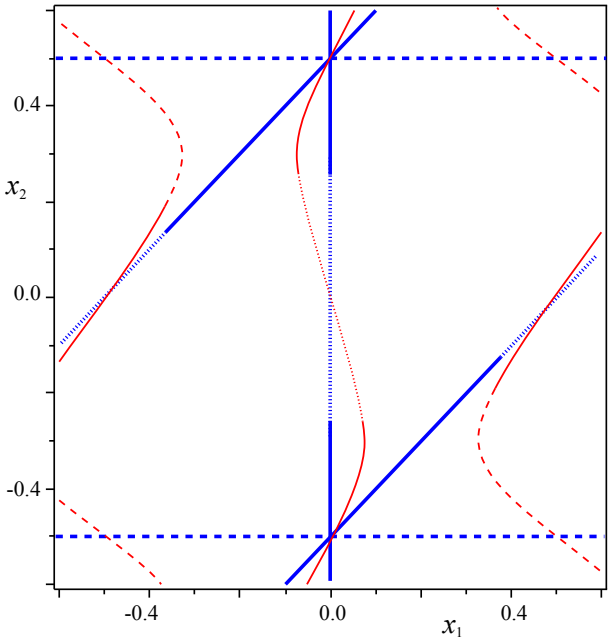

Figure 2.1: Curves of fixed points for (2.12) projected onto the angles x. The thick (blue) lines correspond to the case $a = b = c$, and the thinner (red) curves to $(a, b, c) = (1.0, 0.7, 0.3)$. The stability of these orbits is indicated for $\varepsilon = 0.7$ and $m_1 = 1$; unstable orbits with $R < 0$ are shown as dashed lines and those with $R > 1$ as dotted lines, where R is defined in (2.25).

For period two, the system (2.16) becomes

$$\begin{aligned} z_0 &= \tfrac{1}{2}(m_1 + \varepsilon g(x_0)) - \gamma, \\ z_1 &= \tfrac{1}{2}(m_1 - \varepsilon g(x_0)) - \gamma, \\ x_1 &= x_0 + \Omega(z_1, \delta), \\ \delta &= \tfrac{1}{2}(\beta z_0^2 + \beta z_1^2 - m_2) \end{aligned} \tag{2.19}$$

leaving one transcendental equation

$$g(x_0) + g(x_1) = 0$$

for x_0. Consequently, there is again a set of curves of period-two orbits. Note however, that the value of δ depends upon ε and m for $n = 2$. This holds more generally for higher period orbits as well.

2.2.2 Reversibility

As for the standard map (1.15), it is very convenient that the map (2.12) with (2.11) is reversible because this simplifies the search for periodic orbits. Recall that a map is reversible if it is conjugate to its inverse, that is if there exists a homeomorphism S such that $f \circ S = S \circ f^{-1}$. The collection of symmetries and reversors of a map form a group, the **reversing symmetry** group, see App. E, [103, 69].

Whenever g is an odd function (as in (2.11)), the map (2.12) is reversible, with the two reversors

$$\begin{aligned} S_1(x,z) &= (-x, z - \varepsilon g(x)), \\ S_2(x,z) &= (-x + \Omega(z,\delta), z). \end{aligned} \tag{2.20}$$

To see this note that

$$S_2(x,z) = f \circ S_1(x,z) = S_1 \circ f^{-1}(x,z),$$

since the inverse of f is (1.18). Since g is odd, both S_1 and S_2 are involutions, that is $S_i^2 = id$, consequently

$$f = S_2 \circ S_1.$$

Factorization into a pair of involutions also holds for Chirikov's standard map (1.15), and this was exploited by Greene and MacKay [78].

An orbit (2.14) is **symmetric** with respect to a reversor S if $S(\Gamma) = \Gamma$; i.e., there exists a $j \in \mathbb{Z}$ such that $S(x_0, z_0) = (x_j, z_j)$. Denoting the fixed sets of the reversors by $\mathrm{Fix}(S_i)$, it is well-known that any symmetric orbit necessarily has points on these sets, see App. A. Indeed, for the lift, there are two points on two fixed sets that occur essentially halfway around the orbit (depending on whether n is even or odd), and essentially halfway along in the angle direction (depending on whether the components of m are even or odd), see Table 2.1. For the reversors (2.20) and translation symmetry (2.15), the relevant fixed sets are the curves

$$\begin{aligned} \mathrm{Fix}(S_1 \circ T_{-m}) &= \{(\tfrac{m}{2}, z) : z \in \mathbb{R}\}, \\ \mathrm{Fix}(S_2 \circ T_{-m}) &= \{(\tfrac{1}{2}(\Omega(z,\delta) + m), z) : z \in \mathbb{R}\}. \end{aligned} \tag{2.21}$$

n	S_i	S_f	χ
even	S_1	$S_1 \circ T_{-m}$	$\frac{n}{2}$
	S_2	$S_2 \circ T_{-m}$	$\frac{n}{2}$
odd	S_1	$S_2 \circ T_{-m}$	$\frac{n+1}{2}$
	S_2	$S_1 \circ T_{-m}$	$\frac{n-1}{2}$

Table 2.1: Initial, S_i, and final, S_f, symmetries for (m,n)-symmetric periodic orbits for a lift F of a reversible map with reversors S_1 and $S_2 = F \circ S_1$ and discrete rotation symmetry T_m. The initial point $(x_0, z_0) \in \mathrm{Fix}(S_i)$ maps to the point $(x_\chi, z_\chi) \in \mathrm{Fix}(S_f)$ in χ iterations.

Projecting back to the torus $\mathbb{T}^2$, we see there are eight symmetry curves—four for S_1, the lines above $x = (0,0)$, $(\frac{1}{2},0)$, $(0,\frac{1}{2})$ and $(\frac{1}{2},\frac{1}{2})$, and four curves for S_2. Since symmetric orbits intersect these lines in pairs, as shown in Table 2.1, we expect to find four distinct symmetric periodic orbits for each (m,n).

Moreover, since the one-dimensional fixed sets are graphs over the action coordinate, z, **any** rotational invariant torus of f necessarily intersects **all** of these fixed sets. Consequently, there are symmetric orbits on each rotational torus, and if the dynamics on the torus is conjugate to an incommensurate rotation, then the symmetric orbits are dense. Therefore using symmetric periodic orbits as limiting approximations to rotational tori seems reasonable.

2.2.3 Stability

The linear stability of a period-n orbit, $(x^*, z^*) = f^n(x^*, z^*)$, is determined by its Jacobian matrix, $Df^n(x^*, z^*)$. When $f : M \to M$ is volume-preserving and M is three-dimensional, the characteristic polynomial takes the form

$$\det(\lambda I - Df^n(x^*, z^*)) = \lambda^3 - \tau_1\lambda^2 + \tau_2\lambda - 1,$$

where the trace τ_1 and second trace τ_2 are defined by

$$\begin{aligned} \tau_1 &= \mathrm{tr}(Df^n), \\ \tau_2 &= \tfrac{1}{2}(\tau_1^2 - \mathrm{tr}(Df^n)^2). \end{aligned} \tag{2.22}$$

There are eight generic multiplier configurations in the τ_1-τ_2 plane as shown in Fig. 2.2 [74]. The line $\tau_1 = \tau_2$ corresponds to the existence of a multiplier $\lambda = 1$. The only (τ_1,τ_2) values corresponding

to stable orbits lie on the segment $-1 < \tau_1 = \tau_2 < 3$ where there is a conjugate pair of multipliers on the unit circle. When $\tau_1 > 3$, this pair becomes hyperbolic, and, when $\tau_1 < -1$, reflection hyperbolic.

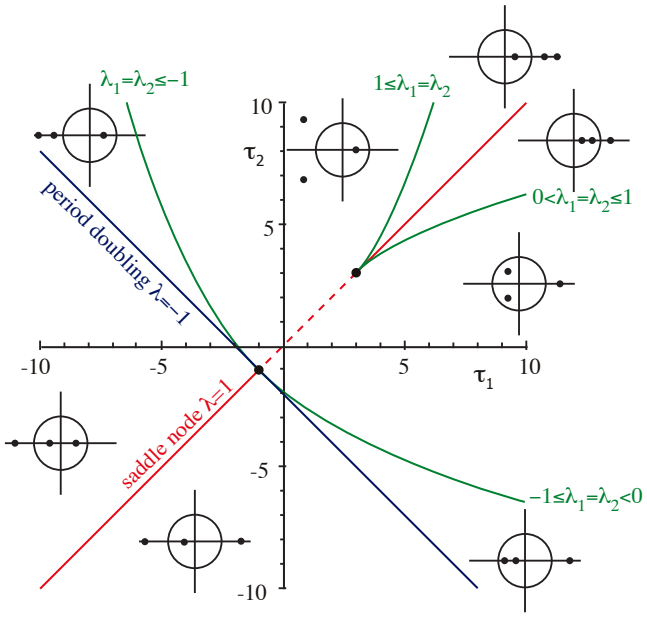

Figure 2.2: Stability diagram for a three-dimensional, volume-preserving map depending upon the trace τ_1 and second trace τ_2. The eight insets show multiplier configurations in the complex-λ plane relative to the unit circle for each of the eight stability domains.

The Jacobian Df of (2.12) is the matrix (in 2×1 block form)

$$Df = \begin{pmatrix} I - \varepsilon \nabla\Omega(z') Dg(x) & \nabla\Omega(z') \\ -\varepsilon Dg(x) & 1 \end{pmatrix}. \tag{2.23}$$

In this expression, Dg is the row vector $(\nabla g)^T$, while $\nabla\Omega(z)$ is a column vector, so that $\nabla\Omega Dg$ is the outer product of these vectors.

Interestingly, (2.23) has the property that, for $n = 1$,

$$\tau_1 = \tau_2 = 3 - \varepsilon \nabla\Omega(z') \cdot \nabla g, \tag{2.24}$$

for any functions Ω and g. Consequently one of the multipliers of Df is always 1, and thus every fixed point has multipliers $(1, \lambda, 1/\lambda)$. For example, in Fig. 2.1 the unstable fixed points are indicated by dashed ($\tau_1 < -1$) and dotted ($\tau_1 > 3$) curves. For the parameters (2.13), the fixed

points on the line $x_1 - x_2 = \frac{1}{2}$ are stable up to $\varepsilon = [\pi(2\beta z^* - 1)]^{-1}$ with z^* given by (2.17). At this parameter value, $\tau_1 = -1$ for the point $(\frac{1}{2}, 0, z^*)$, and as ε grows there is an interval of unstable fixed points orbits on this line. Similarly on the line $x_2 = 0$ the point $(0, 0, z^*)$ first loses stability with $\tau_1 = -1$ at $\varepsilon = \frac{1}{\pi}$. The fixed points on the line $x_2 = \frac{1}{2}$ have $\tau_1 > 3$ for all $\varepsilon > 0$.

2.2.4 The Residue

We noted above that $\tau_1 = \tau_2$ for fixed points of any map of the form (2.12). Of course the equality $\tau_1 = \tau_2$ need not be true for $Df^n(x, z)$, so periodic orbits with periods larger than 1 may not have a unit multiplier. However, for symmetric orbits, the property $\tau_1 = \tau_2$ follows from the conjugacy of Df to Df^{-1}.

Lemma 3. *If Γ is a symmetric periodic orbit of a reversible, three-dimensional, volume-preserving map, then it must have a multiplier $\lambda = 1$, or equivalently, $\tau_1 = \tau_2$.*

Proof. This follows from the more general result: each symmetric periodic orbit of a reversible diffeomorphism has reciprocal multipliers, i.e., if λ is multiplier, then so is λ^{-1}. Indeed by Lem. 5 in App. A, there is a point $x^* \in \Gamma$ and a reversor S such that $x^* \in \mathrm{Fix}(S)$. Moreover, since $S \circ f = f^{-1} \circ S$, then $f^n = S^{-1} \circ f^{-n} \circ S$, so that the matrix $A = Df^n(x^*)$ is conjugate to $Df^{-n}(x^*)$. Since $Df^{-n}(x^*) = A^{-1}$, A and A^{-1} have the same spectrum.

Finally, for the three-dimensional, volume-preserving case, the product of the three multipliers is one, and since the multipliers come in reciprocal pairs, there must be a multiplier $\lambda = 1$. This is equivalent to $\tau_1 = \tau_2$. □

A related observation is that chaotic orbits of a reversible map have a zero Lyapunov exponent if they visit symmetrically related regions with equal probabilities [45].

Using this result, we let $\tau = \tau_1 = \tau_2$ and define an analogue to Greene's residue (2.1) for symmetric orbits

$$R = \frac{1}{4}(3 - \tau) , \quad \tau = \mathrm{tr}(Df^n(x, z)). \tag{2.25}$$

This definition was also used to study periodic orbits for the rotating standard map [5, 111] where reversibility was not required, since one of the three multipliers is identically equal to one for all orbits.

Just as for Greene's residue, orbits are stable when $0 < R < 1$ where they have a complex conjugate multiplier pair on the unit circle; these are analogous to elliptic orbits. The complex pair hits minus one at $R = 1$ and is subsequently replaced by a reciprocal pair of negative multipliers when $R > 1$. When $R = 0$ the orbit has a triple multiplier $\lambda = 1$, and when $R < 0$ there is a reciprocal pair of positive eigenvalues; these orbits are analogous to hyperbolic orbits of an area-preserving map.

Analytical formulae for the positions and residues of the symmetric fixed points are shown in Table 2.2. The fixed points lie on $\mathrm{Fix}(S_1) \cap \mathrm{Fix}(S_2)$, recall (2.21), since $m = \Omega(z^*)$. Their residues depend upon the parity of the components of m, which we denote by "e" for even and "o" for odd. There are four parities as shown in the table.

Symmetric, period-two orbits must solve the system (2.19). Thus on $\mathrm{Fix}(S_1)$, the orbit is

$$(0, \frac{m_1}{2} - \gamma) \mapsto (\frac{m}{2}, \frac{m_1}{2} - \gamma),$$

for $\delta^* = \frac{1}{4}\beta(m_1 - 2\gamma)^2 - \frac{m_2}{2}$. Since $gcd(m_1, m_2, n) = 1$, there are three types of such orbits, depending upon the parity of m. Their residues depend similarly on this parity, see Table 2.2. A period-two orbit that begins on $\mathrm{Fix}(S_2)$ is given by

$$(\tfrac{1}{2}\Omega(z^*), z^*) \mapsto (m - \tfrac{1}{2}\Omega(z^*), m_1 - 2\gamma - z^*),$$

where the initial action must satisfy the transcendental equation

$$2z^* - g(\tfrac{1}{2}\Omega(z^*)) = m_1 - 2\gamma,$$

and δ^* is determined by (2.19). The residue of these orbits does not have a simple analytical form.

(m,n)	(x^*,z^*)	δ^*	R
$(e,e,1)$	$(0,0,m_1-\gamma)$	$\beta z^{*2}-m_2$	$\pi\varepsilon$
$(e,o,1)$	$(0,\frac{1}{2},m_1-\gamma)$		0
$(o,e,1)$	$(\frac{1}{2},0,m_1-\gamma)$		$\pi\varepsilon(2\beta z^*-1)$
$(o,o,1)$	$(\frac{1}{2},\frac{1}{2},m_1-\gamma)$		$-2\pi\beta\varepsilon z^*$
$(o,o,2)$	$(0,0,\frac{m_1}{2}-\gamma)$	$\beta z^{*2}-\frac{1}{2}m_2$	$2\pi\varepsilon(1-2\beta z(1-2\pi\varepsilon))$
$(o,e,2)$	$(0,0,\frac{m_1}{2}-\gamma)$		$2\pi\varepsilon(2\pi\varepsilon+2\beta z(1-2\pi\varepsilon))$
$(e,o,2)$	$(0,0,\frac{m_1}{2}-\gamma)$		$2\pi\varepsilon$

Table 2.2: Properties of the four types of fixed points and three types of period-two orbits beginning on $\mathrm{Fix}(S_1)$ for $a=b=c=1$. Orbits are classified by the parity of the components of m.

2.3 Computing Symmetric Orbits

The computation of symmetric periodic orbits can be reduced to finding the zeros of a function $H:\mathbb{R}^2\to\mathbb{R}^2$ since the orbits must begin and end on fixed sets of the reversors. Indeed, for a given fixed set, the initial angles are completely determined by (z,δ). We therefore need only determine $z_0=z^*$ and δ^* by requiring that $x_n=x_0+m$. In addition, the numerical work can be halved: since the "half-orbit" lands on another fixed set, recall Table 2.1, only $\chi\sim n/2$ iterations need to be performed.

More concretely, let $(x^i(z,\delta),z)\in\mathrm{Fix}(S_i)$ and $(x^f(z,\delta),z)\in\mathrm{Fix}(S_f)$ denote points on the initial and final symmetry curves of an (m,n)-orbit, given in Table 2.1 using (2.21). If, for example, $S_f=S_1\circ T_{-m}$ then $x^f(z,\delta)=\frac{1}{2}m$, and if $S_f=S_2\circ T_{-m}$ then $x^f(z,\delta)=\frac{1}{2}(\Omega(z,\delta)+m)$. Denoting the length of the half-orbit by χ so that $(x_\chi,z_\chi)=F^\chi(x^i(z,\delta),z)$, then an (m,n)-orbit corresponds to a zero of

$$H(z,\delta)=x_\chi(z,\delta)-x^f(z_\chi(z,\delta)), \tag{2.26}$$

that is, to a point (z^*,δ^*) such that $H(z^*,\delta^*)=0$.

Numerical solution of this two-dimensional system is straightforward using a Newton or pseudo-Newton method; we employ Broyden's method [39]. Recall that finite difference approximations, such as those used in the secant method, are underdetermined in more than one dimension. The idea of Broyden's method is to begin with an initial approximation to the Jacobian, the identity in our case, and improve it at each iteration by taking the solution of the finite difference

approximation that minimally modifies (in the Frobenius norm) the current approximation. Using double precision arithmetic, we generally define convergence as $|H(z^*, \delta^*)| < 10^{-10}$; however, orbits were often found to higher precision. A maximum of 75 Broyden iterations were performed.

An example of the dependence of (z^*, δ^*) on ε for three low-period orbits is shown in Fig. 2.3; note that the dependence on ε appears to be smooth. Orbits with periods up to $\mathcal{O}(10^5)$ and moderate values of ε can be easily found. Moreover, we are able to find symmetric orbits for any coprime (m, n) and any pair S_i, S_f as listed in Table 2.1.

It is important to note that errors can be compounded in these calculations. While the half-orbit error was always smaller than 10^{-10}, the error for the full orbit,

$$\kappa \equiv |x_n - x_0 - m| + |z_n - z_0|, \tag{2.27}$$

was often larger, but generally no more than 10^{-8}. Of course when the orbit was stable or nearly stable, i.e., $R = \mathcal{O}(1)$, the error κ was typically smaller.

Unstable orbits are difficult to find because the derivative of H becomes large and the algorithm becomes extremely sensitive to the initial guess. This can be partially obviated by using continuation from the trivial case $\varepsilon = 0$ where the initial conditions are given by (2.17). We found quadratic extrapolation to be sufficient to predict subsequent initial conditions. Extrapolation typically requires 10-15 fewer iterates of the Broyden method, allows larger steps in ϵ, and converges for larger residue values.

To maintain convergence, the extrapolation step size must decrease as the orbit period grows. To start, the simple choice $\Delta\varepsilon = 0.1n^{-1}$ yields few convergence failures. If successful, the step size is increased by half. If unsuccessful, the step size is decreased by a third. Though this process generally results in more failed steps, it proved far faster than a method with a fixed step size.

2.4 Computing Residues

Given numerical values of (z^*, δ^*) for an (m, n)-orbit, the residue (2.25) is obtained by multiplying the successive Jacobian matrices along the orbit to compute $\mathrm{tr}(Df^n)$. Every (m, n)-orbit

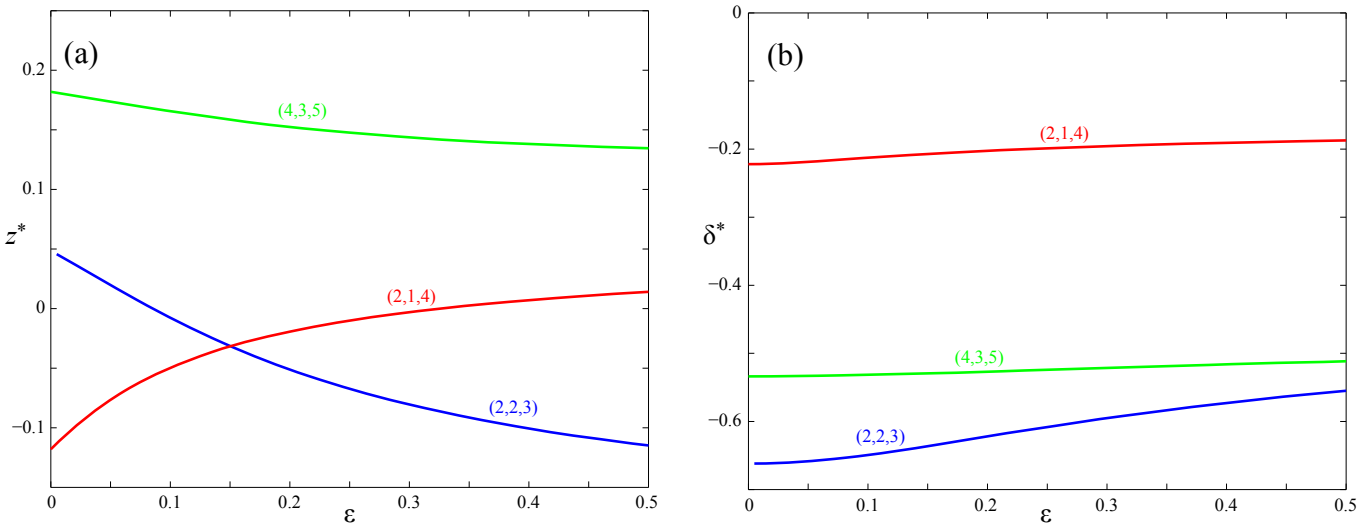

Figure 2.3: Numerically computed (z^*, δ^*) for three low-period orbits beginning on $\mathrm{Fix}(S_1)$ as a function of ε using a step size of 0.005

has zero residue at $\varepsilon = 0$ and we observe that R grows or decreases smoothly with ε. The behavior is initially monotone, but for intermediate values it often oscillates, as can be seen for several low-period orbits with $(x^i, z^i) \in \mathrm{Fix}(S_1)$ in Fig. 2.4. For example, the residue of the $(2,1,4)$ orbit (red curve) initially becomes negative, reaching a minimum near $\varepsilon = 0.04505$ and subsequently grows monotonically, passing $R = 1$ near $\varepsilon = 0.1146$. The residue of the $(1,3,4)$ orbit (black curve), on the other hand, is initially positive, but reaches a maximum near $\varepsilon = 0.09815$, and then decreases monotonically thereafter. The residues of higher period orbits can oscillate several times, but always appear to grow monotonically for large ε.

Note that the residue for fixed points and period-two orbits either grows linearly or quadratically for small ε (except for the $(e,o,1)$ orbits which have zero residue), recall Table 2.2. Surprisingly, we observe that linear or quadratic growth holds for higher periods as well, some samples are shown in Fig. 2.5. There does not appear to be a simple relation between the period or type of orbit and the small-ε asymptotic behavior. For example, we observed the growth rates:

$$R = \begin{cases} \mathcal{O}(\varepsilon) & : \ (1,1,3),(2,2,3),(2,3,3),(3,2,3),(3,3,4),(1,4,4),(3,4,4),(4,3,4),(1,1,5),\ldots \\ \mathcal{O}(\varepsilon^2) & : \ (1,2,3),(2,1,3),(2,1,4),(1,3,4),(3,2,4),(1,3,5),(3,2,5),(4,2,5),(4,3,5),\ldots \end{cases}.$$

when $\varepsilon \ll 1$, independent of the initial symmetry lines.

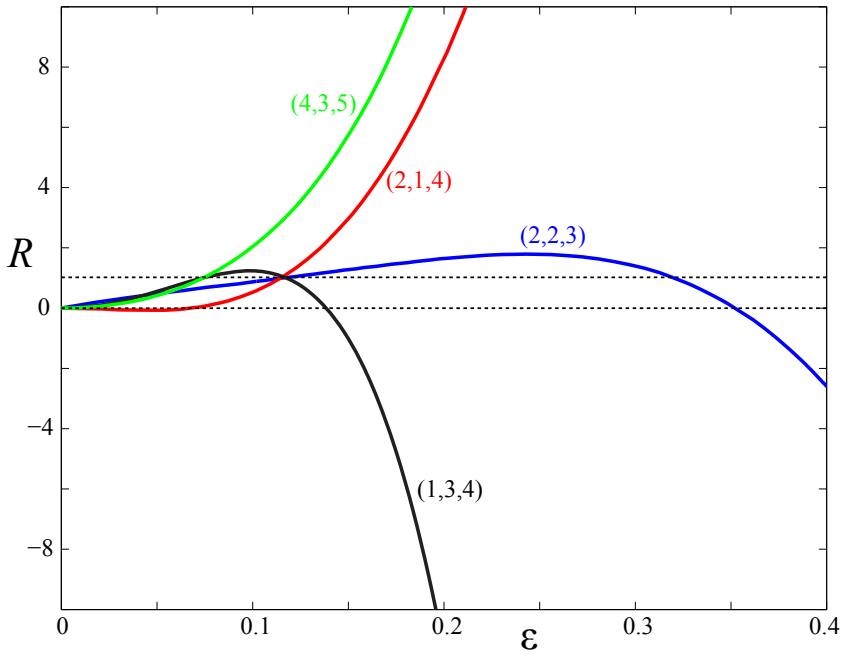

Figure 2.4: Residue as a function of ε for four (m,n)-orbits of (2.12) that start on $\mathrm{Fix}(S_1)$. The bifurcation values $R=0$ and $R=1$ are indicated by dashed lines.

This asymptotic behavior contrasts with the behavior of the standard map, where $R=\mathcal{O}(\varepsilon^n)$ for $\varepsilon \ll 1$ [54]. An explanation for our observations could follow from a perturbation analysis of the periodic orbits. This would require a generalization of the Poincaré-Birkhoff theorem to the volume-preserving case to establish the existence of these orbits, but we know of no such result.[1]

Greene also observed that for the standard map, $R=\mathcal{O}(\varepsilon^n)$ for $\varepsilon \gg 1$. We similarly observe that most of the residues of (2.12) grow as ε^n, two examples are shown in Fig. 2.5. However, there are exceptions: every symmetry line has a class of orbits—those listed in Table 2.3—for which the residue grows as ε^{n-1}. Moreover, on $\mathrm{Fix}(S_1 \circ T_{0,1})$ the residues of all orbits have this lower growth rate.

As we observe in Fig. 2.4, the sign of the residue varies with the orbit and with ε. Greene and MacKay found that the standard map has a special symmetry fixed set, the so-called **dominant** set, on which every orbit of the standard map has positive residue [77]. This holds as well in other

[1] For example, Cheng and Sun's generalization of Poincaré-Birkhoff applies to invariant circles, not periodic orbits [29].

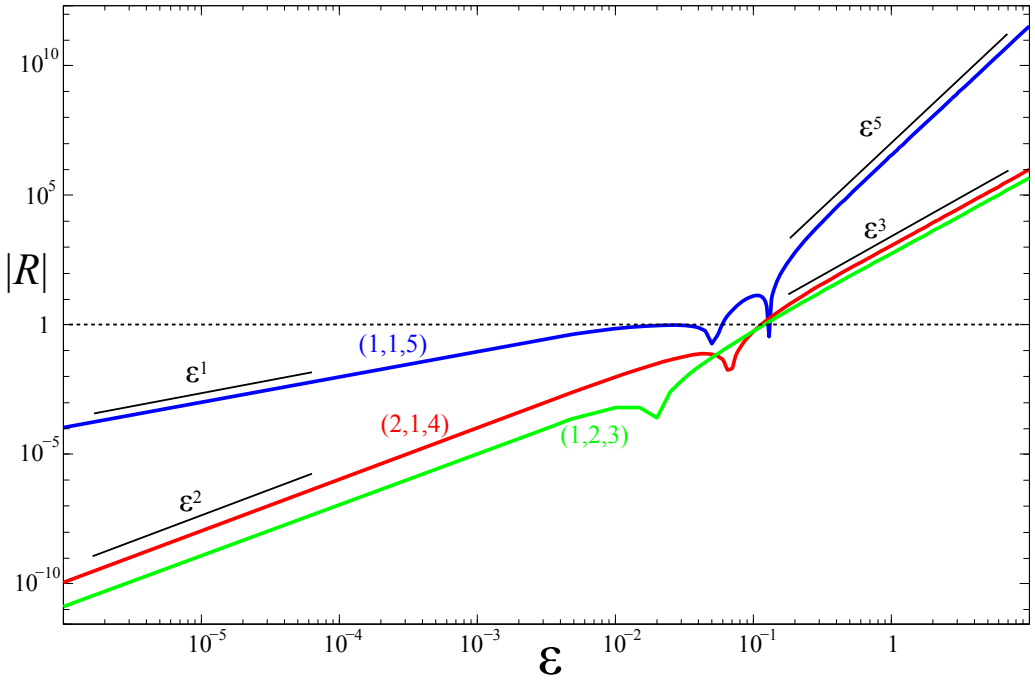

Figure 2.5: Residue as a function of ε for three orbits of (2.12) that start on $\mathrm{Fix}(S_1)$ plotted on a log-log scale. The cusps correspond to points where R changes sign. The asymptotic behavior is indicated by the line segments.

two-dimensional examples [103]. To our knowledge no such result is known for higher-dimensional maps, though there is some numerical evidence of a dominant symmetry for the 4D Froeshlé map [65].

To determine whether the map (2.12) has a dominant symmetry, we looked at a number of (m, n)-orbits of each symmetry and parity type. The results are summarized in Table 2.4, which indicates the stability of the orbit on each of the eight symmetry fixed sets. Unfortunately, we were unable to find any systematic organization of residue signs on any fixed set. One pattern that seems to hold is that for small, positive ε, there appear to be two elliptic, $0 < R < 1$, and two hyperbolic, $R < 0$, orbits for each (m, n); these are labeled e_i and h_i for $i = 1, 2$ in Table 2.4. This does not hold, however, for large ε: the asymptotic sign of the residue as $\varepsilon \to \infty$ is indicated by the $\pm$ signs in the table.

The accuracy of the residue computations is less than that of the orbit itself because multiplication of the Jacobian matrices along the orbit gives rise to additional error. Roughly speaking,

for fixed matrices A and B and $\kappa \ll 1$,

$$\mathrm{tr}((A+\kappa B)^n) \approx \mathrm{tr}(A^n) + \mathcal{O}(n\kappa\mu^{n-1})$$

where μ is the largest eigenvalue of A. For the residue computation we can think of μ as an estimate of the Lyapunov multiplier or mean residue of the orbit, and thus the relative error in the residue is of order $\frac{n\kappa}{\mu}$. If κ were fixed and $\mu = \mathcal{O}(1)$, the error would grow linearly with the period. However, as the period grows, the orbit error κ, (2.27), increases because of the floating point errors in the computation of (2.26).

This error estimate for the residue computations is shown in Fig. 2.6(a) for a period 5842 orbit. When $\varepsilon < 0.023$, $|R| < \mathcal{O}(10^{-7})$, and the error makes the residue essentially uncomputable; however, the main point is that all of the multipliers for small ε are essentially 1.0. When the orbit loses stability, near $\varepsilon = 0.025$, it does so rapidly reaching $R = 10,010$ at $\varepsilon = 0.0265$, and the estimate indicates that when $10^{-7} < |R| < 10^4$, the relative error in R is small. Note that even when $R \sim 10^4$, the Lyapunov multiplier of this orbit is $\mu \sim R^{1/n} = \mathcal{O}(1)$; consequently the error in the residue is still of order $n\kappa$.

The residue as a function of period for 35 orbits for $\varepsilon = 0.01$ is shown in Fig. 2.6(b), together with the error estimate. This particular sequence of orbits corresponds to the Farey sequence of approximants of the "spiral mean" rotation vector that will be studied in §2.5.1. For this ε, these orbits become increasingly stable as the period grows. While we are not able to obtain an accurate value for the residue when $n > 300$, we can nevertheless be sure that it is very small: the multipliers of these orbits sit very close to the point $\tau = 3.0$. We will argue in §2.6.1 that this sequence of periodic orbits appears to converge to an invariant torus.

S_1	$S_1 \circ T_{0,1}$	$S_1 \circ T_{1,0}$	$S_1 \circ T_{1,1}$	S_2	$S_2 \circ T_{0,1}$	$S_2 \circ T_{1,0}$	$S_2 \circ T_{1,1}$
(e,o,e)	All	(o,o,e)	(o,e,e)	(e,o,o)	(e,e,o)	(o,o,o)	(o,e,o)

Table 2.3: Classes of orbits for which $R = \mathcal{O}(\varepsilon^{n-1})$ for $\varepsilon \gg 1$, grouped by symmetry line. Orbits not listed have $R = \mathcal{O}(\varepsilon^n)$ for $\varepsilon \gg 1$.

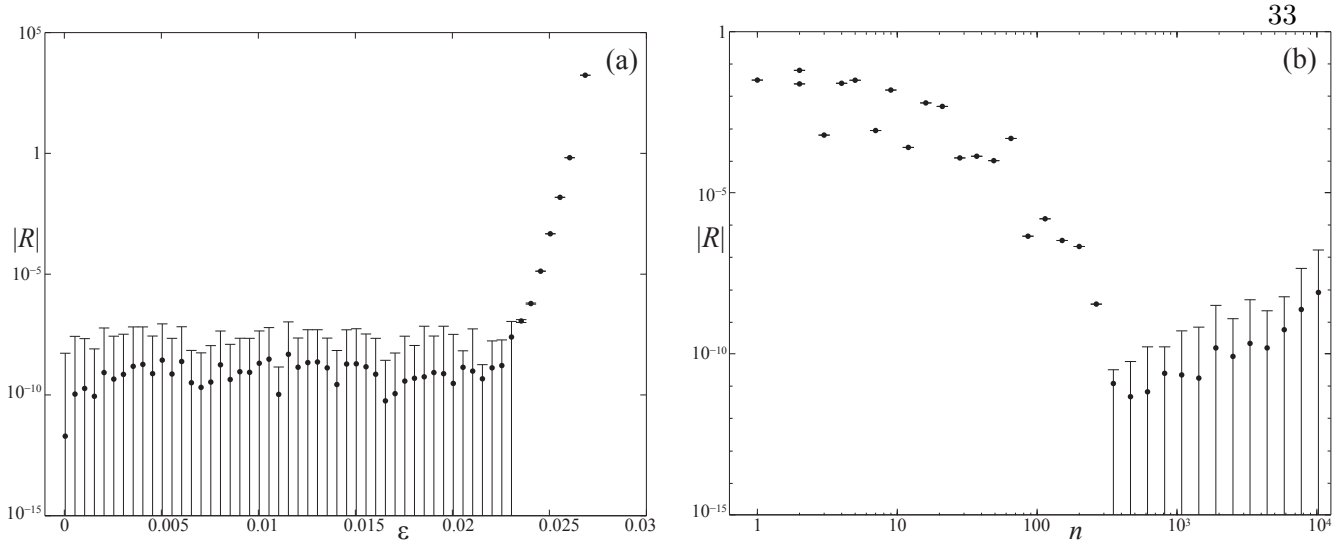

Figure 2.6: (a) Residue of the $(1897, 4410, 5842)$, $\mathrm{Fix}(S_1)$ orbit as a function of ε. (b) Residues of a sequence of $\mathrm{Fix}(S_1)$ orbits with periods 1 to 17991 (the orbits of Table 2.6) with $\varepsilon = 0.01$. The bars indicate the estimated error $\pm n\kappa$.

2.5 Farey Sequences and Periodic Orbits

As we discussed in §2.1, the application of Greene's residue criterion requires finding a suitable sequence of (m, n)-orbits whose rotation numbers converge to a chosen Diophantine rotation vector. For the $d = 1$ case, these can be systematically obtained either using continued fractions—for which the successive convergents (2.3) are "best approximants"—or the Farey tree—which gives, in addition to the convergents, intermediate approximants (see the review in App. B).

There is no multi-dimensional generalization of the continued fraction algorithm that is guaranteed to give exactly the sequence of best rational approximants to a given irrational vector, though there are strongly convergent algorithms [67, 63]. In lieu of these, we will use Kim and Ostlund's generalization of the Farey tree, see App. B, to generate rational approximations to incommensurate rotation vectors [64].

This generalized Farey-tree is a recursively-generated, binary tree that produces a set of coprime integer vectors (m_1, m_2, n) contained within an initial cone formed from three selected vectors (see Fig. B.2 in App. B). Each vector in the tree corresponds to a rational rotation vector $\frac{m}{n} \in \mathbb{Q}^2$; as an illustration, the points in Fig. 2.7(a) correspond to the rotation vectors formed from

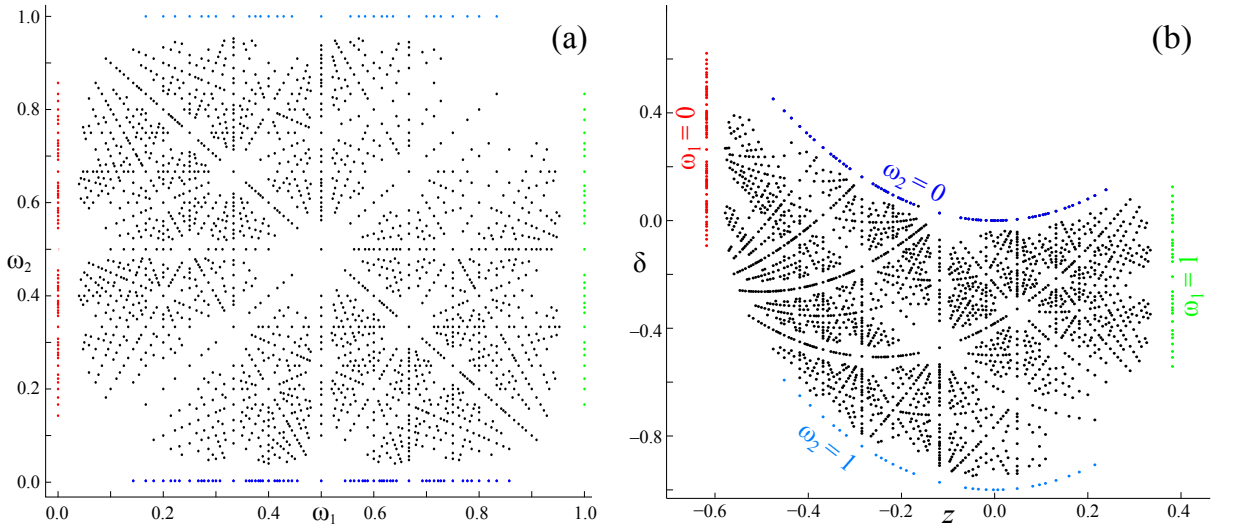

Figure 2.7: (a) The 2140 unique rotation vectors that give $(\omega_1, \omega_2) \in [0,1]^2$ on the Kim-Ostlund tree up to level 13. (b) The corresponding values $(z^*(\omega), \delta^*(\omega))$ for the (m,n)-orbits of (2.12) for $\varepsilon = 0$. Rotation vectors on the four lines $\omega_{1,2} = 0, 1$ are colored and labeled in (b).

the first 13 levels of the tree construction. Each of these can also be regarded as an (m,n)-periodic orbit of (2.12) for $\varepsilon = 0$. Indeed, using (2.17), these vectors correspond to the (z^*, δ^*) values shown in Fig. 2.7(b). Note that the transformation $\omega \mapsto (z^*, \delta^*)$ turns each line $\omega_1 = const$ into a parabola, and that since the map $\Omega(z, \delta)$, (2.7), is orientation reversing, the upper and lower boundaries of the square are flipped.

Each of the points in Fig. 2.7(b) continues to an (m,n)-orbit of (2.12) on each symmetry line for $\varepsilon \neq 0$. The orbits on $\mathrm{Fix}(S_1)$ for $\varepsilon = 0.02$ are shown in Fig. 2.8. The points are colored to indicate their residues: orbits with the smallest residues are light (yellow), those with $|R| \approx 1$ are dark (red), and those with $|R| > 1$ are black (small points). The corresponding (z^*, δ^*) values for each of these orbits, Fig. 2.8(b), are shifted from their $\varepsilon = 0$ values in Fig. 2.7(b) so as to widen the gaps around the low-order resonance curves. In phase space this correlates with the growth of tubes of secondary tori for each resonance, and these are largest for the forced resonances, $p = (0,1)$, $(1,0)$, and $(1,-1)$, of (2.11) [43]. Similar behavior has been observed in action space for symmetric orbits of the four-dimensional Froeshlé map [65].

The lightest regions in Fig. 2.8 correspond to groupings of the most stable orbits. As we will

see in §2.6, these regions also contain the most robust tori.

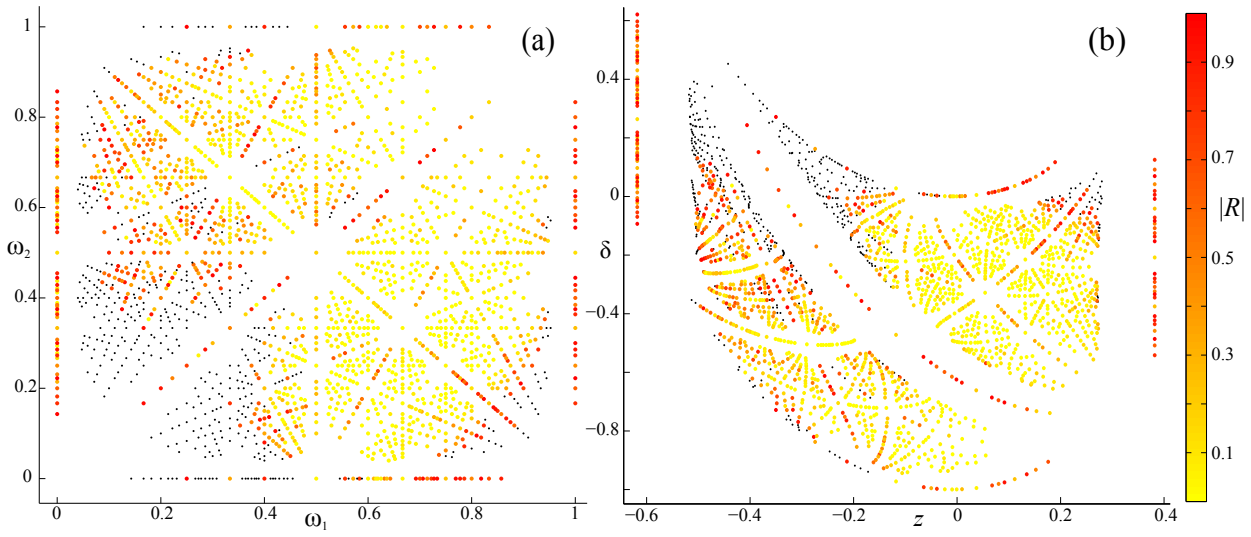

Figure 2.8: Periodic orbits of (2.12) on $\mathrm{Fix}(S_1)$ for $\varepsilon = 0.02$ with rotation vectors as in Fig. 2.7. The color indicates the magnitude of the residue, $|R| < 1$, as shown in the color bar. Orbits with $|R| \geq 1$ are shown as small, black points.

2.5.1 Spiral Mean

It is not at all clear which Diophantine vector may be an appropriate choice to replace the golden mean, (2.5), that appears to give the most robust invariant circle in the standard map. A natural conjecture, as we recall in App. C, is that—since integral bases of degree-$(d+1)$ algebraic fields give rise to Diophantine vectors—some cubic field will correspond to robust two-tori. Several candidates have been proposed for the most robust field [64, 71, 110], and invariant tori with such rotation vectors have been studied for 4D symplectic maps, recall Chapter 1. However, the robustness conjecture has not yet, to our knowledge, been investigated. Indeed, it would be difficult to find a "last" invariant torus in the symplectic case: since the tori are not codimension one, they do not form barriers.

In the next several sections we will investigate the robustness of a set of tori in a particular

cubic field that was proposed by Kim and Ostlund [64], namely that of the **spiral mean**:

$$\begin{aligned} &\sigma^3 - \sigma - 1 = 0, \\ &\sigma \approx 1.3247179572447460. \end{aligned} \tag{2.28}$$

The field $\mathbb{Q}(\sigma)$ is naturally related to the generalized Farey tree of App. B. Indeed every vector whose generalized Farey path has an infinite tail of l's or r's corresponds to a rotation vector in $\mathbb{Q}^2(\sigma)$. Moreover, each such vector is Diophantine according to Th. 7 in App. C.

For example, the direction $(\sigma^2, 1, \sigma)$ is a basis for the integer ring $\mathbb{Z}(\sigma)$; consequently, the projection of this direction onto the plane $(\omega, 1)$ gives the Diophantine rotation vector $\omega = (\sigma, 1/\sigma) \in \mathbb{Q}^2(\sigma)$. The generalized Farey paths r^ℓ give a sequence of rational rotation vectors, $\frac{m_\ell}{n_\ell}$, that limit on this vector. We denote the infinite path for this ω by $\bar{r}$ or r^∞.

We will study in detail a similar torus for which $\omega \in [0,1]^2$, corresponding to the direction

$$llr^\infty \simeq (1, \sigma^3, \sigma^4)^T. \tag{2.29}$$

Projecting this direction onto the plane $(\omega, 1)$ gives the rotation vector

$$\omega = (\sigma - 1, \sigma^2 - 1) \in [0,1] \times [0,1]. \tag{2.30}$$

The Farey convergents for the path (2.29) are

$$llr^\ell \simeq (n_{\ell-1}, n_{\ell+2}, n_{\ell+3})^T \tag{2.31}$$

where n_ℓ obeys (C.4). Several of the vectors in this sequence are shown in Table 2.5.

When $\varepsilon = 0$, the llr^ℓ periodic orbits are, by (2.17), at

$$z_\ell = \frac{n_{\ell-1}}{n_{\ell+3}} - \gamma, \quad \delta_\ell = \beta z_\ell^2 - \frac{n_{\ell+2}}{n_{\ell+3}}. \tag{2.32}$$

These values converge geometrically to the position of the spiral torus at $\varepsilon = 0$

$$\begin{aligned} z_\infty &= \sigma - 1 - \gamma \approx -0.2933160310, \\ \delta_\infty &= \beta z_\infty^2 + 1 - \sigma^2 \approx -0.5828090783, \end{aligned}$$

as can be seen in Fig. 2.9(a). Indeed, from (C.5) $n_\ell \sim a_0\sigma^\ell + \mathcal{O}(\sigma^{-\ell/2})$, so the convergents approach this point geometrically at a rate $\sigma^{-3/2}$; for example,

$$z_\ell \approx z_\infty + \frac{0.6037}{\sigma^{3\ell/2}} \cos(\ell\theta + 0.4892) + \mathcal{O}(\sigma^{-3\ell}) \tag{2.33}$$

with θ from (C.1). The values $\delta_\ell \to \delta_\infty$ at the same rate as z, as can easily be shown from (2.32).

The line in Fig. 2.9(a) corresponds to (2.33) with the cosine replaced by 1; it is an effective upper bound to the values (2.32). The modulation of this geometrical convergence by the phase θ is illustrated by the (green) curve in the figure, which is obtained from (2.32) by treating ℓ as a continuous variable. The near periodicities of the discrete levels can be explained by the fact that $\theta \approx \frac{4\pi}{5}$ and even more closely $\theta \approx \frac{10\pi}{13}$.

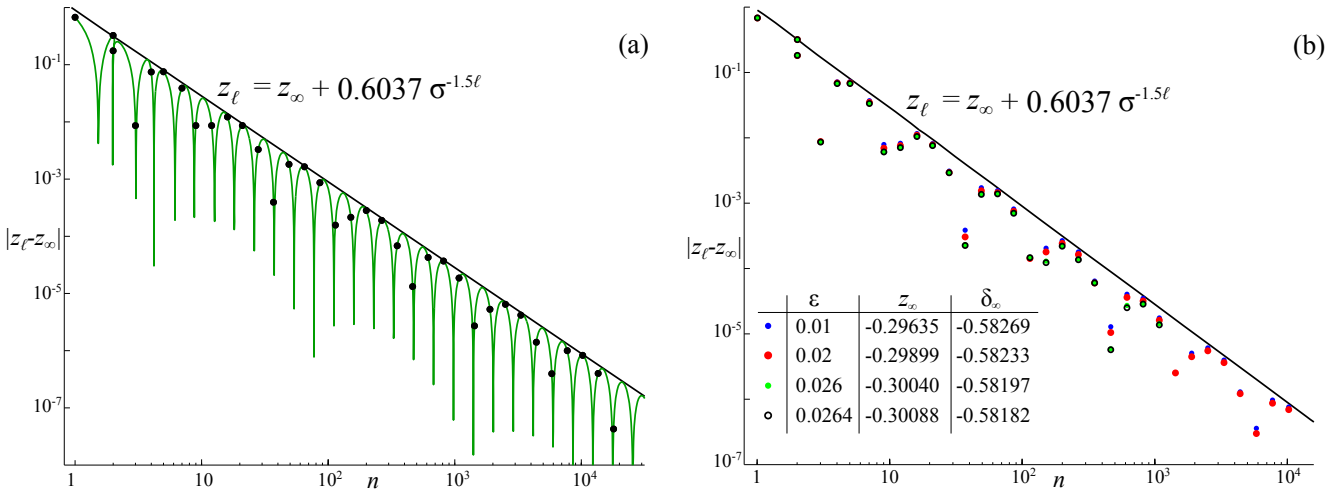

Figure 2.9: The initial action for the first 35 approximants to llr^∞ for (a) $\varepsilon = 0$ and (b) four cases with $\varepsilon > 0$. The curve (green) in panel (a) is the exact result (2.32) upon extending the level ℓ to a continuous variable. The line (black) in both panels is the upper bound of the asymptotic result (2.33) with slope $-\frac{3}{2}$ on the log-log scale.

It is interesting that the geometric convergence of $z_\ell \to z_\infty$ appears to be maintained for $\varepsilon > 0$—computations of the actions of orbits for the spiral convergents for four values of ε are shown in Fig. 2.9(b). In this figure, data is not shown for periods larger than 10^3 for the two largest values of ε (0.026 and 0.0264) because the orbit finding algorithm did not converge. Note that even though, as shown in the inset, the converged point $(z_\infty, \delta_\infty)$ varies with ε, the geometric convergence rate is consistent with the $\varepsilon = 0$ value $\sigma^{-3/2}$; however, there is some indication that

the convergence rate could be faster for the larger two ε's. Unfortunately, the oscillations make it difficult to extract a precise rate. As we will see below, for $\varepsilon > 0.0259$ the torus seems to be destroyed, and by analogy with the standard map, a different convergence rate might be expected [81].

2.6 Residue Criterion for a Spiral Mean Torus

An invariant torus on which the dynamics is diffeomorphic to rigid rotation must have each Lyapunov multiplier corresponding to its tangent directions equal to one. Consequently, all of the multipliers of a codimension-one torus in a volume-preserving map must be one. Thus a natural conjecture is that the multipliers of a sequence of periodic orbits that limit on such a torus should all limit to one. Similar considerations for the symplectic case led to the residue bounds discussed in §2.1. As a consequence, for the three-dimensional volume-preserving case, periodic orbits in the neighborhood of a smooth invariant torus should have stability parameters near the point $\tau_1 = \tau_2 = 3$ that corresponds to a triple-one multiplier, recall Fig. 2.2.

When the map is reversible and the reversor fixed sets are graphs over the action (as in (2.21)), then every rotational invariant torus will contain symmetric orbits. If the torus has an incommensurate rotation vector, then these orbits will be dense. Thus it seems sensible to investigate the existence of such tori by looking for sequences of symmetric periodic orbits whose residues, (2.25), approach zero.

2.6.1 Critical Spiral Torus

In this section, we study the sequence of periodic orbits (2.31) whose rotation vectors converge to the Diophantine vector (2.30). Figure 2.6(b) showed that the residues of these orbits appear to converge to zero as $\ell \to \infty$ when ε is fixed and small. Figure 2.5, however, showed that the residue of each orbit grows geometrically with ε. Indeed, as can be seen in Fig. 2.10(a), the onset of this growth becomes more sudden as the period is increased. The residues of low-period spiral mean approximants begin to grow near $\varepsilon \approx 0.03$, while for $\ell > 23$, the onset of rapid growth in R occurs

near $\varepsilon = 0.26$. For larger period spiral approximants, as shown on a log scale in Fig. 2.10(b), rapid growth in R begins near $\varepsilon \approx 0.0259$. This evidence suggests that the llr^{∞} torus does not exist for $\varepsilon > 0.0259$.

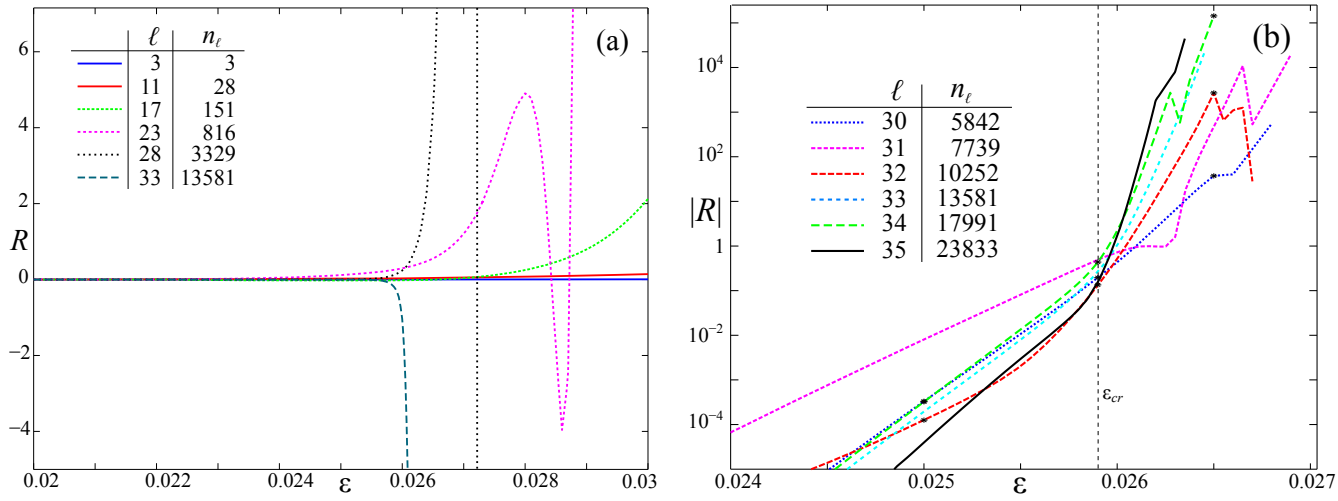

Figure 2.10: Residue as a function of ε for Fix(S_1) orbits with rotation vectors to llr^{ℓ} for (a) six low-period orbits, and (b) six longer period orbits near ε_{cr}. The stars indicate the residues for the three values of ε shown in Fig. 2.12.

To more systematically investigate the residue criterion, we choose a threshold residue, R_{th}, and compute the smallest positive ε for which the level ℓ orbit has $|R| = R_{th}$; call this value $\varepsilon_{R_{th}}$. Computationally, we continue each orbit in ε, as discussed in §2.3, until R_{th} is bracketed. Bisection is then used to find $\varepsilon_{R_{th}}$ as precisely as possible. The threshold ε values are shown for the first 36 levels, up to period 31572, in Table 2.6. These thresholds appear to converge to

$$\varepsilon_{cr} = 0.02590 \pm 5(10)^{-5}, \tag{2.34}$$

independently of R_{th}. Computations for the spiral mean orbits on the other symmetry lines gave the same result.

The convergence of the thresholds to ε_{cr} with period is geometric, as shown in Fig. 2.11 for $R_{th} = 0.9$. A least squares fit to this data gives

$$\varepsilon_{\ell} = \varepsilon_{cr} + (0.17 \pm 0.06) n^{-0.79 \pm 0.02}. \tag{2.35}$$

It is perhaps interesting that the rate of convergence, 0.79, is close to, but significantly different from, $\sigma^{-1} \approx 0.75488$.

It is important to remember that each convergent periodic orbit exists only for a particular $\delta(\varepsilon)$, as determined by (2.18). The threshold values $\delta(\varepsilon_\ell)$ converge to

$$\delta_{cr} = -0.58192 \pm 5(10)^{-5},$$

and the convergence is geometric, just like that of ε_ℓ itself, however, rate is now 1.1 ± 0.1 and there are oscillations like those observed in Fig. 2.9 for z_ℓ at fixed ε.

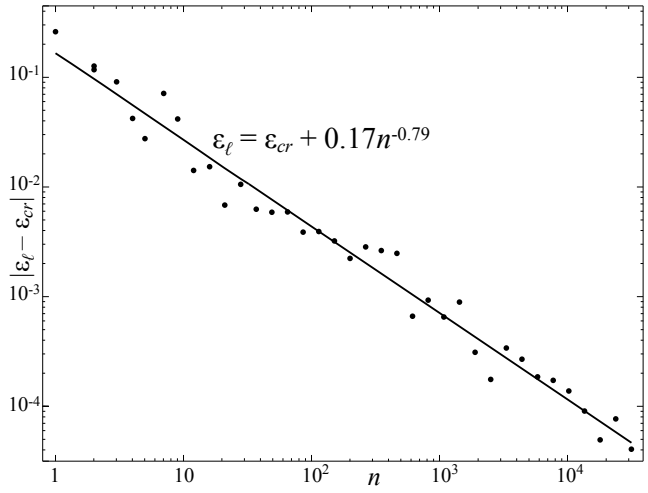

Figure 2.11: The ε values for $R_{th} = 0.9$ for the first 36 approximants to llr^∞ using $\varepsilon_{cr} = 0.02590$.

2.6.2 Supercritical Tori

These results imply that the llr^∞ torus appears to be critical at $\varepsilon_{cr} \approx 0.02590$. The limit of the initial conditions for the Fix(S_1) periodic orbits at this value is

$$(x_\infty, z_\infty, \delta_\infty) \approx (0, -0.30054, -0.58192).$$

This orbit appears to lie on a critical spiral mean torus.

By analogy with the area-preserving case, we expect that when $\varepsilon > \varepsilon_{cr}$, the llr^ℓ orbits will still converge to a quasiperiodic orbit, but one that is hyperbolic and whose closure is no longer a

torus; indeed, for twist maps the supercritical orbits are dense on Cantor sets. Figure 2.12 gives a visualization of this for our map: it shows the phase portraits of three spiral approximants for three values of ε near ε_{cr}. The residues for these nine cases were marked with a $*$ in Fig. 2.10(b). When $\varepsilon < \varepsilon_{cr}$ (the left column of Fig. 2.12) the approximating orbits are stable and as the period is increased the points appear to limit to a smooth, nonzero density on a smooth torus. In the middle column of the figure, where $\varepsilon = \varepsilon_{cr}$, the density becomes less smooth, and in the right column, where $\varepsilon > \varepsilon_{cr}$, the limiting density appears to have holes. This can be better seen in Fig. 2.13 which shows the projection of the $\ell = 34$ approximant onto the (x, y) plane.

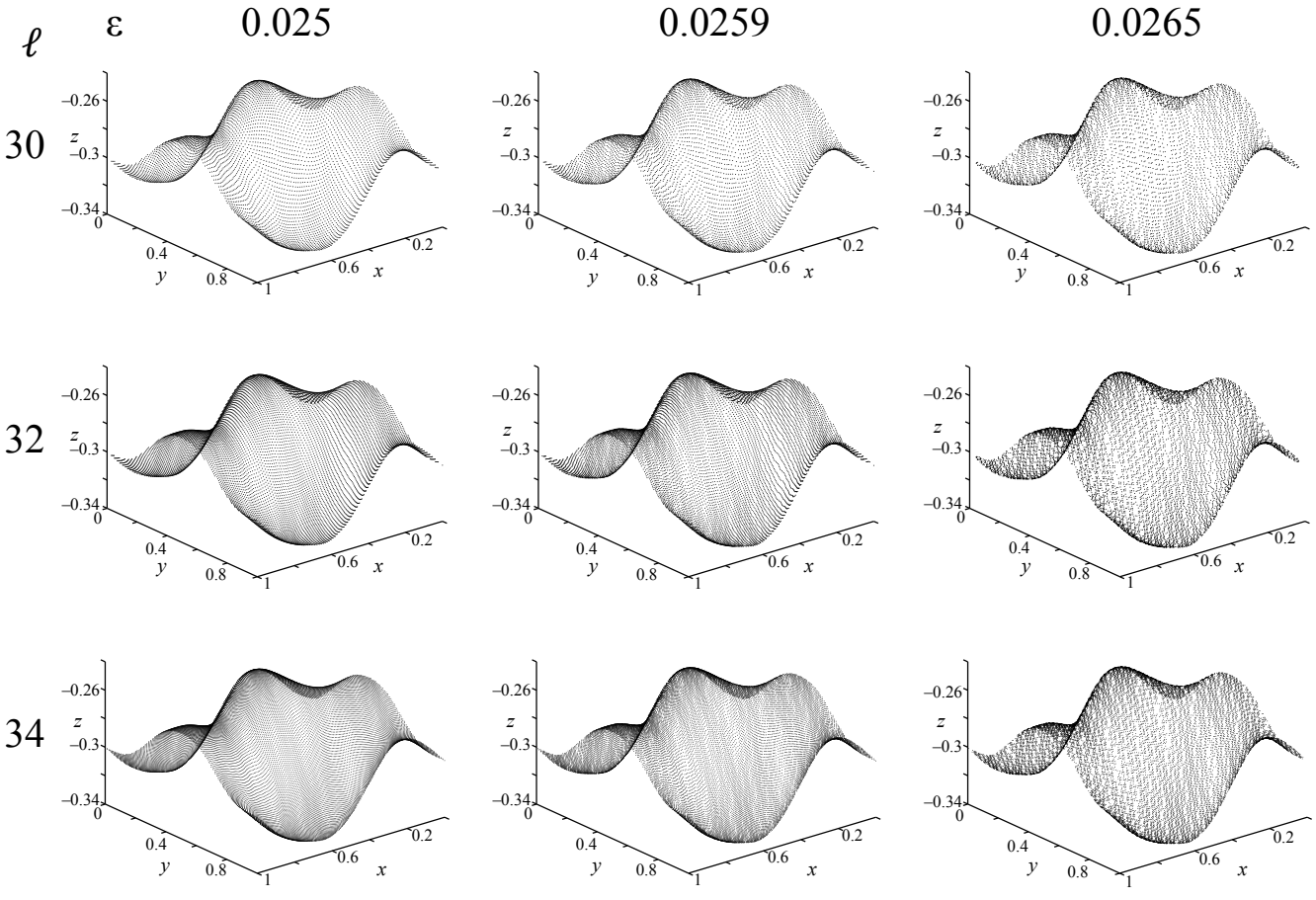

Figure 2.12: Phase portraits of the periodic orbits llr^{30}, llr^{32}, and llr^{34} (rows) on Fix(S_1) for three ε values (columns). For $\varepsilon < \varepsilon_{cr} \approx 0.0259$ the orbits appear to limit on a smooth torus. At ε_{cr} the density is nonuniform, and when $\varepsilon > \varepsilon_{cr}$ the orbits seem to limit to a torus with holes.

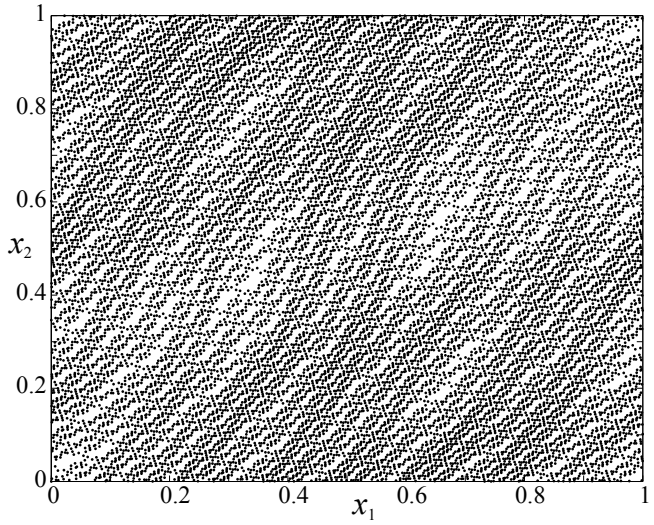

Figure 2.13: Projection of the Fix(S_1) spiral approximant llr^{34}, with $(m, n) = (5842, 13581, 17991)$, onto the angle-plane for $\varepsilon = 0.0265$.

2.6.3 Varying Parameters

Up to this point we have studied only the standard parameter set (2.13); in this section we vary the parameter c in the force (2.11). Note that the map (2.12) is invariant under the replacement $(x, \varepsilon, c) \to (x + (\frac{1}{2}, \frac{1}{2}), -\varepsilon, -c)$. Since we have observed that ε_{cr} is the same for the Fix(S_1) and the Fix($S_1 \circ T_{1,1}$) orbits, the critical graph $(\varepsilon_{cr}, c_{cr})$ will be symmetric under reflection through the origin. Thus we study only positive values of ε.

Figure 2.14 shows the critical set $(\varepsilon_{cr}, c_{cr})$ of the spiral torus (2.29) for $c \in [-2, 2]$, holding the remaining parameters fixed according to (2.13). On this scale, ε_{cr} appears to be a graph over c, and for $c < 0$ this graph appears to grow smoothly as c increases. The peak value, $\varepsilon_{cr} \approx 0.06156$, occurs at $c_{cr} \approx 0.07281$. Though the graph appears to decrease monotonically for larger c values, this is not the case: there are a number of cusps. These appear to be associated with an increasing number of oscillations in the function $R(\varepsilon)$ before it settles into its asymptotic growth, recall §2.4. An enlargement near the most prominent cusp is shown in Fig. 2.14(b).

The oscillations in $R(\varepsilon)$ make it harder to obtain accurate values for the critical parameters near each cusp. To resolve the cusp shown in Fig. 2.14(b), we used a longer period orbit (period

31572), and a larger threshold $R_{th} = 10$. Note that what appeared to be a single peak near $c = 0.073$ becomes, in the enlargement, a number of cusps and several possible discontinuities. Each cusp corresponds to a change of the large ε asymptotic behavior of R, and near the cusp the number of oscillations in the graph $R(\varepsilon)$ changes. We are not able to resolve the apparent discontinuities in Fig. 2.14(b)—it is possible that the critical set is not a graph over c in these regions. Several less prominent cusps are also visible in Fig. 2.14(a); the local behavior near these is similar to the one shown in the enlargement.

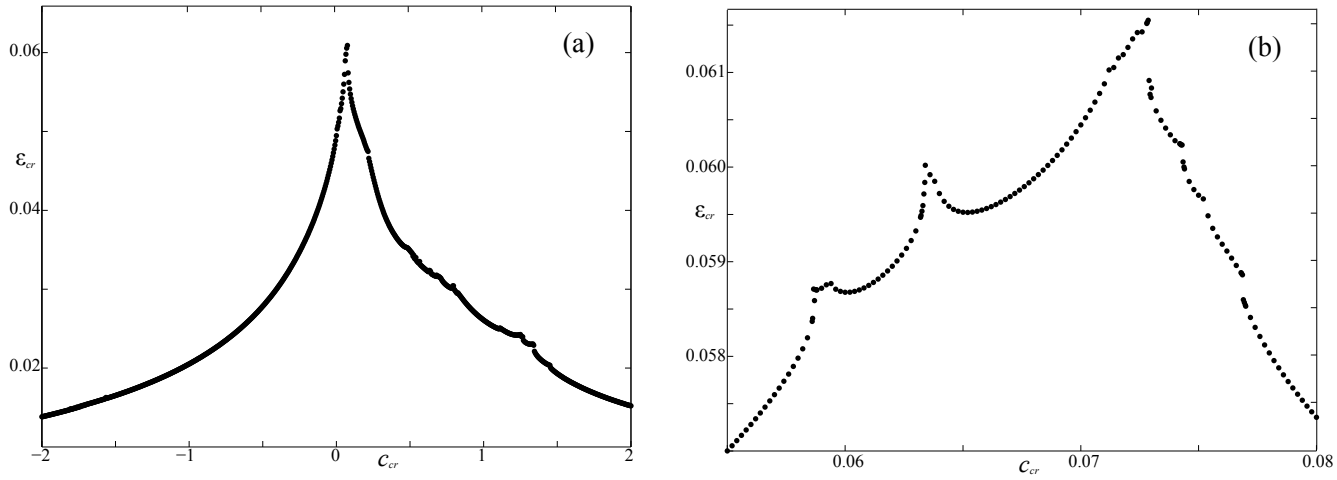

Figure 2.14: Critical set $(\varepsilon_{cr}, c_{cr})$ for the llr^{∞} torus with the remaining parameters fixed as usual at (2.13). (a) Critical set computed using the llr^{30}, period 5482, orbit with $R_{th} = 0.9$. (b) Enlargement near the peak ε_{cr} using the llr^{36} orbit with $R_{th} = 10$.

2.7 The Last Torus

The critical function, $\varepsilon_{cr}(\omega)$ is the value of ε at which the torus with rotation vector ω is first destroyed upon perturbation from integrability, $\varepsilon = 0$ (here we assume that $\delta = \beta \langle z^2 \rangle - \omega_2$, recall (2.18)). When ω is resonant, $p \cdot \omega = q$, the torus is typically destroyed immediately as ε becomes nonzero; i.e., $\varepsilon_{cr}(\omega) = 0$ at resonance. However, KAM theory implies that $\varepsilon_{cr}(\omega) > 0$ when ω is Diophantine; thus, the critical function is highly singular.

Our goal in this section is to compute $\varepsilon_{cr}(\omega)$ and to identify the most robust torus of our model (2.12). Ideally we would like to discover the analogue of the golden mean, which, as Greene

conjectured, appears to give the most robust invariant circle of the standard map (1.15). Though there is considerable numerical support for Greene's conjecture, it has never been proven.[2] Strong numerical evidence also indicates that invariant circles with "noble" rotation numbers,

$$\omega = \frac{a\phi + b}{c\phi + d} \ , \ \text{with } ad - bc = \pm 1,$$

are **locally** robust for area-preserving maps, see Chapter 5 [98, 84]. That is, in any interval of rotation numbers the most persistent invariant circle has a noble rotation number. Recall that each noble number is the projection of the integral basis $(a\phi + b, c\phi + d)$ of $\mathbb{Z}(\phi)$ onto $(\omega, 1)$.

2.7.1 Critical Function

Thus it is natural to conjecture that the most robust tori for a two-angle map may correspond to integral bases of some cubic field. As a preliminary investigation, we will compute the critical function for bases of $\mathbb{Z}(\sigma)$. Recall from App. C that $v_{\bar{r}}$ (C.2) is one such integral basis and that every other integral basis is obtained from $v_{\bar{r}}$ by multiplication with some element of $SL(3, \mathbb{Z})$. To construct a sampling of these matrices we will use the 2^ℓ directions on the generalized Farey tree at level ℓ, recall App. B. To each path $h = i_1 i_2 \dots i_\ell$ with $i_j \in \{r, l\}$ there is a corresponding matrix $C_{i_1} C_{i_2} \dots C_{i_\ell} \in SL(3, \mathbb{Z})$ using (B.1). Therefore, the direction

$$v_p = C_{i_1} C_{i_2} \dots C_{i_\ell} v_{\bar{r}} \ , \quad i_j \in \{l, r\},$$

is an integral basis for $\mathbb{Z}(\sigma)$ with path $p = h\bar{r}$. We refer to h as the **head** and $\bar{r}$ as the **tail** of this path. As we remarked in App. B some of the finite paths at level ℓ on the generalized Farey tree correspond to duplicated directions; however, the 2^ℓ directions obtained by appending the infinite tail $\bar{r}$ are unique.

The projection of each v_p onto $(\omega_p, 1)$ gives a rotation vector ω_p whose components are Diophantine by Th. 7. Since the matrices C_l and C_r do not generate $SL(3, \mathbb{Z})$, the Farey tree does not generate all of the integral bases. Nevertheless, as was seen in Fig. 2.7, the resulting

[2] It is known that the standard map has no rotational circles when $2\pi\varepsilon > 63/64$ [83].

rotation vectors ω_p give a discrete sampling of frequency space that is sensibly more dense in the nonresonant regions.

We estimate $\varepsilon_{cr}(\omega_p)$ for each such invariant torus using the residue criterion for nearby periodic orbits. To give a reasonable approximation, but limit the computation time, we approximate the torus using the periodic orbit with path hr^k, selecting the length, k, of the tail so that the orbit has period larger than 5000. Note that the k we choose depends on the head h. We then compute the value of ε for which $|R| = R_{th} = 0.9$ for each of the corresponding periodic orbits hr^k.

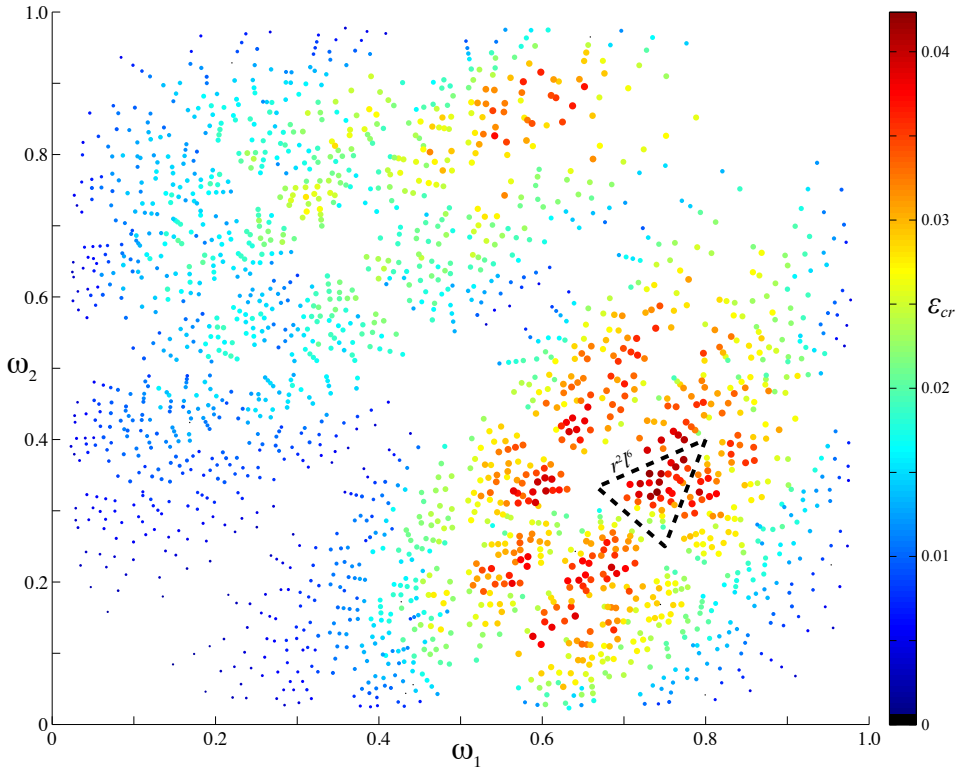

Figure 2.15: The critical function for (2.12) with the standard parameters (2.13). The values of ε_{cr} are low near the resonances, but grow into several peaks. The level-8 triangle that contains the most robust torus, r^2l^6, is shown (dashed).

To sample the tori with $\omega \in [0,1]^2$, we began by generating all of the level $\ell = 13$ heads that start with rrl or llr, namely those in the two triangles of Fig. B.2(b). The result, shown in Fig. 2.15, is an approximation to $\varepsilon_{cr}(\omega)$ on the $2 \times 2^{10} = 2048$ rotation vectors at this level. In this figure, the size of the dots (and their color, as shown in the color bar) is proportional to $\varepsilon_{cr}(\omega_p)$.

Note that there are several local peaks in the critical function, and that it tends to be small near low-order resonance lines. The most robust torus in this figure has the path $p = r^2l^6r^3l^2r^k$ with $k = 19$; this corresponds to $(m, n) = (3901, 1718, 5268)$, or rotation vector $\omega_p \approx (0.7405, 0.3261)$. For this torus, $\varepsilon_{cr}(\omega_p) = 0.0424$.

Hypothesizing that the most robust torus is nearby, we zoom-in by focusing on the level-8 triangle

$$r^2l^6 \simeq \begin{pmatrix} 2 & 3 & 4 \\ 1 & 1 & 2 \\ 3 & 4 & 5 \end{pmatrix}$$

that contains this vector, i.e., the dashed triangle in Fig. 2.15. We now generate the 2^9, level-17 paths within this triangle, i.e., each path of length 17 that begins with r^2l^6. Appending r^k to each of these to give a periodic orbit with period larger than 5000, gives the zoomed-in view of the critical function shown in Fig. 2.16(a). The most robust torus of the 512 sampled vectors has $\varepsilon_{cr}(\omega_p) = 0.0479$. It has the path $p = r^2l^6(rlr)^2lr^2r^k$ with the $k = 17$ approximation $(m, n) = (4276, 2081, 5806)$. We again zoom-in near the most robust torus, incrementing the level of the base triangle by three, and focusing now on the level-11 triangle

$$r^2l^6rlr \simeq \begin{pmatrix} 6 & 2 & 7 \\ 3 & 1 & 3 \\ 8 & 3 & 10 \end{pmatrix}.$$

The critical function for another 2^9 rotation vectors using this level-11 triangle as the base is shown in Fig. 2.16(b). The most robust rotation vector at this stage has the path $p = r^2l^6(rlr)^2l^5rr^k$ with its $k = 14$ approximation $(m, n) = (4670, 2278, 6353)$ and $\varepsilon_{cr}(\omega_p) = 0.0485$. This vector is contained in the level-14 triangle

$$r^2l^6(rlr)^2 \simeq \begin{pmatrix} 13 & 6 & 14 \\ 6 & 3 & 7 \\ 18 & 8 & 19 \end{pmatrix},$$

which is outlined in Fig. 2.16(b).

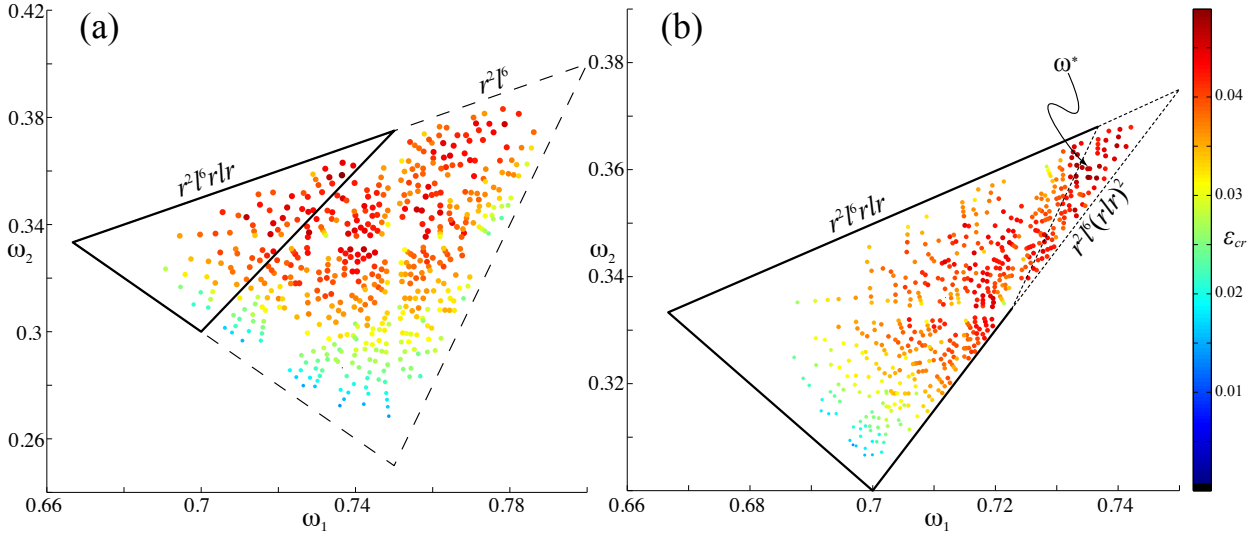

Figure 2.16: Enlargements of the critical function for two "most robust" triangles, showing ε_{cr} for 512 rotation vectors in the spiral field that have heads nine levels down from their respective triangles. (a) Enlargement of the triangle r^2l^6 (dashed) from Fig. 2.15. The level-11 triangle, r^2l^6rlr containing the most robust torus is also shown (solid). (b) Enlargement of the level-11 triangle from (a), and the level-14 triangle (small dashes) containing the most robust torus at this stage. The location of the most robust rotation vector at level-38 is denoted by ω^*.

Continuing in this fashion, we increment the level of the base triangle by three and then find the most robust torus among 2^9 rotation vectors within this triangle. The peak of the critical function increases with each zoom, leading to the level-29 triangle

$$r^2l^6(rlr)^2r(rl)^4r^3l^3 \simeq \begin{pmatrix} 172 & 241 & 330 \\ 85 & 119 & 163 \\ 234 & 328 & 449 \end{pmatrix}. \tag{2.36}$$

The most robust torus in this triangle has path $p = r^2l^6(rlr)^2r(rl)^4r^3l^3r^2(lr)^2r^4$, giving $(m, n) = (4800, 2371, 6531)$ so that $\omega \approx (0.7350, 0.3630)$. This orbit has initial condition

$$(x^*, z^*, \delta^*) \approx (0, 0.123605791956645, -0.331972596409587).$$

The peak critical value has converged to $\varepsilon_{max} = 0.0522 \pm 0.0005$, to three significant figures. Note that the given error bound signifies the observed variation in the maximal ε values for **period** 5000 **orbits**. Since we fix the period, this ε_{max} does not necessarily represent the true maximal value of ε for infinite period. Nevertheless, this orbit is our best estimate, to period 5000, of the most

robust torus for (2.12) for the standard parameters (2.13).

To improve this result, we re-examined the level-29 triangle (2.36). As before, we use the 2^9 level $29+9$ periodic orbits within this triangle, but now add a tail r^k so that the period is at least $25,000$. Of these 512 rotation numbers the most robust torus has the path

$$p = r^2l^6(rlr)^2r(rl)^4r^3l^3r^3(lr)^3r^8, \tag{2.37}$$

which agrees for the first 31 levels with the previous one, but differs after that. This corresponds to $(m,n) = (23749, 11731, 32316)$, so that

$$\omega \approx (0.73490, 0.36301).$$

This torus is located at

$$(x^*, z^*, \delta^*) \approx (0, 0.123303207885153, -0.332181389896200)$$

and is destroyed at the critical value.

$$\varepsilon_{max} = 0.0512 \pm 0.0005. \tag{2.38}$$

This value of ε_{max} is less than the value of ε_{max} computed using the period 5000 orbits, which is consistent with the behavior seen in Table 2.6. Namely, critical ε values, by and large, decrease as the period of the approximating periodic orbits increases, limiting on the true ε_{cr} from above.

Unfortunately, unlike the noble numbers of the area-preserving case, there does not appear to be any simple pattern in the Farey sequence (2.37) of the most robust torus.

2.7.2 Crossing Time

To compare these estimates for the peak values of ε_{cr} with the dynamics we performed a "crossing time" experiment, similar to that of [90]. The point is that a rotational torus is a barrier so that any orbit that begins below the torus must remain below.

To make this computation easier, we choose a frequency map that is periodic mod-one in z, i.e., so that $\Omega(z+1) = \Omega(z) + m$ for some $m \in \mathbb{Z}^2$. In this case, the invariant sets of the map

in each unit interval of z are identical. Moreover there are no rotational invariant tori whenever there exists an orbit for which $|z_t - z_0| > 1 + \Delta$, where Δ is the maximal vertical extent of a torus. Since the first component of (2.7) satisfies the periodicity requirement, we modify only its second component:

$$\Omega_2(z) = \beta(\text{nint}(z))^2 - \delta,$$

where "nint" is the nearest integer function. Since the tori for parameters near $(\varepsilon, \delta) = (0.05, -0.3)$ are located near $z = 0.1$ and have vertical extent of order 0.1, this modification will not affect their existence or nonexistence. Of course, it certainly changes the dynamics whenever $|z| > 0.5$.

The crossing time, t_c, is defined to be the first time for which $|z_{t_c}(x_0, z_0) - z_0| \geq 1.3$. If there is an orbit with $t_c < \infty$, the map has no rotational tori with $\Delta < 0.3$. The crossing time is certainly a highly variable function of initial conditions, so we compute its distribution for a set of initial conditions. Fixing $\delta = -0.33$, we start ten orbits with $x_0 = 0$ and a random value $|z_0| < 0.001$. When $\varepsilon \geq 0.1$ all of the orbits cross within a few thousand iterates, but as ε decreases, the crossing times grow rapidly, as shown in Fig. 2.17. We found that whenever $\varepsilon < 0.0512$ none of the trajectories crossed within 10^{10} iterations. The implication, in complete agreement with (2.38), is that there must be rotational tori in this case. The median of the distribution of t_c for $0.0512 \leq \varepsilon \leq 0.10$ can be fit to the power law

$$t_c = 0.0132(\varepsilon - \varepsilon_\infty)^{-3.807},$$

with $\varepsilon_\infty = 0.05047 \pm 0.0002$ as shown in Fig. 2.17. The value ε_∞ is close to ε_{cr} of (2.38), and the difference is probably due to the weight given in the fit to points for larger values of ε, though it may also be due to the sharp dependence of ε_{cr} on δ.

Indeed, we compare the crossing time experiments for various values of δ with the critical ε values of the tori in Fig. 2.17(b). The points in the figure represent the computed $(\varepsilon_{cr}, \delta_{cr})$ for the 2048 tori of Fig. 2.15 in the *rrl* and *llr* triangles. The upper envelope of these points is an estimate of the most robust torus for a fixed δ. Since these points are not from the zoomed-in triangles, like those of Fig. 2.16, they underestimate the maximal ε_{cr}. The crosses in Fig. 2.17(b) show the

computed positions of the pole, ε_∞, in the crossing time as a function of δ. These are obtained from power law fits to crossing times experiments with a maximal iteration time of 10^{10}. Note that the maximal value of ε is a highly sensitive function of δ.

The crossing time experiments confirm that the most robust torus of (2.12) for the standard parameters (2.13) is destroyed near (2.38).

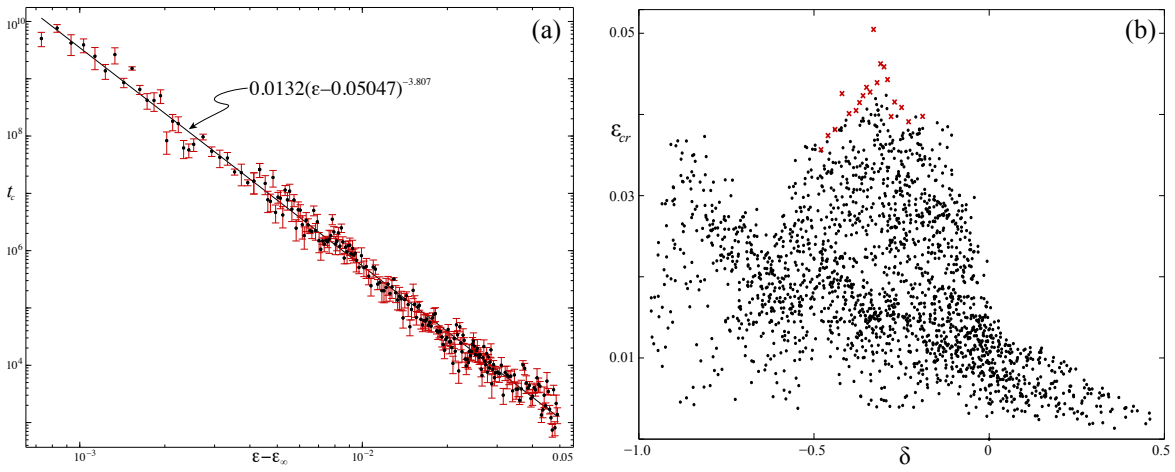

Figure 2.17: (a) Crossing time as a function of ε for orbits of (2.12) with $\delta = -0.33$. Points correspond to the median of the crossing times for each ε, and error bars to the median absolute deviation. (b) Critical ε values as a function of δ. The dots (black) are $(\varepsilon_{cr}, \delta_{cr})$ pairs for the tori of Fig. 2.15, and the crosses (red) are estimates of the pole position, ε_∞, of t_c for twenty values of δ.

Orbit	S_1	$S_1 \circ T_{0,1}$	$S_1 \circ T_{1,0}$	$S_1 \circ T_{1,1}$	S_2	$S_2 \circ T_{0,1}$	$S_2 \circ T_{1,0}$	$S_2 \circ T_{1,1}$
(2,2,3)	e_1-	h_1-	h_2-	e_2+	e_1-	h_1-	h_2-	e_2+
(4,2,5)	h_1-	h_2+	e_2+	e_1-	h_1-	h_2+	e_2+	e_1-
(2,1,4)	h_1+	h_1+	e_1+	e_1+	h_2-	h_2-	e_2-	e_2-
(4,3,4)	e_1+	e_1+	h_2-	h_2-	h_1+	h_1+	e_2-	e_2-
(2,1,3)	e_1+	h_1+	e_2-	h_2-	h_1+	e_1+	h_2-	e_2-
(4,3,5)	e_1-	h_1+	e_2-	h_2+	h_1+	e_1-	h_2+	e_2-
(1,4,4)	h_1+	e_1+	h_1+	e_1+	e_2-	h_2-	e_2-	h_2-
(3,2,4)	e_1+	h_1+	e_1+	h_1+	h_2+	e_2+	h_2+	e_2+
(1,2,3)	h_1+	h_2-	e_1+	e_2+	e_1+	e_2+	h_1+	h_2-
(3,2,5)	e_1+	h_1+	h_2+	e_2+	h_2+	e_2+	e_1+	h_1+
(1,3,4)	e_1-	e_2-	e_2-	e_1-	h_1-	h_2-	h_2-	h_1-
(3,3,4)	e_1-	h_1-	h_1-	e_1-	e_2+	h_2-	h_2-	e_2+
(1,1,3)	e_1+	h_1-	h_2-	e_2-	e_2-	h_2-	h_1-	e_1+
(1,3,5)	h_1+	e_2-	e_1-	e_2-	e_2-	e_1-	e_2-	h_1+

Table 2.4: Signs of the residues of symmetric orbits of each parity on each of the eight symmetry fixed sets for (2.12) with parameters (2.13). Orbits are labeled by stability for small positive ε ("e" for elliptic and "h" for hyperbolic), and by the residue sign ($\pm$) for large positive ε. For small ε there are two hyperbolic and two elliptic orbits for each (m, n), labelled by subscripts 1 and 2.

path	(m, n)	path	(m, n)
ll	$(1, 1, 1)$	llr^{20}	$(114, 265, 351)$
llr	$(0, 1, 2)$	llr^{21}	$(151, 351, 465)$
llr^2	$(1, 2, 2)$	llr^{22}	$(200, 465, 616)$
	$\vdots$		$\vdots$
llr^6	$(2, 5, 7)$	llr^{33}	$(4410, 10252, 13581)$
llr^7	$(3, 7, 9)$	llr^{34}	$(5842, 13581, 17991)$
llr^8	$(4, 9, 12)$	llr^{35}	$(7739, 17991, 23833)$
llr^9	$(5, 12, 16)$	llr^{36}	$(10252, 23833, 31572)$
	$\vdots$		$\vdots$

Table 2.5: Integer vectors for the generalized Farey paths llr^ℓ.

ℓ	n_ℓ	$\varepsilon_{0.5}$	$\varepsilon_{0.9}$	$\varepsilon_{1.5}$	ℓ	n_ℓ	$\varepsilon_{0.5}$	$\varepsilon_{0.9}$	$\varepsilon_{1.5}$
0	*1	0.159156	0.286479	0.477464	19	265	0.028418	0.028739	0.029030
1	2	0.079578	0.143239	0.238734	20	351	0.028425	0.028532	0.028650
2	2	0.121723	0.152553	0.188191	21	*465	0.027723	0.028382	0.028444
3	*3	0.097264	0.116817	0.137303	22	616	0.026147	0.026563	0.026920
4	4	0.047052	0.068028	0.154364	23	816	0.026426	0.026828	0.027130
5	5	0.038700	0.053493	0.135967	24	1081	0.026372	0.026551	0.026696
6	7	0.094469	0.097173	0.100279	25	*1432	0.026746	0.026791	0.026840
7	*9	0.032182	0.042449	0.068823	26	*1897	0.026046	0.026209	0.026341
8	*12	0.035600	0.040047	0.044786	27	2513	0.025880	0.026076	0.026218
9	16	0.038450	0.041201	0.043517	28	3329	0.026136	0.026240	0.026327
10	21	0.030190	0.032730	0.035036	29	4410	0.026058	0.026169	0.026262
11	28	0.034410	0.036471	0.038134	30	*5842	0.026016	0.026085	0.026143
12	*37	0.029858	0.032166	0.038226	31	7739	0.025905	0.026073	0.026316
13	49	0.030033	0.031782	0.033172	32	10252	0.025998	0.026037	0.026072
14	65	0.028867	0.031821	0.033347	33	13581	0.025949	0.025990	0.0260
15	86	0.028891	0.029774	0.030563	34	*17991	0.02591	0.02595	0.0260
16	*114	0.029003	0.029824	0.030530	35	*23833	0.02595	0.025976	0.0260
17	*151	0.028573	0.029119	0.029631	36	31572	0.0258	0.0259	0.0259
18	200	0.026830	0.028130	0.030583					

Table 2.6: Stability thresholds for the first 36 spiral mean approximants of llr^∞ on $\mathrm{Fix}(S_1)$. Shown are the values $\varepsilon_{R_{th}}$ at which the residue first reaches three thresholds, $R_{th} = 0.5$, 0.9, and 1.5. The * denotes orbits that are best approximants to ω in the sense of (C.6).

Chapter 3

Computing the Conjugacy for an Invariant Torus

3.1 Introduction

The residue method for volume-preserving maps described in Chapter 2 is only applicable to tori in reversible maps. In this chapter we describe a method to determine the existence of tori in both reversible and nonreversible systems. We will begin by introducing an efficient algorithm to compute the embedding for invariant tori of maps, adapted from the methods developed in [35, 46, 59, 12]. We will then show how the growth of the derivative of the embedding can be used to predict criticality. We specialize to the case that f is a three-dimensional volume-preserving map with one action and the torus is rotational, though much of the analysis carries over to higher-dimensional symplectic and volume-preserving mappings as well as nonrotational tori. The details of the corresponding algorithm for area-preserving mappings, used extensively in Chapters 5 and 6, can be found in [59, 48].

3.2 An Algorithm to Compute the Conjugacy for an Invariant Torus

Let $f_{\varepsilon,\lambda}$ be a family of real analytic, volume-preserving maps of the two-cylinder $M = \mathbb{T}^2 \times \mathbb{R}$ with an integrable-like limit at $\varepsilon = 0$. The parameter $\lambda \in \mathbb{R}^3$ serves several purposes that will become evident as the algorithm is presented.

Suppose there exists an analytic torus for the map f_{0,λ_0} on which the dynamics is conjugate to rigid rotation with rotation number $\omega \in \mathcal{D}_2$, that is, we suppose there exists an analytic embedding

$k : \mathbb{T}^2 \to M$ such that $k(\mathbb{T}^2) = \mathcal{C}$, and

$$f_{0,\lambda_0} \circ k = k \circ T_\omega, \text{ where } T_\omega(\theta) \equiv \theta + \omega, \tag{3.1}$$

is the rigid translation, see Fig. 3.1. KAM theory guarantees the persistence of the analytic, rotational invariant torus $\mathcal{C}$ when ε is perturbed away from zero [119, 28]. More precisely, for every $\varepsilon \ll 1$ there exists some λ_ε and embedding k such that the map $f_{\varepsilon,\lambda_\varepsilon}$ has a torus with rotation vector ω on which the dynamics is conjugate to rigid rotation with k analytic. Since k is analytic, its periodic part has a convergent Fourier series, and so it can be represented as

$$k(\theta) = \begin{pmatrix} \theta \\ 0 \end{pmatrix} + \sum_{j \in \mathbb{Z}^2} \hat{k}_j e^{2\pi i j \cdot \theta} \tag{3.2}$$

with coefficients $\hat{k}_j = \hat{k}^*_{-j} \in \mathbb{C}^3$

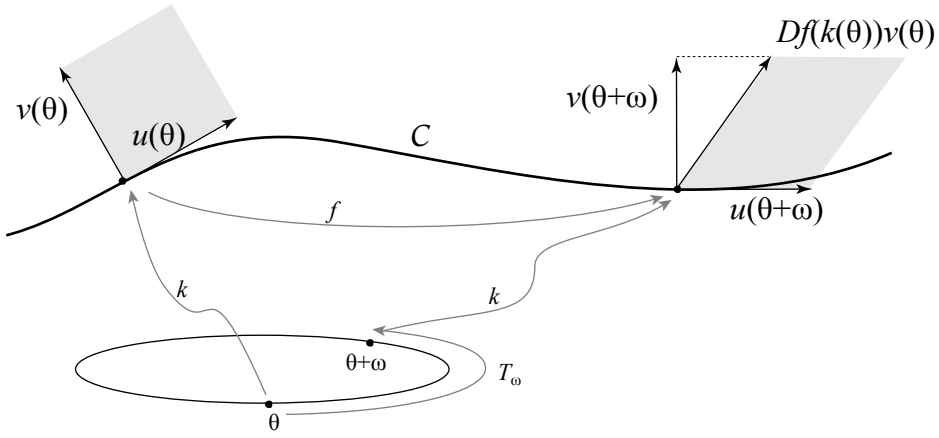

Figure 3.1: A visualization of automatic reducibility in two dimensions. The shaded regions have unit area.

Note that solutions of (3.1), if they exist, are not unique: given a solution $k(\theta)$, then $k(\theta + \chi)$ is also a solution $\forall \chi \in \mathbb{R}^2$. However when ω is incommensurate, recall (1.5), continuous conjugacies are otherwise unique, apart from this shift in the origin of θ.

Lemma 4 ([1])**.** *If $k \in C^0(\mathbb{T}^2, M)$ solves (3.1) for an incommensurate rotation vector ω, then every other continuous solution of (3.1) for the same invariant torus is of the form $k(\theta + \chi)$ for some $\chi \in \mathbb{T}^2$.*

Proof. Indeed, if $\tilde{k}$ is another continuous conjugacy, then, since $\tilde{k}(\mathbb{T}^2) = k(\mathbb{T}^2) = \mathcal{C}$, there exists a χ such that, e.g., $\tilde{k}(0) = k(\chi)$, and by (3.1), this implies $\tilde{k}(n\omega) = k(\chi + n\omega)$, $\forall n \in \mathbb{Z}$. Thus $\tilde{k}(\theta) = k(\theta + \chi)$ on a dense set in $\mathbb{T}^2$, and by continuity they agree everywhere. □

3.2.1 Automatic Reducibility

Under the assumption that there exists an invariant torus with rotation vector ω we have, in conjunction with Blass and de la Llave, developed an iterative, quasi-Newton scheme to find the conjugacy k. The algorithm starts with a guess (k, λ) such that

$$f_{\varepsilon,\lambda} \circ k - k \circ T_\omega = e, \tag{3.3}$$

and is guaranteed to converge provided that the error, e, is sufficiently small [12]. The iteration proceeds by inserting a corrected $k \to k + \Delta$ and $\lambda \to \lambda + \zeta$ into (3.3) and expanding to give

$$f_{\varepsilon,\lambda}(k(\theta)) + Df_{\varepsilon,\lambda}(k(\theta))\Delta(\theta) - k(\theta + \omega) - \Delta(\theta + \omega) + D_\lambda f_{\varepsilon,\lambda}(k(\theta))\zeta = \mathcal{O}(\Delta^2, \zeta^2)$$

where Df_λ and $D_\lambda f_\lambda$ indicate the Jacobians with respect to the state variables and parameter λ, respectively. Neglecting the second-order terms and using (3.3) gives the iterative equation

$$\Delta(\theta + \omega) - Df_{\varepsilon,\lambda}(k(\theta))\Delta(\theta) + D_\lambda f_{\varepsilon,\lambda}(k(\theta))\zeta = -e(\theta), \tag{3.4}$$

that can be viewed as determining (Δ, ζ). The resulting function, $k + \Delta$ and $\lambda + \zeta$, then is an approximate conjugacy in the sense of satisfying (3.3) with a new, presumably smaller, error e.

A direct inversion of the **cohomology** operator on the left hand side of (3.4) is numerically expensive. However, this linear operator can be partially diagonalized through a process called **automatic reducibility** in [59]. The idea is that there exists a change of variables $\Delta(\theta) = M(\theta)w(\theta)$ where $M(\theta)$ is a 3×3 orthogonal matrix, and such that for the new vector $w(\theta)$, (3.4) takes the form

$$w(\theta + \omega) - U(\theta)w(\theta) + G(\theta)\zeta = M^T(\theta + \omega)e(\theta) \equiv \tilde{e}(\theta), \tag{3.5}$$

where $U(\theta)$ is a special upper-triangular matrix and

$$G(\theta) = M^T(\theta + \omega)D_\lambda f_{\varepsilon,\lambda}(k(\theta)). \tag{3.6}$$

To find U and M, we must solve the matrix system

$$Df_{\varepsilon,\lambda}(k(\theta))M(\theta) = M(\theta+\omega)U(\theta). \tag{3.7}$$

To solve (3.7), the columns of M are chosen to be tangent and normal vector fields of the (approximate) circle $\mathcal{C}$. Note that were k an exact solution of (3.1), then differentiation implies

$$Df_{\varepsilon,\lambda}(k(\theta))Dk(\theta) = Dk(\theta+\omega), \tag{3.8}$$

which is the statement that the tangent vector fields, the columns of Dk, to $\mathcal{C}$ are invariant under $f_{\varepsilon,\lambda}$. Since the function k in (3.4) will never be an exact conjugacy, Dk will only approximately solve (3.8). Nevertheless, we may use (3.8) in the Newton iteration (3.4) incurring only error at second order, see [12]. The matrix M is now chosen to be

$$M(\theta) = \begin{pmatrix} u_1(\theta) & u_2(\theta) & v(\theta) \end{pmatrix}.$$

where u and v are unit tangent and normal vector fields

$$\begin{aligned} u_1(\theta) &= \frac{1}{\|D_{\theta_1}k(\theta)\|} D_{\theta_1}k(\theta), \\ u_2(\theta) &= \frac{1}{\|D_{\theta_2}k(\theta)\|} D_{\theta_2}k(\theta), \\ v(\theta) &= u_1 \times u_2, \end{aligned} \tag{3.9}$$

and $\times$ is the standard cross product.

With this choice, (3.7) becomes

$$\begin{aligned} Df(k(\theta))M(\theta) &= \begin{pmatrix} Df(k(\theta))u_1(\theta) & Df(k(\theta))u_2(\theta) & Df(k(\theta))v(\theta) \end{pmatrix} \\ &= \begin{pmatrix} u_1(\theta+\omega) & u_2(\theta+\omega) & v(\theta+\omega) \end{pmatrix} \begin{pmatrix} 1 & 0 & a_1(\theta) \\ 0 & 1 & a_2(\theta) \\ 0 & 0 & 1 \end{pmatrix}, \end{aligned} \tag{3.10}$$

which must be solved for the off-diagonal terms of U, the function $a(\theta)$. Approximate invariance of the tangent vector field, (3.8), implies that the first two columns of (3.10) are an identity, at least to second order. The third column gives

$$a_1(\theta)u_1(\theta+\omega) + a_2(\theta)u_2(\theta+\omega) + v(\theta+\omega) = Df_{\varepsilon,\lambda}(k(\theta))v(\theta). \tag{3.11}$$

Left-crossing by $u_1(\theta+\omega)$ (or $u_2(\theta+\omega)$), taking the inner product of the result with $-v(\theta+\omega)$ (or $v(\theta+\omega)$), and using orthogonality gives

$$\begin{aligned} a_1(\theta) &= -v(\theta+\omega)^T(u_2(\theta+\omega)\times Df_{\varepsilon,\lambda}(k(\theta))v(\theta)), \\ a_2(\theta) &= v(\theta+\omega)^T(u_1(\theta+\omega)\times Df_{\varepsilon,\lambda}(k(\theta))v(\theta)), \end{aligned} \tag{3.12}$$

which determines a. Similarly, taking the inner project of (3.11) with $u_1(\theta+\omega)\times u_2(\theta+\omega)$ and using the definition (3.9) gives the consistency condition

$$\begin{aligned} 1 &= (u_1(\theta+\omega)\times u_2(\theta+\omega))^T v(\theta+\omega) \\ &= (u_1(\theta+\omega)\times u_2(\theta+\omega))^T Df_{\varepsilon,\lambda}v(\theta) = 1. \end{aligned}$$

Simply put, this condition states that the projection onto v of the sheared image $Df_{\varepsilon,\lambda}v$ is exactly the normal vector v, since volume is preserved, see Fig. 3.1.

The three rows of (3.5) now yield partially decoupled equations for the components of the vector w,

$$w_1(\theta+\omega)-w_1(\theta) = \tilde{e}_1(\theta)+a_1(\theta)w_3(\theta)+G_1(\theta)\cdot\zeta, \tag{3.13}$$

$$w_2(\theta+\omega)-w_2(\theta) = \tilde{e}_2(\theta)+a_2(\theta)w_3(\theta)+G_2(\theta)\cdot\zeta, \tag{3.14}$$

$$w_3(\theta+\omega)-w_3(\theta) = \tilde{e}_3(\theta)+G_3(\theta)\cdot\zeta, \tag{3.15}$$

where a is defined by (3.12), $\tilde{e}$ by (3.5), and G_i is the i^{th} row of G, (3.6).

These three equations can be solved easily in Fourier space. Indeed, each is of the form of a cohomology equation

$$w\circ T_\omega - w = e,$$

which is diagonalized by Fourier transformation. Indeed, it is not hard to see that when e is analytic and ω is Diophantine (1.7), then w is analytic [94] and its Fourier coefficients are

$$\hat{w}_j = \frac{\hat{e}_j}{e^{2\pi i j\cdot\omega}-1},\ j\neq 0, \tag{3.16}$$

provided that e satisfies the solvability condition

$$\hat{e}_0 = \int_0^1 e(\theta)d\theta = 0,$$

i.e., that its average vanish. Since the average, $\hat{w}_0$, is in the kernel of the cohomology operator, it can be chosen freely.

3.2.2 Solvability

Beginning with a guess for the conjugacy (k, λ), we compute the error e from (1.8), G from (3.6), and the vector fields u_1, u_2, and v from (3.9). Now the modified error $\tilde{e}$ can be computed from (3.5) and a from (3.12). At this point the cohomology equation (3.15) can be solved for w_3 using (3.16), under the assumption that the average of $\tilde{e}_3(\theta) + G_3(\theta) \cdot \zeta$ vanishes. Even though this assumption is not generally true for an approximate conjugacy, ignoring this problem tends not to interfere with convergence of the method; indeed when $\tilde{e} \to 0$, so does the error induced by this inconsistency [12]. The average of w_3 may then be freely chosen. For simplicity, we set $w_3 = 0$.

The solvability condition for w_1 and w_2 is then

$$\begin{aligned} \hat{e}_{10} + \hat{G}_{10} \cdot \zeta &= 0 \\ \hat{e}_{20} + \hat{G}_{20} \cdot \zeta &= 0, \end{aligned} \tag{3.17}$$

which uniquely determines ζ. At this point (3.13) and (3.14) are consistent and can be solved for w_1 and w_2. The averages of w_1 and w_2 are arbitrary; indeed, since this gives the contributions $u_1(\theta)\hat{w}_{10}$ and $u_2(\theta)\hat{w}_{20}$ to k, it contributes to a shift along the torus, which corresponds to the non-uniqueness of the solution. We set $\hat{w}_{10} = \hat{w}_{20} = 0$ for simplicity. Once w is found, k and λ can be updated as $k \to k + M(\theta)w(\theta)$ and $\lambda \to \lambda + \zeta$, and this process is repeated until the error is satisfactorily low.

The importance of the parameter λ is now evident – it allows us to control averages and ensure the solvability of the cohomology equations. The elements of λ can be freely chosen, and may be dependent on the family of maps being studied. In our applications we chose the first element of λ to be a parameter in the frequency map Ω. Recall from §2.2 that the image of the frequency map $\Omega(z)$ in maps of the form (1.17) is at most a one-dimensional subspace of the two-dimensional frequency space. The map will therefore only contain tori with rotation vectors along this subspace. This restriction can be circumvented by considering a family of maps with $\delta \in \mathbb{R}$ a

parameter in the frequency map, $\Omega = \Omega(z, \delta)$ recall §2.2 . We set the second component of λ to the average of the action component of the conjugacy, $k_z(\theta)$, and rescale this component such that it has zero average, i.e.

$$k_z(\theta) = k_z(\theta) - \bar{k}_z$$

where

$$\bar{k}_z = \int_0^1 k_z(\theta) d\theta.$$

Since we can ignore the solvability condition in (3.15) the final component of λ may be set to zero,

$$\lambda = \begin{pmatrix} \delta \\ \bar{k}_z \\ 0 \end{pmatrix}.$$

3.2.3 Fast Fourier Transform

This algorithm requires the frequent transition from real to Fourier space. We define the discrete Fourier series of a function k as

$$k(\theta_n) = \sum_{j=-\frac{N}{2}}^{\frac{N}{2}-1} \hat{k}_j e^{2\pi i j \cdot \theta_n / N}$$

where the Fourier coefficients $\hat{k}_j \in \mathbb{C}^3$ are given by

$$\hat{k}_j = \frac{1}{N} \sum_{n=-\frac{N}{2}}^{\frac{N}{2}-1} k(\theta_n) e^{2\pi i j \cdot n / N}.$$

This transformation is performed efficiently using the Fast Fourier Transform (FFT) [113]. We implement the FFT using the **fftw** package [49].

3.3 Summary of the Algorithm

This algorithm is generally quite robust and invariant tori can be computed for moderate values of ε and many $\omega \in \mathcal{D}$. In some cases the algorithm fails well before ε_{cr}, even when using continuation methods to update the initial guess. This failure is often the result of aliasing in

the Fourier spectrum. Aliasing occurs whenever one computes the discrete Fourier transform of a nonlinear function of a discrete approximation to k. This error can be ameliorated by application of an anti-aliasing filter [113]. When applying this method to area-preserving maps we use a quadratic filter

$$\hat{k}_j \to \frac{\hat{k}_j}{j^2 - J^2}, \quad |j| > J$$

to scale the amplitudes of the Fourier coefficients above a threshold, J. When $\Omega(z)$ is linear we set $J = \frac{1}{2}N$ for N Fourier modes and set $J = \frac{1}{4}N$ for maps with nonlinear $\Omega(z)$ to compensate for the additional nonlinearity. This filter is applied to k at the beginning of each Newton step, prior to the computation of the error e with (1.8). A stronger anti-aliasing filter is needed when computing tori in volume-preserving maps. In this case we set all Fourier coefficients above the threshold $J = \frac{1}{3}\sqrt{N}$ to zero when solving the cohomology equations, (3.16). A coefficient is considered above this threshold if the magnitude of either mode number exceeds J.

To compute invariant tori for large ε, we use continuation from $\varepsilon = 0$, where k is trivial. In the area-preserving case we begin by incrementing the parameter by $\Delta\varepsilon = 0.01$ and using $N = 2^8$ Fourier modes. Similarly, we increment by $\Delta\varepsilon = 0.001$ and use $N = 2^7 \times 2^7$ Fourier modes for volume-preserving maps. The algorithm is iterated until the L^2 norm of the error e is less than the tolerance, set to 10^{-12} for area-preserving maps and 10^{-10} for volume-preserving ones. We then increment ε by $\Delta\varepsilon$, and use extrapolation to generate an initial guess for k and, if needed, λ, at the new ε. This is continued until the algorithm fails to converge within the specified tolerance. Upon this first failure, the step size is reduced to $\Delta\varepsilon = 0.0005$ for area-preserving maps or $\Delta\varepsilon = 0.0001$ for volume-preserving maps, and the number of Fourier modes is doubled in every dimension. At each successive failure the number of Fourier modes is again doubled; however, we found it significantly faster and more accurate (for the computation of ε_{cr}, see §3.4) to keep the step size constant. The algorithm exits when the number of Fourier modes exceeds 2^{13} or $2^9 \times 2^9$. Typically this failure occurs before the critical perturbation amplitude, ε_{cr}, where the invariant torus is first destroyed. By comparing with Greene's criterion (recall §2.1) for Chirikov's map (1.15) and the standard

volume preserving map (2.12), we observe that convergence typically fails when $\varepsilon_{cr} - \varepsilon \sim 10^{-3}$, see Fig. 3.2.

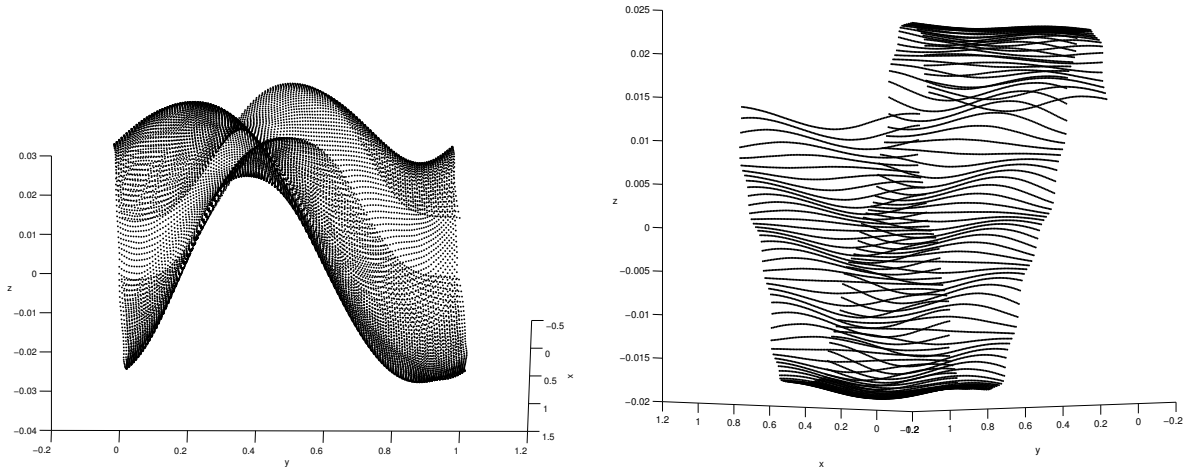

Figure 3.2: Near-critical invariant tori with rotation vector $(\sigma - 1, \sigma^2 - 1)$ (2.30) for (a) the standard volume preserving map (2.12) and (b) the ABC map (1.19) with $B = \varepsilon^2$. The torus for the standard volume-preserving map closely agrees with the periodic orbits shown in Fig. 2.12. The dynamics of the torus for the ABC map occur predominantly in the y direction. This is due to $B \ll \varepsilon$, hence the dynamics in the x direction are largely decoupled from the other dimensions.

3.4 Detecting Critical Tori

The quasi-Newton scheme discussed in §3.2 provides a method to compute an analytic invariant torus when it exists. According to KAM theory, whenever ω is Diophantine (1.7) and g and Ω are analytic, (1.2) has an analytic invariant torus when ε is small enough [34]. We will use the scheme of §3.2 to estimate the value $\varepsilon_{cr}(\omega)$ such that there is an invariant torus with rotation vector ω for all $0 \leq \varepsilon \leq \varepsilon_{cr}(\omega)$.

3.4.1 Critical Circles

When f is an area-preserving twist homeomorphism, Aubry-Mather theory implies that it has a minimizing invariant set for each ω and when ω is irrational, this set is either an invariant circle or a cantorus [87]. So, typically we expect that when ε exceeds ε_{cr} the invariant circle becomes a cantorus. Of course, it may reform for larger values of ε, and indeed the boundary of existence

of an invariant circle for multi-parameter maps is often be quite complex [18, 116, 61].

Since the conjugacy loses continuity at $\varepsilon_{cr}(\omega)$, this transition can be detected by the behavior of a Sobolev norm [20, 21]. To detect the transition, we use a related seminorm defined as the L^2-norm of the m^{th} derivative:

$$\|k\|_m^2 \equiv \|D^m k\|_{L^2}^2 = \sum_j (2\pi|j|)^{2m} |\hat{k}_j|^2, \tag{3.18}$$

where $\hat{k}$ are the Fourier coefficients of k. As $\varepsilon \to \varepsilon_{cr}$, $\|k\|_m \to \infty$, and we assume it does so asymptotically as

$$\|k\|_m \sim \frac{A}{(\varepsilon_{cr} - \varepsilon)^b} \tag{3.19}$$

To compute the three parameters in asymptotic form (3.19), we use three consecutive $(\varepsilon, \|k\|_m)$ pairs from the continuation method. One reason for using a fixed step size in ε, as described in §3.3, is that we find the estimate of the pole position to be more accurate than if a variable step size was used. We typically compute (3.18) for the angle component of k, though the action component gave similar results.

Numerical computations for the rotation number ϕ^{-2} and several examples of (1.9) indicate that (3.19) is a good fit for $m = 2$ when $\varepsilon_{cr} - \varepsilon \lesssim 10^{-2}$, see Fig. 3.3(a). More generally we find that (3.19) applies for other values of m with $b \approx m - 1$.

The choice of m significantly affects the error in the approximation of ε_{cr}. In Fig. 3.3(b) we compare the estimates of ε_{cr} from (3.19) for Chirikov's map with those obtained numerically from Greene's criterion (details of the implementation can be found in App. D). For the invariant circles with rotation numbers ϕ and $\sqrt{2}$, and orbits of periods up to 30000, Greene's method gives

$$\begin{aligned} \varepsilon_{cr}(\phi) &= 0.9716353(1) \\ \varepsilon_{cr}(\sqrt{2}) &= 0.957447(6), \end{aligned} \tag{3.20}$$

where the error (the number in parentheses is the uncertainty in the last digit) is estimated from the extrapolation.[1] We observe that the smallest numerical error for the seminorm fit occurs with the

[1] Using quadruple precision, MacKay computed $\varepsilon_{cr}(\phi) = 0.9716354063(2)$ [78, §4.4].

choice $m = 2$. With the maximal number of Fourier modes fixed to 2^{13}, mainly for computational speed, we are typically able to estimate ε_{cr} with an error less than 10^{-4}.

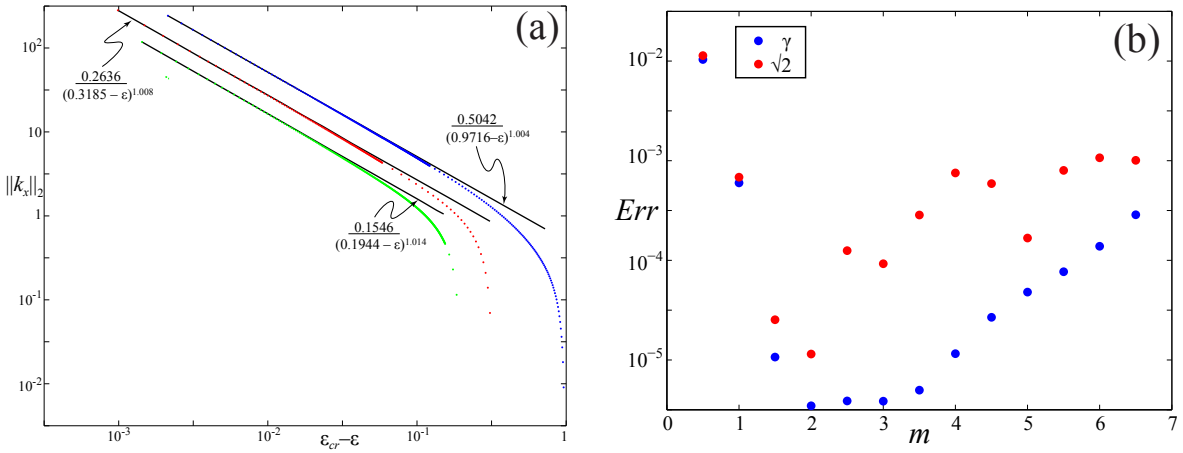

Figure 3.3: (a) Blow-up of the seminorm $\|k_x\|_2$ for the $\omega = \phi^{-2}$ invariant circle for three cases of (1.9). The upper (blue) curve corresponds to Chirikov's standard map. The lower two curves have the force (4.3) with $\psi = \pi/4$. The middle (red) curve is for the frequency map (1.11) and the bottom (green) is for (1.16) with $\delta = 0.3$. In each case the horizontal axis is logarithmic based on the best estimate of ε_{cr} from (3.19). (b) Error in the pole location for fits to (3.19) for seminorms with varying m for Chirikov's map for two rotation numbers, compared to ε_{cr} from Greene's criterion. For both rotation numbers, the smallest error occurs with $m = 2$.

When the invariant circle is not symmetric, Greene's residue criterion is harder to implement, since a periodic orbit finder would require a two-dimensional search. Nevertheless, we select $m = 2$ for the computations in the rest of this dissertation. We estimate the error in the calculation of ε_{cr} as the difference between the last two, three-step approximations obtained with the step size $\Delta\varepsilon = 0.0005$.

A more comprehensive evaluation of the accuracy of the seminorm method will be performed in Chapter 4.

3.4.2 Critical Tori

There is no generalized version of Aubry-Mather theory applicable to volume-preserving homeomorphisms. The topology of the invariant sets for $\varepsilon > \varepsilon_{cr}$ is therefore unknown. However, this set no longer forms a boundary to transport, so we can conclude that some gaps form in the

surface. The formation of these gaps, and the corresponding spike in the derivatives, provides a means to predict criticality.

Although the seminorm method described in §3.4.1 can be applied to volume-preserving systems, it is prone to larger errors, likely a result of the increased effects of aliasing on the Fourier spectrum. We therefore measure the growth of the derivatives of k by studying square of the singular values of Dk, or, equivalently, $||Dk||_2^2$, which we will denote $\mathcal{S}$. Recall that the singular values of Dk are defined as the square roots of the eigenvalues of

$$Dk^T Dk = \begin{pmatrix} ||u_1||_2^2 & u_1 \cdot u_2 \\ u_1 \cdot u_2 & ||u_2||_2^2 \end{pmatrix}, \tag{3.21}$$

Note that we do not normalize the tangent vectors, as described by (3.9), prior to computing these singular values. As $\varepsilon \to \varepsilon_{cr}$ we expect $\mathcal{S} \to \infty$ asymptotically as (3.19). The pole position is estimated by using three successive $(\varepsilon, \mathcal{S})$ pairs from the continuation scheme.

One advantage of this technique is that we do not need to select any parameters to minimize error. Indeed, we are able to predict the pole position with reasonable accuracy for a variety of volume-preserving maps and Diophantine rotation vectors, see Fig. 3.4. The parameter b in (3.19) varies significantly with both the map and rotation vector of the torus, in contrast to the behavior seen when applying the seminorm method for circles, recall Fig. 3.3

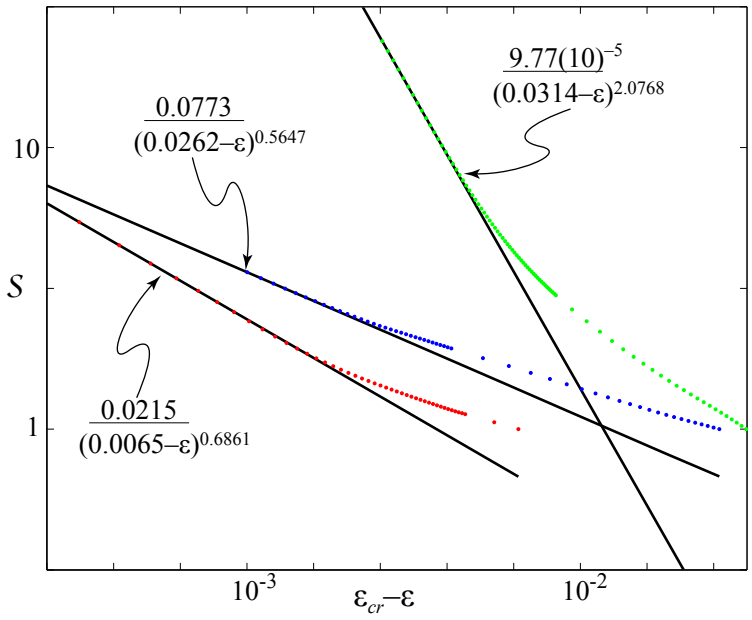

Figure 3.4: Blow-up of the largest singular value for the $\omega = ll\bar{r}$ invariant torus for three volume-preserving maps. The middle (blue) curve corresponds to the standard volume-preseving map. The upper and lower curves are for the ABC map (1.19). The bottom (red) curve is for $B = 2\varepsilon$ and the top (green) is for $B = \varepsilon^2$. In each case the horizontal axis is logarithmic based on the best estimate of ε_{cr} from (3.19).

Chapter 4

Conjugacies of Near-Critical Tori

In this chapter we examine the conjugacy (3.1) for tori with golden and spiral mean rotation vectors for a variety of area and volume-preserving maps. Our goal is to provide evidence for two conjectures.

Conjecture 1. *When a rotational invariant circle of (1.9) is destroyed it becomes a cantorus.*

Recall that this is known to be true whenever (1.9) is a nondegenerate twist map, i.e. when (1.14) holds. However, Aubry-Mather does not extend to nontwist maps such as (1.9) with (1.16). In §4.1 we will study the formation of gaps in invariant circles of (1.9) with a variety of frequency maps and multi-harmonic forces, giving evidence for Conj. 1.

Conjecture 2. *A rotational invariant torus of a three-dimensional volume-preserving map with one action and two angles is destroyed by the formation of a single or multiple "holes".*

The formation of holes in the rotational circles of area-preserving maps is described by AI theory, recall §1.1. This theory has not yet been generalized to volume-preserving systems, although horseshoes of orbits have been found by Malkin and Li [70, 60]. In §4.2 we will examine the near-critical tori of the standard volume-preserving map (2.12) and the ABC Map (1.19), providing evidence for Conj. 2

4.1 Area-Preserving Maps

We begin by computing the embedding of the oft-studied, golden mean invariant circle for Chirikov's map, i.e., for

$$g = g_1 = \frac{\varepsilon}{2\pi}\sin(2\pi x) \tag{4.1}$$

and $\Omega = \Omega_1$, (1.11). The algorithm of §3.2 converges up to $\varepsilon = 0.9695$, which from (3.20) is $\varepsilon_{cr}(\phi) - 0.0021$. The resulting embedding at this parameter value, as shown in Fig. 4.1, has error $e(\theta)$, (1.8), with L_2-norm of $(10)^{-12}$ and L_∞-norm of $1.7(10)^{-11}$.

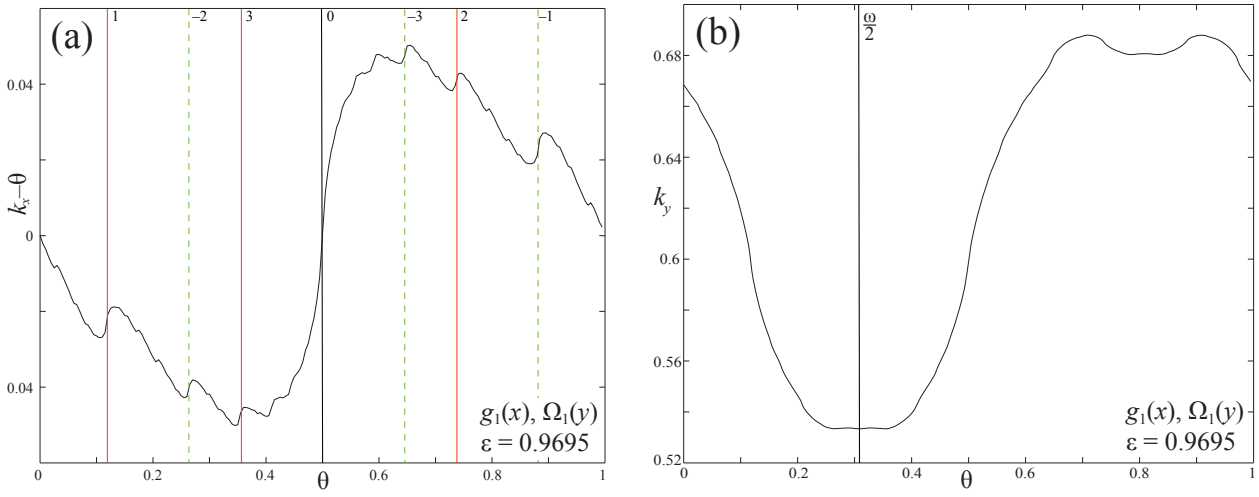

Figure 4.1: Components of the conjugacy for the $\omega = \phi^{-1}$ invariant circle with of Chirikov's standard map from a computation with 2^{13} Fourier modes. (a) The function $k_x(\theta) - \theta$ and the first three forward and backward images of $\theta = \frac{1}{2}$, indicated by the solid (red) and dotted (green) lines, respectively. (b) The action component $k_y(\theta)$ is even about $\omega/2$.

Since Chirikov's map has twist, Aubry and Mather theory implies that each invariant circle becomes a cantorus upon destruction. Moreover, these sets are ordered in the sense that $\theta \mapsto k_x(\theta)$ is a monotone circle map. The implication is that upon destruction of the circle, the extension of the conjugacy to the Cantor set is a devil's staircase; consequently, $k_x(\theta) - \theta$ must develop positive jump discontinuities at a dense set of θ values corresponding to the location of the gaps in the cantorus. Although the Fourier method does not converge for the critical or super-critical cases, the beginning of this metamorphosis can be seen as $\varepsilon \to \varepsilon_{cr}$. For example, localized regions with

large slope along the orbit $\theta_t = \frac{1}{2} + t\omega$ can be seen in Fig. 4.1(a). Indeed the largest, incipient discontinuity occurs at $\theta = \frac{1}{2}$, which, since the computations give $k_x(\frac{1}{2}) \approx \frac{1}{2}$, also corresponds to $x \approx \frac{1}{2}$.

The locations of the gaps can be explained by recalling that an invariant circle corresponds to a minimizing state of the Frenkel-Kontorova energy (1.12). The potential for this map, $V(x) = -\frac{1}{4\pi^2}\cos(2\pi x)$, has a single maximum at $x = \frac{1}{2}$; thus, the AI theory implies that the largest gap should form around this maximum, and its images form a bi-infinite family (one "hole") that corresponds to the gaps in the cantorus. The first few forward and backward iterates in this family are indicated by the vertical lines in Fig. 4.1(a). Continuing this process to larger iterates appears to account for all the local peaks in the derivative of k_x; thus it appears that this cantorus has one hole [81], a fact that can be proven near the AI limit [10].

The standard map has two independent families of reversors, see App. E: it is **doubly-reversible**. The first reversor arises from the oddness of g_1 and the second from the oddness of Ω_1. As is shown in Cor. 9 in the appendix, the first reversor implies that the function $k_x(\theta)$ is odd about some point φ; using (F.3), we computed $\varphi = -\hat{k}_{x0} \approx -8.130(10)^{-5}$. Since φ is so small, the graph in Fig. 4.1(a) looks like it is odd about 0. Corollary 9 also implies that the action $k_y(\theta)$ is even about $\varphi + \frac{1}{2}\omega$, as is visually apparent in Fig. 4.1b. More precisely, we found that the identities (F.3) are satisfied up to an error with L_∞-norm of $9.9(10)^{-13}$, which is comparable to the accuracy of the computation of k itself.

A second, doubly-reversible version of (1.9) is the generalized, two-harmonic twist map with the force

$$g_2(x;\psi) = \tfrac{1}{2\pi}\left(\sin(\psi)\sin(2\pi x) + \cos(\psi)\sin(4\pi x)\right), \tag{4.2}$$

keeping the frequency map, Ω_1. The breakup of the golden mean circle for this map was studied first by Greene et al [55], and later the formation of cantori and turnstiles were studied in [61, 62, 9, 10, 73].[1] The two-harmonic map reduces to Chirikov's map when $\psi = \frac{\pi}{2}$; the two maps are also equivalent when $\psi = 0$ or π under the rescaling transformation $(x, y) \mapsto 2(x, y)$, so that the

[1] In these papers the parameterization $k_1 = \varepsilon\sin(\psi)$ and $k_2 = -2\varepsilon\cos(\psi)$ was used for εg_2.

parameter and rotation number are effectively doubled. Finally, since $g(x+\frac{1}{2},-\psi)=g(x,\psi)$, it is sufficient to study the parameter range $\psi\in[0,\pi]$.

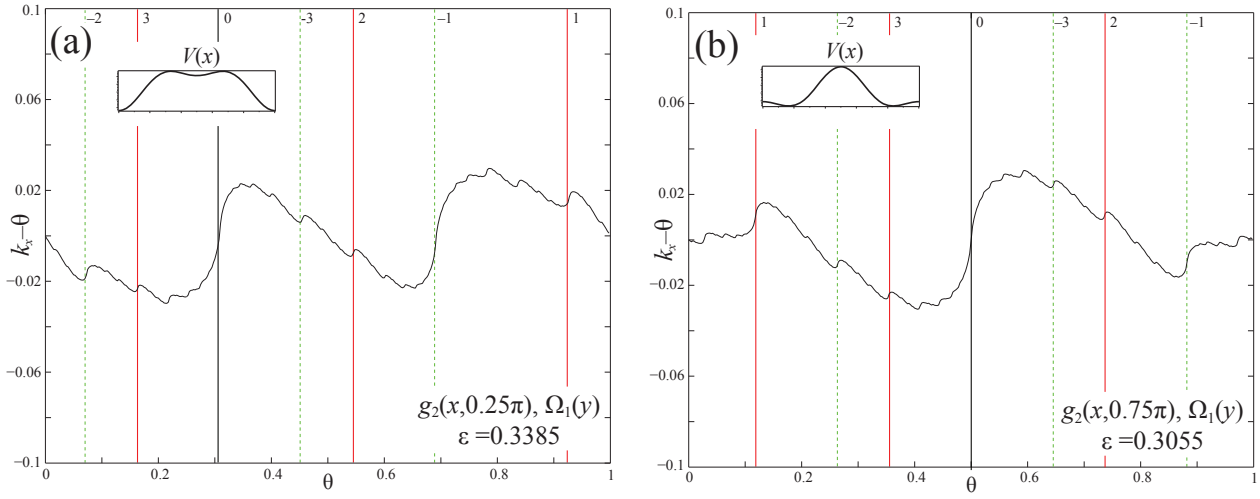

Figure 4.2: Plots of $k_x(\theta)-\theta$ for near-critical invariant circles for (1.9) with (1.11) and (4.2) and $\omega=\phi^{-1}$. Also shown are the first three forward (red, solid) and backward (green, dashed) images of the largest gap. Insets show the shape of the potential $V(x)$ for the two values of ψ.

Two examples of near-critical invariant circles for the two-harmonic twist map are shown in Fig. 4.2. Since this map has the same reversors as Chirikov's map, k_x is still odd (since $k_x(0)\approx 0$, essentially about $\theta=0$). When ψ is small, as in Fig. 4.2(a), it appears that there is a symmetric pair of two equally large incipient gaps (near $\theta_1=0.3090$ and 0.6910), while for larger larger ψ, Fig. 4.2(b), their is a single, largest gap near $\theta=0.5$. In both cases, it appears that there is a single orbit, $\theta_i+t\omega$, of gaps: for example, two largest peaks in Fig. 4.2(a) are separated by one iterate. Thus the resulting cantori will have one "hole."

The difference between the two cases is correlated to the structure of the potential $V(x)=\int g_2 dx$, shown in the insets in Fig. 4.2. For the two harmonic case, V has critical points at $x=0$, $\frac{1}{2}$ and any solutions of $\tan\psi=-2\cos(2\pi x)$. When $0<\psi<\arctan 2\approx 0.35\pi$, V has two wells, the deepest at $x=0$, separated by maxima of equal height; this is the case for Fig. 4.2(a). The maxima collide at $\tan\psi=2$ annihilating the well at $x=\frac{1}{2}$. For $|\tan\psi|\geq 2$, V has single well. Finally, when $0.65\pi\approx\pi-\arctan 2<\psi<\pi$ the potential has two equally deep wells separated by

differing maxima, the largest at $x = \frac{1}{2}$, as shown in Fig. 4.2(b). The AI limit, $\varepsilon \to \infty$, for a double well potential has infinitely many cantori, selected by the fraction of points that lie in each well [62, 10]. For these cases, there are cantori with two families of gaps, though the second "hole" is formed beyond the initial breakup of the invariant circle. Note that when $\tan\psi = \pm 2$, the potential has degenerate critical points and persistence of AI states with these points occupied cannot be guaranteed.

When the maxima of the potential collide at $\tan\psi = 2$, we expected that the symmetric pair of largest gaps shown in Fig. 4.2(a) would also merge. However, as shown in Fig. 4.3, this merger does not occur until $\psi \approx 0.46\pi$, well after the collision. Note that as the largest gaps coalesce, they still appear to lie on a single orbit, though the number of iterates between them changes with ψ. For example, for $\psi = 0.44\pi$, in Fig. 4.3(a), the largest gaps are two iterates apart, but for $\psi = 0.46\pi$, in Fig. 4.3(c), they are five iterates apart.

The set of critical parameters (ε_{cr}, ψ) for the golden mean circle of this map, computed using the seminorm method is shown in Fig. 4.4(a). For $\psi = \frac{\pi}{2}$, $\varepsilon_{cr} = 0.971635$ since $g_2(x, \frac{\pi}{2}) = g_1(x)$. In addition $\varepsilon_{cr} = 0.40236$ when $\psi = 0$ or π—this is half the critical parameter for the $\omega = \frac{\phi}{2}$ circle of Chirikov's map [55]. When $\psi \in [0, \frac{\pi}{2}]$, the critical set exhibits a Cantor set of cusps as was first observed using Greene's criterion in [61]. The cusps are related to a complex set of symmetry breaking bifurcations of periodic orbits that limit onto the invariant circle [62].

To begin an exploration of the breakup of circles in maps with less symmetry, consider a two-harmonic force similar to (4.2), but with a phase shift so that it is no longer odd:

$$g_3(x;\psi) = \tfrac{1}{2\pi}(\sin(\psi)\sin(2\pi x) + \cos(\psi)\cos(4\pi x)). \tag{4.3}$$

With the odd frequency map Ω_1, the map still has one reversor S_2, (E.2), which conjugates the circles with rotation numbers $\pm\omega$. As before, $g_3(x + \frac{1}{2}, -\psi) = g_3(x, \psi)$, so the parameter ψ can be restricted to the range $[0, \pi]$. Moreover, since $g_3(-x, \pi - \psi) = -g_3(x, \psi)$, the transformation $(x, y, \psi) \to (-x, -y, \pi - \psi)$ leaves the dynamics invariant, so we need consider only $\psi \in [0, \frac{\pi}{2}]$.

Two examples of near-critical invariant circles for this map are shown in Fig. 4.5. Since the

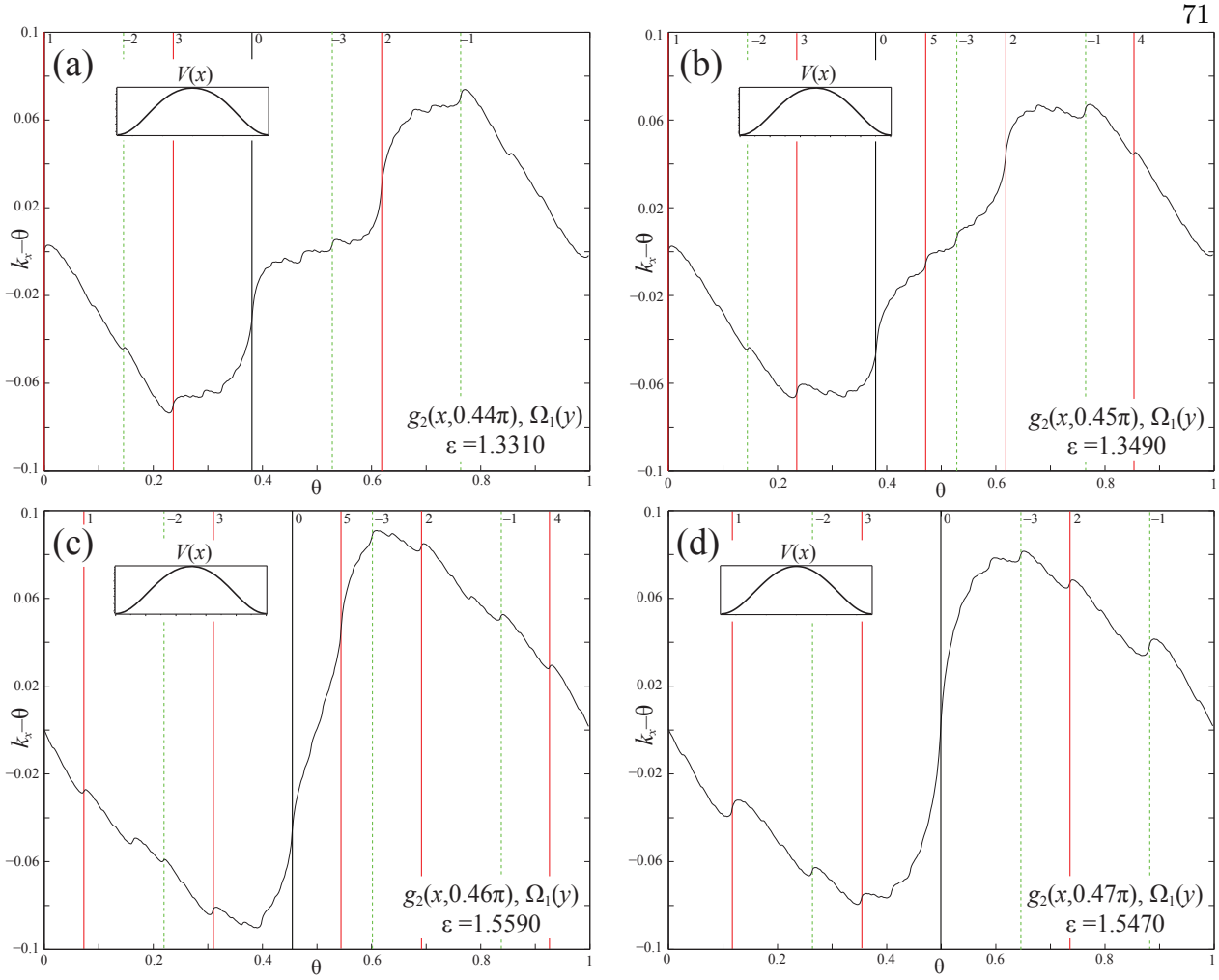

Figure 4.3: Near-critical conjugacies, $k_x(\theta) - \theta$, for the ϕ^{-1} circle of (1.9) with g_2 and Ω_1, and the values of ψ and ε indicated. Insets show the potential $V(x)$ for these parameter values. Vertical lines show forward (solid) and backward (dashed) iterates of the largest gap.

force (4.3) is not odd, the map (1.9) no longer has the reversor (E.1), and the resulting invariant circles will not be invariant under S_1. Indeed, the conjugacies shown in the figure no longer show this symmetry and the relations (F.3) no longer hold.

The potential for g_3 has two wells when $\psi \in [0, \frac{\pi}{4})$ and a single well for $\psi \in [\frac{\pi}{4}, \pi]$. In both panes of the figure, the potential has a single well and the largest gap is formed near the maximum of V. For $\psi < \frac{\pi}{4}$, the second largest gap is formed near the smaller maximum of V. This gap can still be seen for the degenerate case of Fig. 4.5(a), near $\theta = 0.2$, and the corresponding $x = k_x(\theta)$ is near the degenerate critical point of V at $x = 0.25$. This gap is the image of the largest gap and is

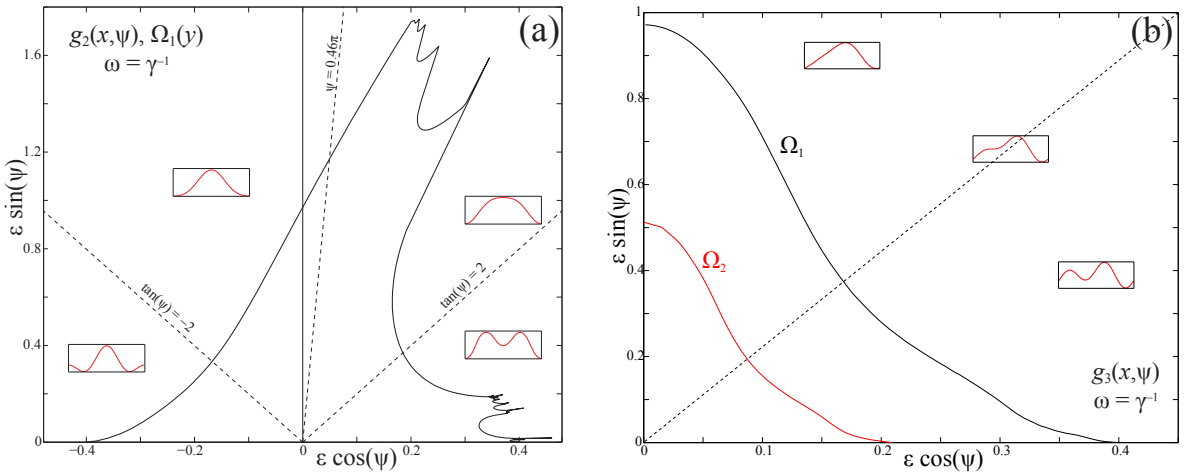

Figure 4.4: Critical parameter set for the golden mean circle of (1.9) for the frequency maps and two-harmonic forces shown, computed using the seminorm. The axes are the amplitudes of the two Fourier modes of εg. The dashed lines correspond to degenerate AI limits and for (a) to $\psi = 0.46\pi$ where the two symmetric gaps coalesce in Fig. 4.3. Insets show representative $V(x)$.

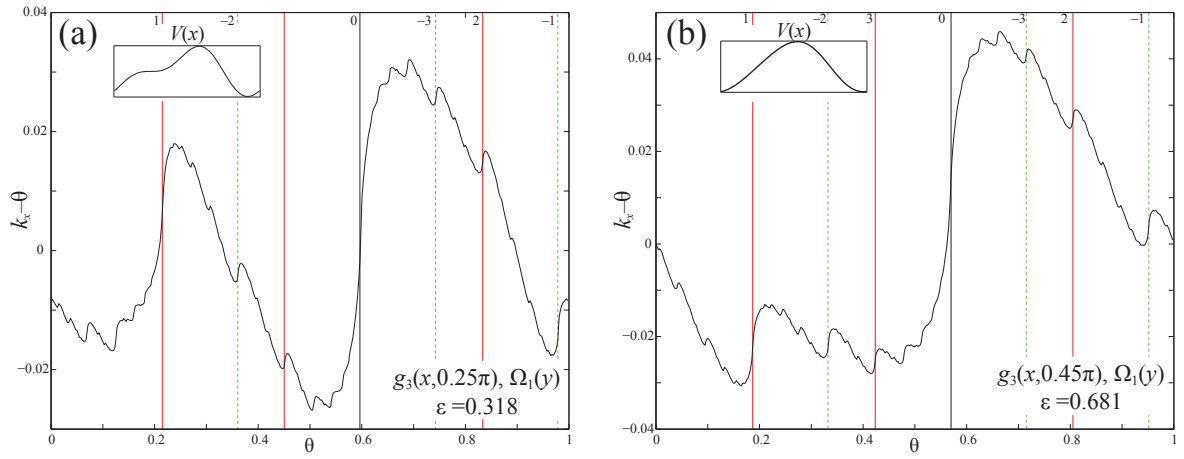

Figure 4.5: Angle component of the conjugacy for a near-critical circle of the generalized standard map with g_3 and Ω_1, for $\omega = \phi^{-1}$ and two values of ψ. These embeddings do not exhibit the symmetry seen for the reversible case, but do display an orbit of incipient gaps.

much larger any other gaps. This secondary gap is still present in Fig. 4.5(b), but is significantly smaller, giving some evidence for the influence of the smaller maximum on the formation of gaps.

The critical set for the golden mean circle of this map is shown in Fig. 4.4(b) (the black curve) for the range $\psi \in [0, \frac{\pi}{2}]$; this set is symmetric under reflections about the horizontal and vertical parameter axes. Just as for Fig. 4.4(a), the points at $\psi = 0$ and $\psi = \frac{\pi}{2}$ correspond to

Chirikov's map. However, this critical curve no longer has a Cantor set of cusps—indeed, it seems to be smooth apart from a cusp at $\psi = 0$ (and also $\psi = \pi$), corresponding to the doubled Chirikov map.

We now consider several maps with the frequency map Ω_2, (1.16), for which twist reverses at $y = 0$. For this case, there are typically two circles for each rotation number in the range of $\Omega_2(y, \delta)$. When $\omega \gg -\delta$ one circle is contained in the positive twist region, $y > 0$, and one in the negative twist region, $y < 0$. The most interesting circles, however, cross $y = 0$ so that the twist condition is locally violated. The breakup of such invariant circles for the standard nontwist map (with g_1), has been much studied [2, 51, 118], so we do not study this map here.

Instead we consider a nontwist map with force g_3. It would seem that destroying the oddness of both g and Ω, would eliminate both reversors of (1.9). However, since g_3 is even about $\frac{1}{4}$, $g_3(\frac{1}{4} + x, \psi) = g(\frac{1}{4} - x, \psi)$, and Ω_2 is even about $y = 0$, this map has the reversor S_3, (E.3). This reversor conjugates the positive and negative twist circles; in particular they have the same ε_{cr}. Moreover, the transformation $(x, y, \psi) \to (x, -y, \pi - \psi)$ leaves the dynamics invariant, and combining this with the reversor allows us to restrict $\psi \in [0, \frac{\pi}{2}]$.

Invariant circles of this map with $\omega \gg -\delta$ are very similar to those of a twist map, see for example the positive twist circle in Fig. 4.6. The conjugacy is very close to that for the twist case, $\Omega = \Omega_1$, shown in Fig. 4.5. Indeed, since $|k_y(\theta)| \approx 0.9581$ with a variation of ± 0.023, the twist is nearly linear over the range of oscillation of y. Moreover, since $D\Omega_2(y, \delta) = 2y \approx 1.9161$, the twist is almost a factor of two larger than that for Ω_1—this accounts for the fact that ε_{cr} has been decreased by factor very close to two from the Ω_1 case.

Circles that experience a stronger variation in twist, display significantly different behavior than those of the twist case. This is especially true of those circles that cross the $y = 0$ axis, where the twist vanishes. Figure 4.7 compares circles for Ω_1 and Ω_2 with the same noble rotation number $\omega \approx -0.2793$. Both still have one orbit of gaps; however, the dominant gap is no longer associated with the largest maximum of V. Thus, though it appears that the invariant circle will become a "one hole" cantorus upon destruction, traditional anti-integrable theory may not provide insight

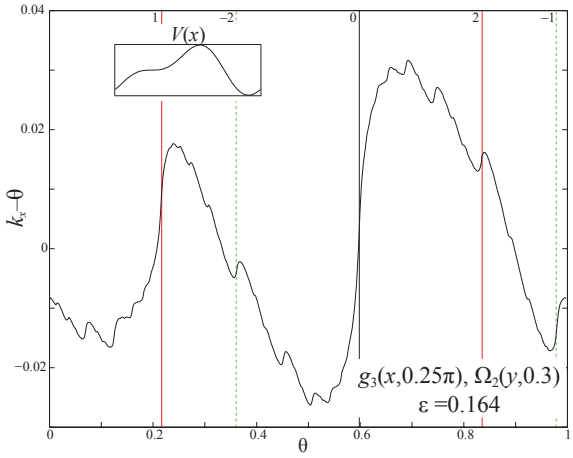

Figure 4.6: Angle component of the conjugacy for near-critical circle of the generalized standard map with g_3 and Ω_2, for $\omega = \phi^{-1}$ and $y > 0$.

its formation. Note also that ε_{cr} for the nontwist case is 4.02 times larger than that for the twist map, no doubt related to the fact that $\langle D\Omega_2(y, 0.3)\rangle = 2\hat{k}_{y0} = 0.2083$ is 4.8 times smaller than $D\Omega_1 = 1$.

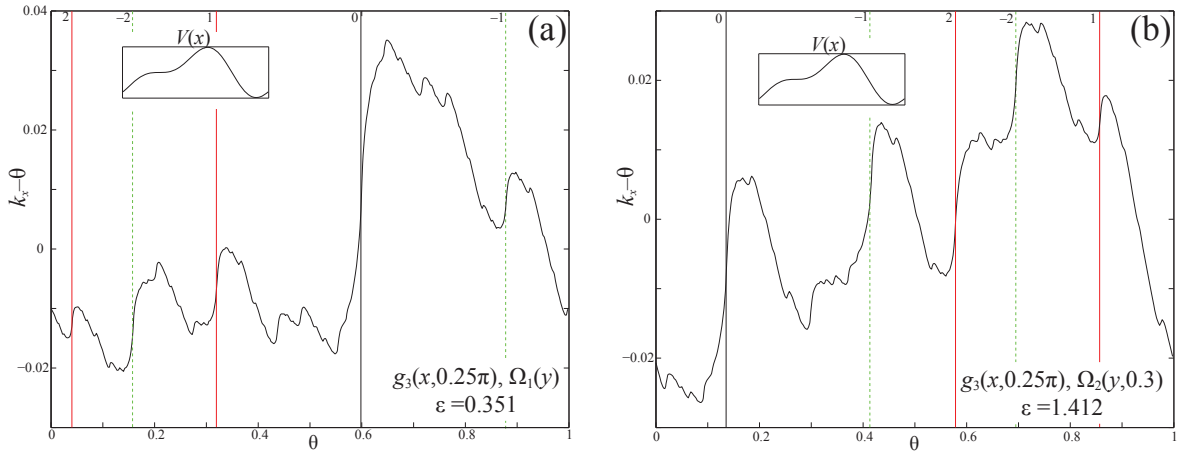

Figure 4.7: The conjugacy k_x for a near-critical invariant circle for $g_3(x, \frac{\pi}{4})$ with $\omega = -(12 + 19\phi)/(43 + 68\phi)$ and Ω_1 (a) and Ω_2 (b). The invariant circle for the nontwist case (b), crosses the y-axis.

Finally, we explored a map that we conjecture has no reversors. For this map we use the frequency map introduced by Rannou [102], that is neither even nor odd,

$$\Omega_3(z) = -z + \frac{1}{2\pi}(\cos(2\pi z) - 1). \tag{4.4}$$

that is neither even nor odd. This frequency map, like Ω_2, does not satisfy the twist condition. Rannou used this in conjunction with an even force that that has a nonzero integral. Thus Rannou's map has nonzero net flux and no rotational invariant circles when $\varepsilon \neq 0$. To permit invariant circles, but to eliminate additional symmetry, we use instead a force that is neither even nor odd, has a zero average, and a full Fourier spectrum:

$$g_4(x;\psi) = \frac{1}{2\pi}\sin\left(2\pi x + \psi\cos(4\pi x)\right). \tag{4.5}$$

The generalized standard map with Ω_3 and g_4 is, to the best of our knowledge, completely nonreversible and asymmetric.

An example of an near-critical, golden mean invariant circle for this map is shown in Fig. 4.8. This circle also appears to have one hole; the principal gap forms near $\theta = 0.44$, corresponding to the (single) maximum of the potential, as shown in the inset to the figure.

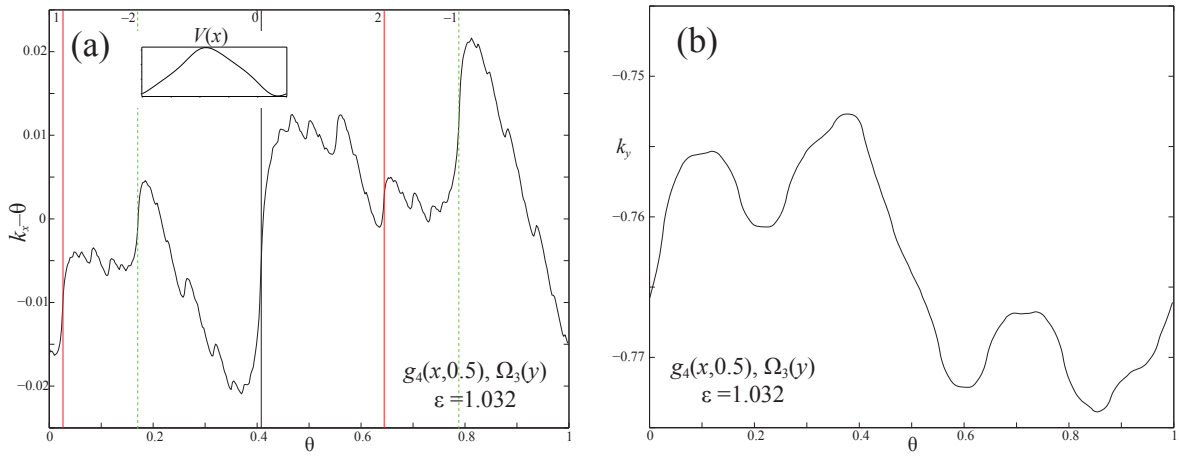

Figure 4.8: Angle (a) and action (b) components of the conjugacy for a near-critical invariant circle with $\omega = \phi^{-1}$ of a generalized standard map with no known symmetries.

4.2 Volume-Preserving Maps

The breakup of tori in volume-preserving maps is far less understood than the breakup of circles. Aubry-Mather theory has not been generalized to nonsymplectic volume-preserving systems, nor can we apply AI theory to general three-dimensional maps, except for some 3^{rd}

difference equations [60]. In this section we will explore the breakup of tori in the standard volume-preserving (2.12) and ABC (1.19) maps by examining the singular values of Dk, (3.21). Recall that these singular values measure the magnitude of the derivatives of k, or, equivalently, the amount of stretching that occurs. Localized growth of the singular value therefore implies the local deformation of the torus.

We will begin by examining the breakup of tori in the standard volume-preserving map (2.12). Since this map is reversible, the Fourier series of the conjugacy satisfies the relations (F.4). Indeed, for the $ll\overline{r}$ torus we found that $\varphi = (1.236(10)^{-6}, -1.598(10)^{-6})$ and the identities (F.4) held up to an L_∞ error of $2.84(10)^{-10}$, $3.03(10)^{-10}$, and $2.22(10)^{-11}$ for the x_1, x_2, and z dimensions, respectively, comparable to the overall accuracy of the computation of k.

The breakup of tori in the standard volume preserving map follows the same general pattern as the breakup of circles in the generalized standard map. A main gap, or pair of gaps, corresponding to a spike in the largest singular value of Dk, forms at some point in the torus. Each gap is then iterated forward and backward in time, generating a "hole." However, both the location of these gaps, and their geometry, vary significantly.

Some tori, such as those shown in Fig. 4.9, develop circular gaps. These gaps, which we refer to as **dimples**, always form in symmetric pairs about $(\theta_1, \theta_2) = (\frac{1}{2}, \frac{1}{2})$. In some cases these gaps lead to a single hole, such as in Fig. 4.9(a), where the main dimples are 6 iterates apart. In other instances, such as Fig. 4.9(b), two distinct holes form within the torus. Recall that this two-hole behavior was never observed in the near-critical conjugacies for the generalized standard map. The dimples tend to form in tori with relatively small singular values, or, equivalently, large b in (3.19).

The gaps in the tori more commonly develop as **streaks**. Initially, a single large streak forms about a spike in the singular value, as shown in Fig. 4.10(a). This streak is commonly aligned with the rotation vector ω, however other alignments have been observed. As the torus becomes critical this main streak breaks apart into several smaller ones which are joined by additional streaks that form throughout the conjugacy, each centered about an iterate of the primary peak in the singular value, see Fig. 4.10(b). This behavior is generally seen in tori with relatively large singular values

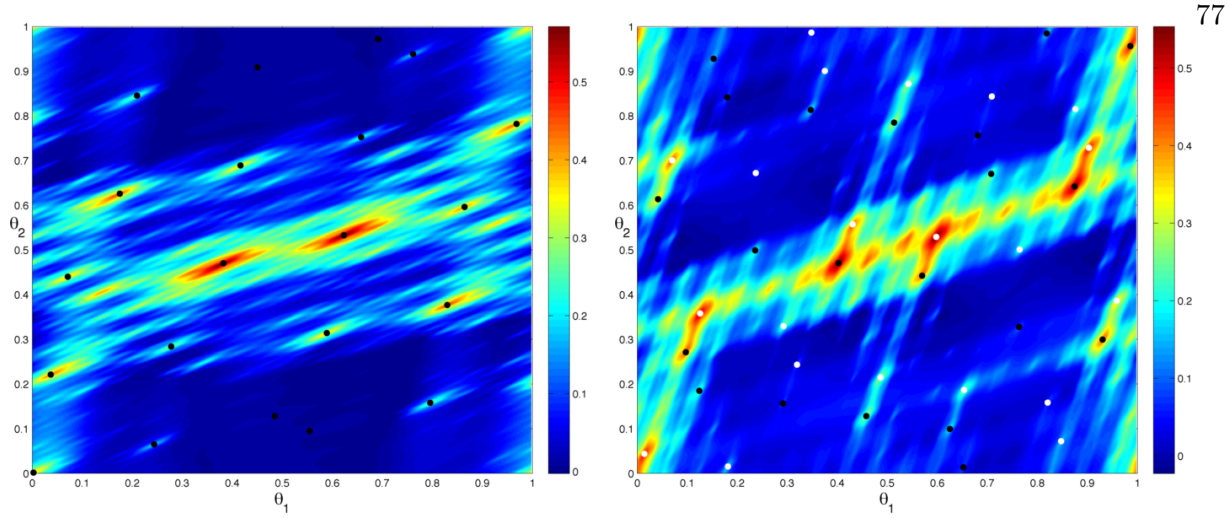

Figure 4.9: Critical conjugacies for tori in the standard volume-preserving map (2.12) that form dimples. The color indicates the $\log_{10}$ of the singular value. (a) The $llrrl\bar{r}$ torus at $\varepsilon = 0.0168$. The largest singular value occurs at $\theta = (.6230, .5332)$. The black dots indicate the forward and backward iterates of this peak. (b) The $llrrrl\bar{r}$ torus at $\varepsilon = 0.0310$. Two main peaks develop at $\theta = (.5977, .5293)$ and $\theta = 1 - (.5977, .5293)$. Each peak generates a "hole" in the torus since the white and black points are on different orbits.

for moderate ε.

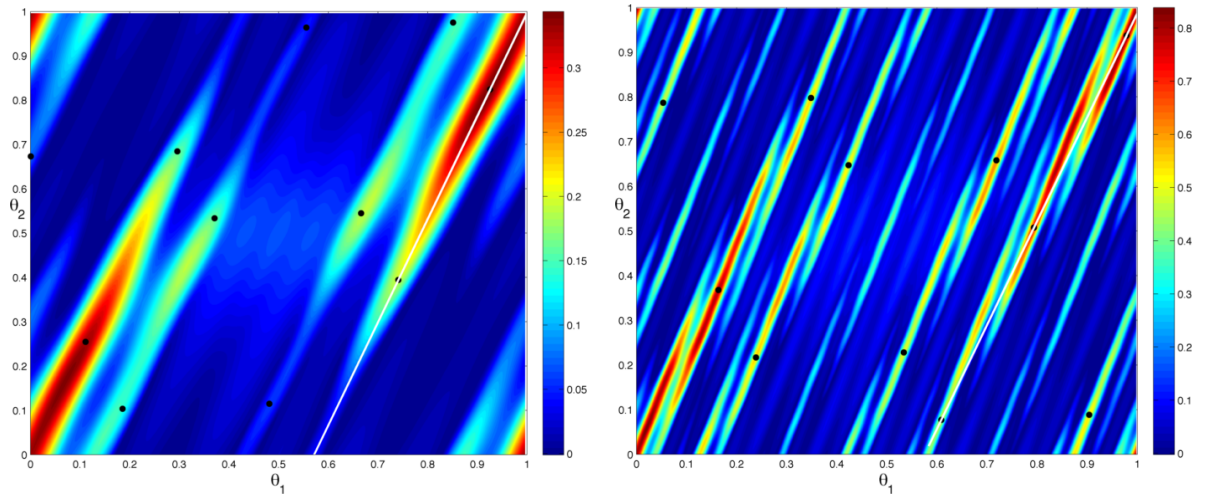

Figure 4.10: Sub-critical and critical conjugacies for the $llrl\bar{r}$ torus in the standard volume-preserving map (2.12). The color indicates the logarithm of the singular value. (a) The sub-critical conjugacy at $\varepsilon = .0099$ exhibits a single large streak aligned with the rotation vector ω, plotted in white. (b) The critical conjugacy at $\varepsilon = 0.0118$. The main streak has broken up and several other smaller streaks have formed. Each smaller streak is centered about an iterate of the peak of the singular value, indicated by the black dots.

The breakup of tori in the nonreversible ABC map (1.19) was also studied. In order to

compute the conjugacy the parameters must be chosen such that the map has an integrable limit. We set $\varepsilon = 2\pi C$, $B = \varepsilon h(\varepsilon)$ for some function $h(\varepsilon)$, and made A an essential parameter in the frequency map, similar to the parameter δ in (2.12), such that Ω is the diffeomorphism

$$\Omega(A, z) = (\frac{A}{2\pi}\sin(2\pi z), \frac{A}{2\pi}\cos(2\pi z)).$$

These parameters will be used throughout the remainder of this dissertation. Note that the parameters B and C describe the amplitude of the perturbation to the y and x dimensions, respectively.

To understand the breakup of tori in this map we must first recognize that the dynamics are significantly altered whenever $B \equiv 0$. In this case the y and z dimensions are completely decoupled from the angle x, hence the dynamics of the map are essentially two-dimensional with a quasi-periodically forced third dimension. The two-dimensional map defined by the angle y and action z is area-preserving and its inverse

$$f_{yz}^{-1}(y, z) = (y - \frac{A}{2\pi}\cos(2\pi(z - \frac{C}{2\pi}\sin(2\pi y))), z - \frac{C}{2\pi}\sin(2\pi y)) \tag{4.6}$$

can be analyzed with AI theory for fixed A. In this case (4.6) has the potential $V_{yz}(y) = \frac{1}{4\pi^2}\cos(2\pi y)$ with a maximum at $y = 0$. Interestingly, the breakup of tori in the $B = 0$ ABC appears to be governed by the potential of (4.6), even though A changes with ε. Indeed, these tori form a thick streak along the line $y = 0$, with only minor variations in the x direction, see Fig. 4.11. Similarly, when $C \equiv 0$ the main streak forms along the line $x = \frac{1}{4}$, corresponding to the peak of the potential for the area-preserving map defined by the angle x and action z, $V_{xz}(x) = \frac{1}{4\pi^2}\sin(2\pi x)$.

The breakup of the ABC map follows a similar pattern when B is either asymptotically larger or smaller than C. Consider, for example, the case with $B = \varepsilon^{3/4} \gg C$. When ε is small, a streak forms along the line $x = \frac{1}{4}$, see Fig. 4.12(a), similar to the $C = 0$ torus. As ε grows and the perturbation in the y direction increases this gap is deformed, and additional gaps form at the iterates of the main peak, shown in Fig. 4.12(b).

When $B = \mathcal{O}(C)$ there is no consistent pattern to the breakup of the tori. In some cases we see gaps form at $x = \frac{1}{4}$ or $y = 0$ and deform, similar to when $B \neq \mathcal{O}(C)$. Dimples often arise at

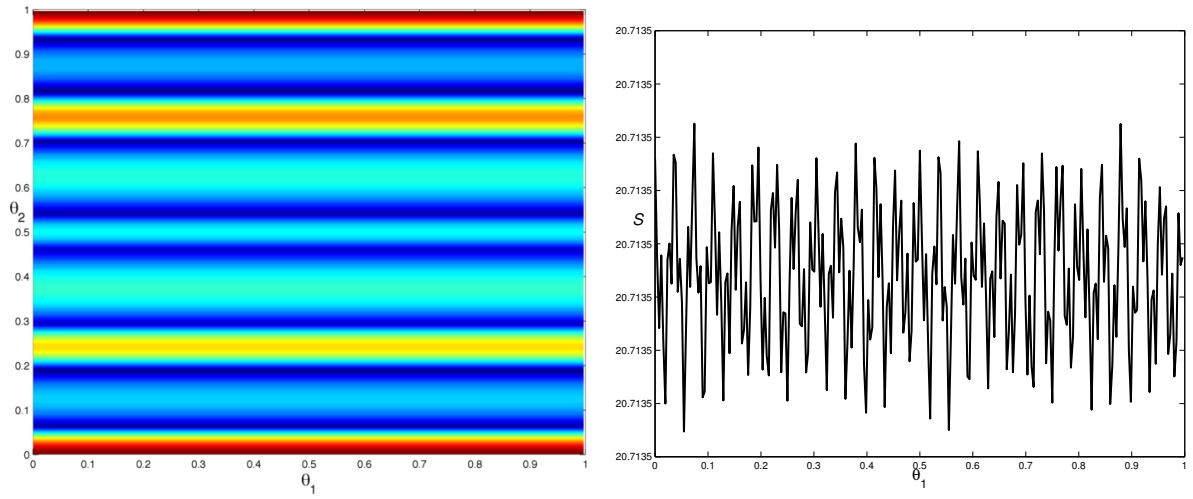

Figure 4.11: (a)Critical conjugacy for the $ll\overline{r}$ torus in the $B = 0$ ABC map at $\varepsilon = 0.0373$. The main streak forms along the line $\theta_2 \approx y = 0$, corresponding to the peak of the potential of the dominant area-preserving map defined by the y and z dimensions. (b) Largest singular value $\mathcal{S}$ as a function of θ_1 at $\theta_2 = 0$. Although there is some slight variation, it is minor relative to the global dynamics

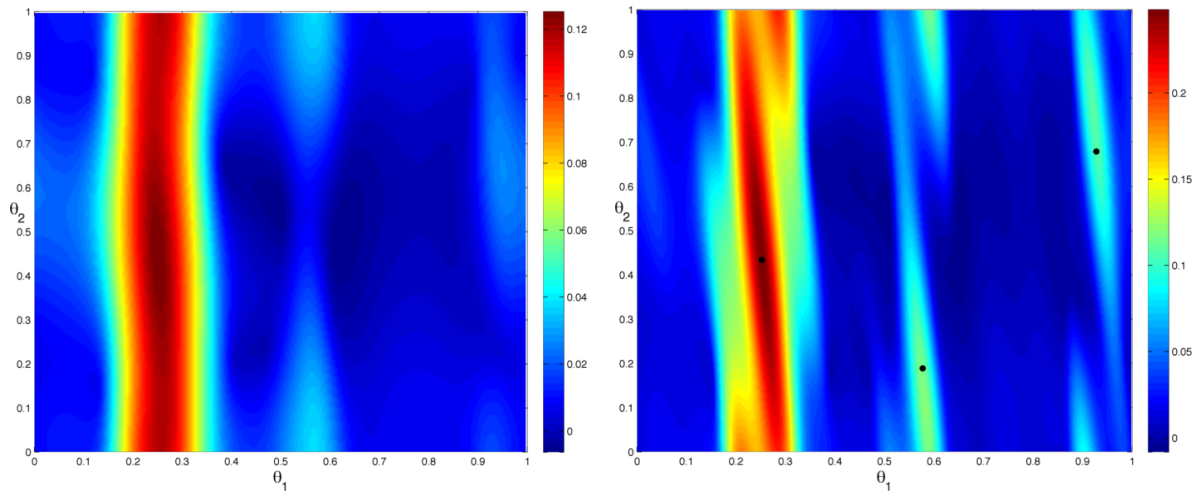

Figure 4.12: Subcritical and critical $ll\overline{r}$ conjugacies for the ABC Map with $B = \varepsilon^{3/4}$. (a) Initially, when $\varepsilon = 0.0015$, a main gap forms along the line $x = \frac{1}{4}$, similar to the breakup of tori in the $C = 0$ map. (b) The near-critical conjugacy for $\varepsilon = 0.0022$. The increased perturbation in the y direction has deformed the main map. Additional streaks have formed at the iterates of the main peak, indicated by the black dots.

$\theta = (\frac{1}{4}, 0)$, $\theta = (\frac{1}{4}, \frac{1}{2})$ and $\theta = (\frac{3}{4}, 0)$, corresponding to the intersection of the maxima and minima of the potentials for the area-preserving maps resulting from either B or C being zero. The repeated formation of dimples at these points may indicate the existence of some underlying potential-like structure.

The topology of the invariant set for $\varepsilon > \varepsilon_{cr}$ in volume-preserving maps is unknown. Indeed, examination of these tori imply that the topology may differ depending on the map and rotation number. For example, tori that form dimples may devolve into Sierpinksi gaskets, while those that exhibit the streak behavior may become a Cantor set of strips. Further deformations at larger ε are certainly possible, as is the reformation of the torus. This behavior cannot be seen in the near-critical conjugacy, and remains an open question.

Chapter 5

Final Circle

Greene conjectured that the last invariant circle of Chirikov's map has the rotation number ϕ, the golden mean (2.5). This conjecture, while never proved, is supported by strong numerical evidence [78]. More generally, the golden invariant circle will not necessarily be globally most robust, but one expects that the last invariant circle in any neighborhood has a related rotation number:

Conjecture 3. *Rotational invariant circles with noble rotation numbers are locally most robust.*

A frequency ratio $\omega = \nu_1/\nu_2$ is **noble** if the vector ν is an integral basis for the quadratic field $\mathbb{Q}(\phi)$, see App. C. Strong numerical evidence for the local robustness of the nobles for Chirikov's map was given by MacKay and Stark [84]. In §5.1, we will study the relative robustness of circles with rotation numbers from different quadratic fields for several examples of (1.9).

The local robustness conjecture implies that the critical function, $\varepsilon_{cr}(\omega)$ will have local maxima at each noble rotation number. The global maximum of this function for Chirikov's map occurs, according to Greene, at the golden mean. More generally, let ω_{max} be location of the global maximum of ε_{cr}, i.e., the rotation number of the globally most robust circle of (1.9).

Conjecture 4. *In the absence of symmetry-breaking bifurcations the rotation number of the globally most robust invariant circle for (1.9) is piecewise constant under continuous changes of (1.9).*

We are not aware of previous studies of this conjecture. Our evidence consists of studying two-parameter families $f_{\varepsilon,\psi}$, obtained by introducing an additional parameter ψ into g. The critical

function will of course depend upon ψ and typically the location of its global maximum would be a piecewise continuous function of ψ with occasional jump discontinuities as different local maxima take over as the global maximum. As we will see in §5.2, ω_{max} seems instead to be locked to fixed noble rotation numbers over intervals of ψ.

5.1 Robustness of Noble Invariant Circles

An invariant circle is **locally** most robust in a one-parameter family f_ε, if it exists for larger ε than any circle in some neighborhood in phase space. The MacKay-Greene renormalization theory [78] leads to the conjecture that the locally most robust circles for twist maps have "noble" rotation numbers, that is, $\omega \in \mathbb{Q}(\phi)$ where

$$\omega = \frac{\nu_1}{\nu_2}, \quad \nu = (a + b\phi, c + d\phi) = (1, \phi)M, \tag{5.1}$$

and the matrix $M \in SL(2, \mathbb{Z})$. In this case ν is an integral basis for the ring $\mathbb{Z}(\phi)$, and the collection of nobles is projectively equivalent to a collection of integral bases of $\mathbb{Z}(\phi)$.

It is not unexpected that the nobles are robust; for example, the size of the perturbation allowed in KAM theory is proportional to the Diophantine constant (1.7), and for any noble has the maximal value, see App. C. The most conclusive evidence for the robustness of the nobles is the numerical study of MacKay and Stark [84] for the standard map.

Here we investigate the relative robustness of nobles relative to other quadratic fields for the various generalized standard maps studied in Chapter 4. We consider the six rings $\mathbb{Z}(r)$ with the smallest discriminants, or equivalently the largest Diophantine constants, as shown in Table 5.1. To characterize the computational accuracy, we first compute the critical parameter value for Chirikov's map for circles in each ring using both the residue and the seminorm methods. Table 5.1 shows that the golden mean is, of course, the clear winner with the largest critical value, (3.20).

The error in each computation of ε_{cr} was estimated by comparing the extrapolated values from the last two iteration steps. The computations indicate that ε_{cr} is about an order of magnitude less accurate using the seminorm method; however, the error is often—but not always—overestimated

r	$D(r)$	CF	$\varepsilon_{cr}^R(r)$	$\varepsilon_{cr}^S(r)$	$\langle\Delta\varepsilon_{cr}\rangle_{rms}$
ϕ	5	$\overline{1}$	0.9716358(1)	0.971638(1)	$1.6(10)^{-6}$
$1+\sqrt{2}$	8	$\overline{2}$	0.957447(6)	0.95744(7)	$3.0(10)^{-6}$
$1+\sqrt{3}$	12	$\overline{2,1}$	0.87608(1)	0.8756(6)	$4.3(10)^{-4}$
$\frac{1}{2}(3+\sqrt{13})$	13	$\overline{3}$	0.89086(2)	0.8905(3)	$3.3(10)^{-3}$
$\frac{1}{2}(3+\sqrt{17})$	17	$\overline{3,1,1}$	0.91573762(4)	0.9143(3)	$1.0(10)^{-4}$
$\frac{1}{2}(3+\sqrt{21})$	21	$\overline{3,1}$	0.77242(5)	0.7720(8)	$2.1(10)^{-4}$

Table 5.1: The the six quadratic fields $\mathbb{Q}(r)$ with the smallest discriminants, D. Each is generated by the irrational r with the periodic continued fraction (CF) shown. The 4^{th} and 5^{th} columns give $\varepsilon_{cr}(r)$ for Chirikov's map computed by the residue method (for orbits up to period $30,000$) and the seminorm method, respectively. The parentheses indicate the estimated extrapolation error in last digit. The last column is the root mean square difference between the two computations for 256 rotation numbers in each field.

by this calculation. The error for both methods tends to increase with discriminant. This is not surprising since circles from fields with larger D tend to be closer to low order resonances. For the residue method, each periodic approximant is also nearer to lower period ones, making the orbits more difficult to compute. Similarly for the conjugacy method, a larger discriminant implies that the denominators in (3.16) will be smaller inducing larger errors in the Fourier coefficients.

To study local robustness, we construct a set of nearby rotation numbers from each ring, using the 256 rationals in $(0, \frac{1}{2}]$ from the Farey tree up to level eight, see App. B. Each pair of neighboring rationals, $(p_1/q_1, p_2/q_2)$, gives a basis vector $\nu = (p_1 + p_2 r, q_1 + q_2 r)$ for each of the six rings. The six corresponding frequency ratios (5.1) lie the interval between the neighbors. These interval widths range from 0.0002 to 0.1 and define the "local" neighborhoods for the robustness test. The last column of Table 5.1 shows the rms difference between the residue and seminorm computations for the 256 irrationals in each ring.

For a given pair of neighboring rationals, we compare the values of ε_{cr} for each of the six rings to determine which is locally most robust. Since the computations of ε_{cr} are uncertain, we are unable to determine a winner when the difference between the most robust and other circles is too small. The approximation to ε_{cr} combined with the estimated error generates a critical interval, in which the true ε_{cr} likely resides. A circle is deemed to be locally most robust if its entire critical interval is more robust than the critical intervals of the other circles. If the most robust interval

Method	ϕ	$1+\sqrt{2}$	$1+\sqrt{3}$	$\frac{1}{2}(3+\sqrt{13})$	$\frac{1}{2}(3+\sqrt{17})$	$\frac{1}{2}(3+\sqrt{21})$	Unsure
residue	173	67	10	0	0	0	6
		240	10	0	0	0	6
			255	0	0	0	1
				180	44	0	32
					256	0	0
seminorm	166	73	6	1	0	1	9
		228	9	2	1	1	15
			34	29	6	2	185
				33	7	3	213
					7	5	244

Table 5.2: The relative robustness of invariant circles of Chirikov's standard map with rotation numbers in different algebraic rings. The numbers in each column indicate the number of times a circle with rotation number in that ring was most robust. The final column is number of trials for which a winner could not be conclusively determined.

overlaps with any other interval, we cannot conclusively declare a winner. We also discounted any result for which the most robust critical interval was greater than 10^{-4}.

Table 5.2 shows the number of times each ring was most robust in a comparison with the other six rings. For the residue computation the nobles are most robust 69% of the time, and for the seminorm method, 67%. Errors caused 2-3% of the trials to be discarded. These results are similar to those of MacKay and Stark [84]. There are cases in which numbers in $\mathbb{Q}(\sqrt{2})$ appear more robust than a noble, but MacKay and Stark found that when the noble at a particular level on the Farey tree was not most robust, there was always a noble further down on the tree that was. Thus the cases in which nobles do not win the contest result from the neighborhood being too large.

If we remove the field $\mathbb{Q}(\phi)$, then a comparison of the remaining five fields (the second and seventh rows of the table) shows that $\mathbb{Q}(\sqrt{2})$ is most robust. Continuing this comparison for the remaining fields shows that robustness seems to be a monotone function of the field discriminant. However, for the seminorm method, the uncertainties are too large to determine a winner amongst the four largest discriminant fields.

It has long been conjectured that noble invariant circles should be locally most robust for maps with more general forces, with nonmontone frequency maps, and without reversing symmetries. We

$\frac{202}{\pi}\psi$	ϕ	$1+\sqrt{2}$	$1+\sqrt{3}$	$\frac{1}{2}(3+\sqrt{13})$	$\frac{1}{2}(3+\sqrt{17})$	$\frac{1}{2}(3+\sqrt{21})$	Unsure
1	165	67	6	1	2	2	13
11	156	80	2	1	1	6	10
21	154	76	5	1	2	4	14
31	160	72	6	2	2	2	12
41	160	71	2	1	3	3	16
51	158	73	5	1	2	5	12
61	152	76	3	1	2	8	14
71	164	72	0	0	2	7	11
81	163	71	3	0	1	5	13
91	163	68	7	2	2	4	10

Table 5.3: Relative robustness of circles from six quadratic fields for the generalized standard map with g_3, Ω_1 and 10 values of ψ. The number in each column corresponds to the number of times each of the six rings of Table 5.1 most robust from 256 trials. The final column is number of trials for which a winner could not be conclusively determined.

investigated this using the seminorm method for the maps of Chapter 4 and found that in each case the nobles appeared to be locally most robust to nearly the same degree that they are for Chirikov's map. For example, Table 5.3 shows the results for the generalized standard map with g_3 and Ω_1 for $\psi \in [0, \pi/2]$. Regardless of the choice of ψ, the noble circles were once again locally most robust at least 60% of the time. We suspect that—just like for Chirikov's map—whenever one of the six non-nobles was a winner, there is a noble below it on the Farey tree that wins, but we did not examine this in detail.

As a second example, Table 5.4 shows the robustness data for the nontwist map with frequency map Ω_2. In this case the symmetries of the map that allow us to restrict to $\omega \in (0, \frac{1}{2})$ are gone. We therefore studied the 512 rotation numbers generated from the rationals on level 9 of the Farey tree in the interval $(0, 1]$. We once again found that circles with noble rotation numbers are locally most robust at least 55% of the time. For this case the errors were larger, and up to 9% of the comparisons had to be discarded.

In conclusion, our results support the conjecture that invariant circles with noble rotation numbers are generically, locally most robust for the generalized standard map (1.9).

$\frac{202}{\pi}\psi$	ϕ	$1+\sqrt{2}$	$1+\sqrt{3}$	$\frac{1}{2}(3+\sqrt{13})$	$\frac{1}{2}(3+\sqrt{17})$	$\frac{1}{2}(3+\sqrt{21})$	Unsure
1	314	116	19	16	1	4	42
11	292	149	24	6	0	4	37
21	296	133	27	11	2	1	42
31	291	151	19	2	1	4	44
41	287	152	17	4	0	4	48
51	283	142	26	8	1	5	47
61	291	145	24	5	1	3	43
71	289	138	25	11	1	1	47
81	297	145	23	7	0	3	37
91	302	146	15	6	0	5	38

Table 5.4: Relative robustness data for (1.9) with $g_3(x,\psi)$ and $\Omega_2(y,0.3)$ and 10 values of ψ using the seminorm method. The number in each column corresponds to the number of times each of the six rings of Table 5.1 most robust from 512 trials. The final column is number of trials for which a winner could not be conclusively determined.

5.2 The Critical Function

The destruction of the last rotational invariant circle is a significant event in the dynamics of area-preserving maps since this corresponds to the transition to global chaos and unbounded orbits. In this section we will identify which of the nobles is globally most robust for the some of the generalized standard maps studied in Chapter 4. Since, as we confirmed in §5.1, the noble circles appear to be locally most robust, we will confine our search to these rotation numbers.

The last invariant circle is the global maximum of the **critical function** $\varepsilon_{cr}(\omega)$. The conjecture that the golden circle is most robust for Chirikov's map has been supported by many computations using periodic orbits [104, 19, 95]. It is also supported using the seminorm technique, as can be seen in Fig. 5.1(a). Here we computed $\varepsilon_{cr}(\omega)$ for 256 noble frequencies in $(0, \frac{1}{2})$ using level 8 of the Farey tree as in §5.1. The resulting picture is indistinguishable from that using the residue method and has maximum value $\varepsilon_{cr}(2-\phi) = \varepsilon_{cr}(\phi)$ of (3.20).[1]

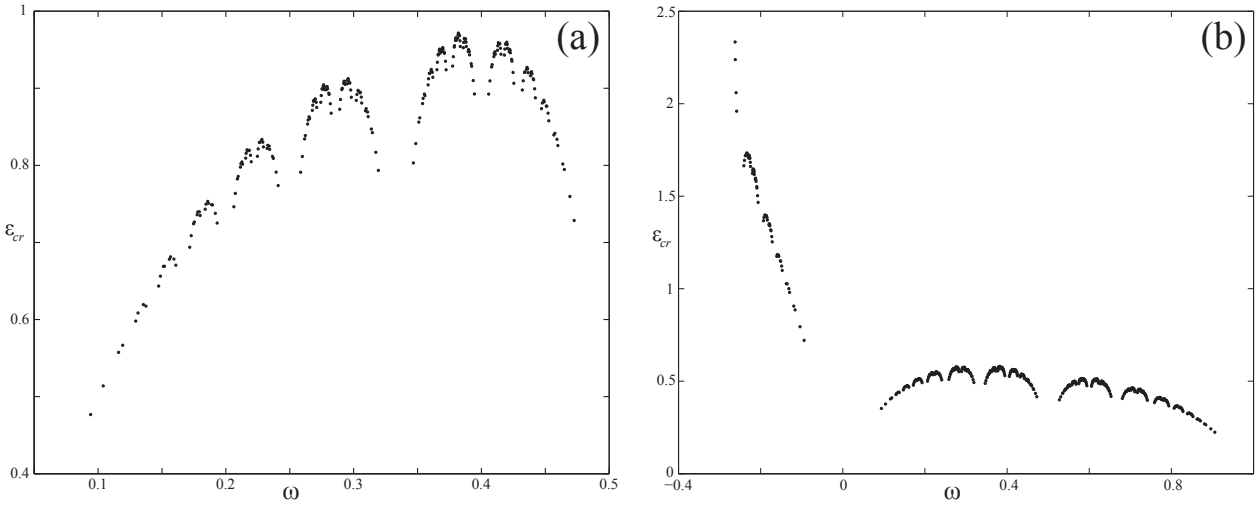

Figure 5.1: Critical functions for (a) Chirikov's standard map and (b) the standard nontwist map for $\delta = 0.3$, using the seminorm method.

Determining the globally most robust circle for the standard nontwist map, with Ω_2 and g_1, is complicated because of the lack of periodicity in frequency space. Figure 5.1(b) shows the critical

[1] Symmetries, recall App. E, imply that $\varepsilon_{cr}(\omega) = \varepsilon_{cr}(n \pm \omega)$ for $n \in \mathbb{Z}$, so it is sufficient to restrict ω to the interval $[0, \frac{1}{2}]$.

function for $-\delta < \omega < 1$ for 512 nobles generated from level 9 of the Farey tree with root $[\frac{0}{1}, \frac{1}{1}]$ and 112 negative nobles greater than $-\delta$. When $\omega > 0$, this critical function has a similar structure to Chirikov's map; however—as has been often observed [93, 108]—the circles become increasingly more robust as $\omega \to -\delta$. Indeed we found the most robust circle to be that with the smallest ω. Unfortunately, the extrapolation errors for the estimate of ε_{cr} tend to become larger in this limit: we discarded the estimates for 44 circles for which the error was larger than 10^{-4}. A similar picture of the critical function is seen for the nontwist map with the force g_3: the most robust circle was always found to be the one with rotation number closest to -δ.

The critical function is considerably more complex for the multiharmonic twist map, with Ω_1 and g_2. Though ε_{cr} resembles that for Chirikov's map when $\psi \in [\frac{\pi}{2}, \pi]$, see Fig. 5.2(a), when $\psi \in [0, \frac{\pi}{2}]$, $\varepsilon_{cr}(\omega)$ is much less regular, see Fig. 5.2(b). Recall that this region of parameters corresponds to the Cantor set of cusps in the critical set of the golden circle, e.g., Fig. 4.4(a). We also observed that $\varepsilon_{cr}(\omega)$ is especially erratic when two gaps collide, as we observed near $\psi = 0.47$ in Fig. 4.3.

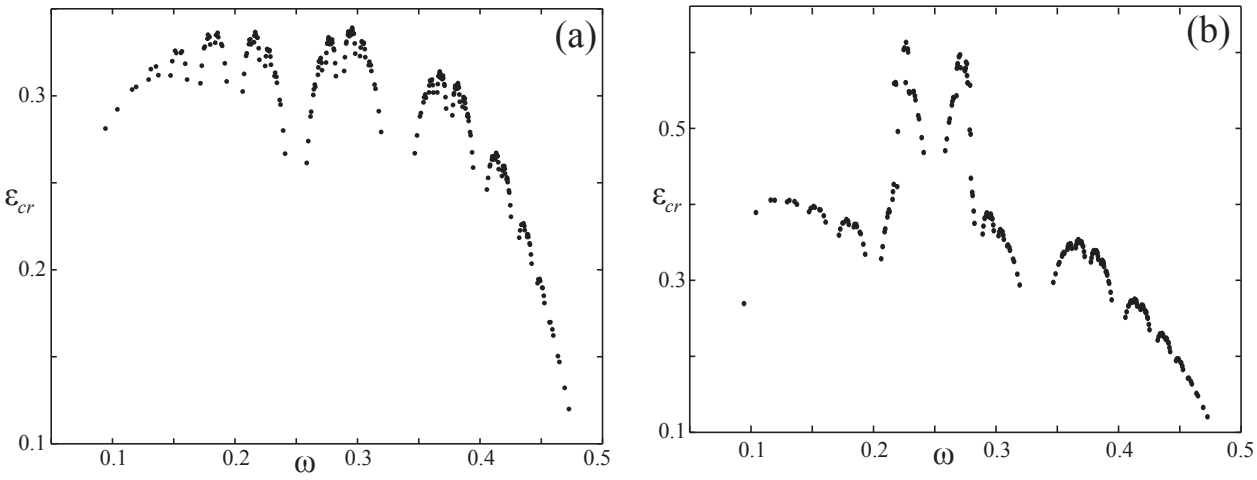

Figure 5.2: Critical function for the generalized standard map with Ω_1 and (a) $g_2(x, 2.3484)$, or (b) $g_2(x, 0.7776)$ for 256 noble rotation numbers.

5.3 Most Robust Circle

To address Conj. 4, we studied the rotation number of the most robust circle for two parameter families of generalized standard maps. In particular, studied the dependence of

$$\omega_{max} = \arg\max\{\varepsilon_{cr}(\omega)\}$$

on the parameter ψ in our various force models. To do this, we first obtained a rough estimate for the interval of rotation numbers that contains the most robust circles over a range of ψ. Then, for each value of ψ, we select the most robust circle from the 256 nobles on level 8 of the Farey tree in this interval.

For example, for a twist map with frequency map Ω_1, periodicity allows us to restrict ω to the interval $[0, \frac{1}{2}]$. The dependence of ω_{max} on the parameter ψ for the force g_3 is is shown in Fig. 5.3(a). Surprisingly, of the 256 nobles examined, only five are most robust over most of the range of ψ; their rotation numbers are shown in the figure. Each of these circles has a critical set that varies smoothly with ψ, as shown in Fig. 5.3(b).

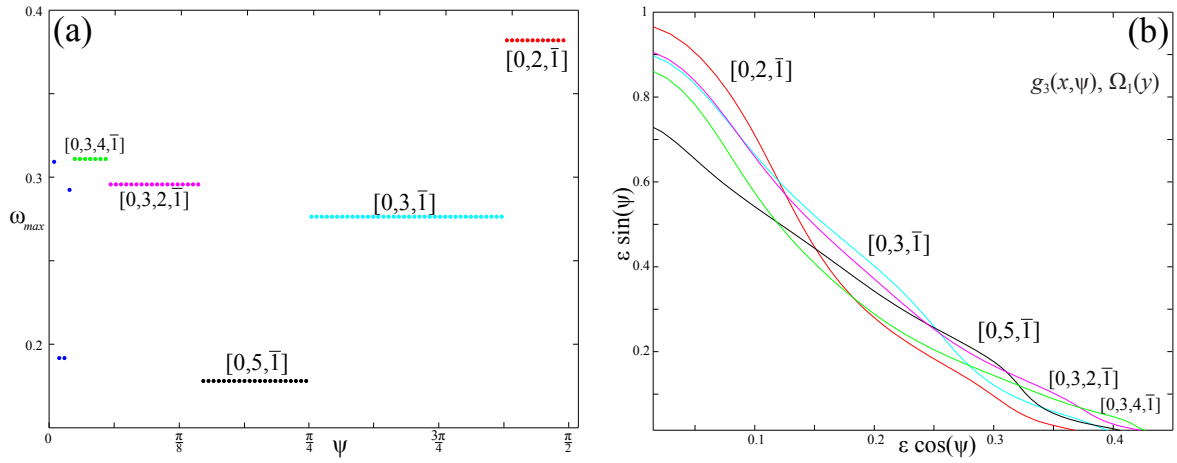

Figure 5.3: Globally most robust circles for Ω_1 and $g_3(x, \psi)$ for 100 values of $\psi \in [0, \frac{\pi}{2}]$. Labels show the continued fraction expansions of the rotation numbers for five most robust circles. (a) The rotation number of the most robust circle. (b) The critical sets, $\{(\cos\psi, \sin\psi)\varepsilon_{cr}(\omega)\}$ for the five most robust circles of (a).

The graph of $\omega_{max}(\psi)$ for this map follows a predictable pattern. As noted in Chapter 4, this map reduces to Chirikov's map at $\psi = \frac{\pi}{2}$, and to the same map on half the spatial scale at $\psi = 0$.

Thus the circle with rotation number $2-\phi = [0,2,\overline{1}]$ is most robust at $\frac{\pi}{2}$. However, when $\psi = 0$ the critical function has equal global maxima at the "half-noble" rotation numbers $\frac{1}{2}(n \pm \phi)$. For the range $[0, \frac{1}{2}]$ there are maxima at

$$\begin{aligned} \tfrac{1}{2}(\phi - 1) &= [0,3,\overline{4}], \\ \tfrac{1}{2}(2 - \phi) &= [0,5,\overline{4}]. \end{aligned} \tag{5.2}$$

For moderate ψ, the observed values of ω_{max} move logically from $2-\phi$ to one of the half-nobles, in the sense that their continued fraction expansions become increasingly similar to those of the half-nobles (5.2). This behavior persists for small ψ, shown for the 256 circles with noble rotation numbers from level 8 of the Farey tree with the root $(\frac{2}{7}, \frac{1}{3})$ in Fig. 5.4. The evolution is not monotonic-indeed, the rotation number of the most robust circle appears to oscillate about $\frac{1}{2}(\phi-1)$. For very small ψ the rotation number of the most robust circle is fixed at the noble in the sample closest to $\frac{1}{2}(\phi - 1)$.

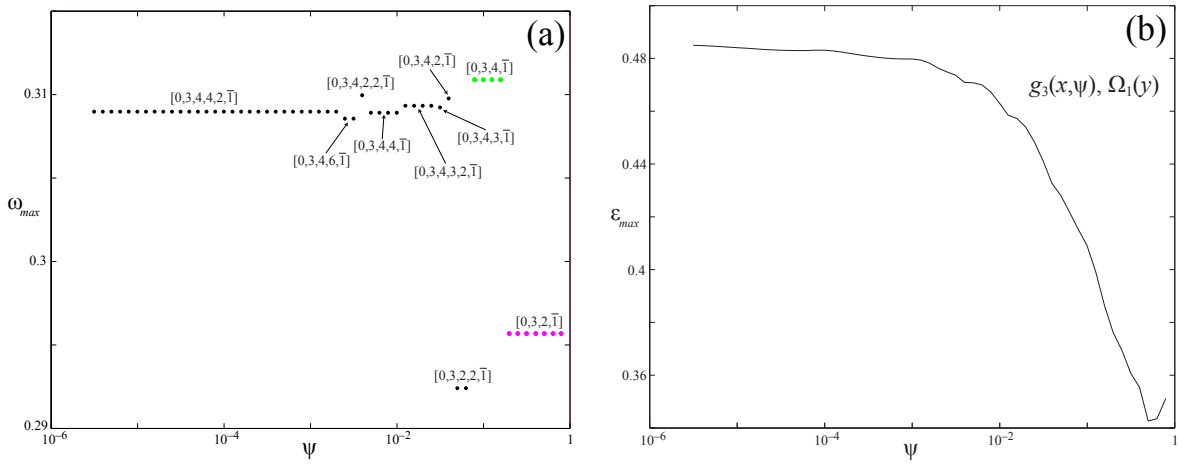

Figure 5.4: Most robust circles for Ω_1 and $g_3(x,\psi)$ for 50 values of $\psi \in [10^{-6}, 1]$ in the vicinity of $\frac{1}{2}(\phi-1)$. Labels show the continued fraction expansions of the rotation numbers of the most robust circles. (a) The rotation number of the most robust circle. (b) The critical curve, $\varepsilon_{cr}(\omega)$, for the most robust circles of (a).

The rotation number of the most robust circle seems to remain constant on intervals of the parameter ψ, at least for the twist map with force g_3. We examined several other multiharmonic twist maps in order to determine if this behavior was typical. The critical data for the generalized standard map with Ω_1 and g_4 with $\psi \in [0,1]$ is shown in Fig. 5.5, alongside the critical data for Ω_1

with

$$g_5(x;\psi) = \frac{\sin(2\pi x)}{2\pi(1+\psi\sin(4\pi x))} \tag{5.3}$$

and $\psi \in [0, 0.7]$. Since for $\psi = 0$ both maps reduce to Chirikov's map, the golden circle is most robust. As ψ grows the rotation number of the most robust circle appears to limit on $\frac{1}{2}$. Expansion about the $(1, 2)$ resonance indicates that only the even modes of the force are significant. The robustness of the circles near this resonance can therefore be explained by the relative lack of harmonic content in the even modes of g_4 and g_5.

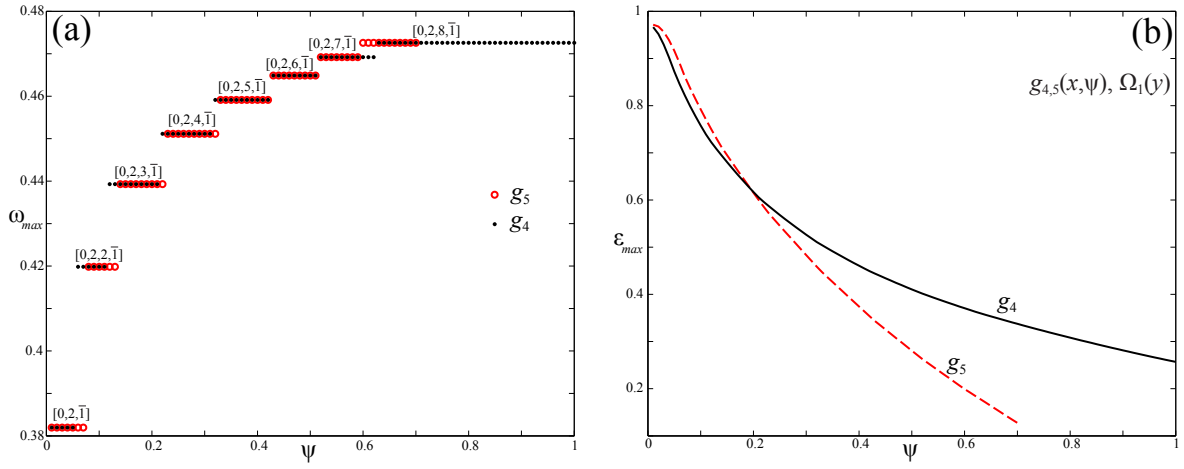

Figure 5.5: (a) $\omega_{max}(\psi)$ and (b) $\varepsilon_{cr}(\omega_{max})$ amongst 256 nobles in $[0, \frac{1}{2}]$ for the twist map with forcing g_4 (4.5) (solid black) and g_5 (5.3) (dashed red and open circles) for 100 values of $\psi \in [0, 1]$.

The fully nonreversible case with $\Omega = \Omega_3$ and $g = g_4$ displayed behavior similar to the twist maps with Ω_1. For this map, the globally most robust circle always had a small rotation number. However, the proximity of these circles to resonance led to large errors, making it difficult to determine which circle was truly most robust. To focus in on the robust region, we looked at the 64 nobles from level 6 of the Farey tree with the root $[0, \frac{1}{7}]$. To improve the accuracy of the estimates we used up to 2^{15} Fourier modes and smaller step sizes in ε, beginning with $\Delta\varepsilon = .005$, decreasing to $\Delta\varepsilon = .0001$ when that step size failed. The results, shown in Fig. 5.6, indicate that ω_{max} is again constant over intervals of ψ, with jump discontinuities. Also, just as for the Ω_1 case, $\varepsilon_{cr}(\omega_{max})$ is monotone decreasing with ψ.

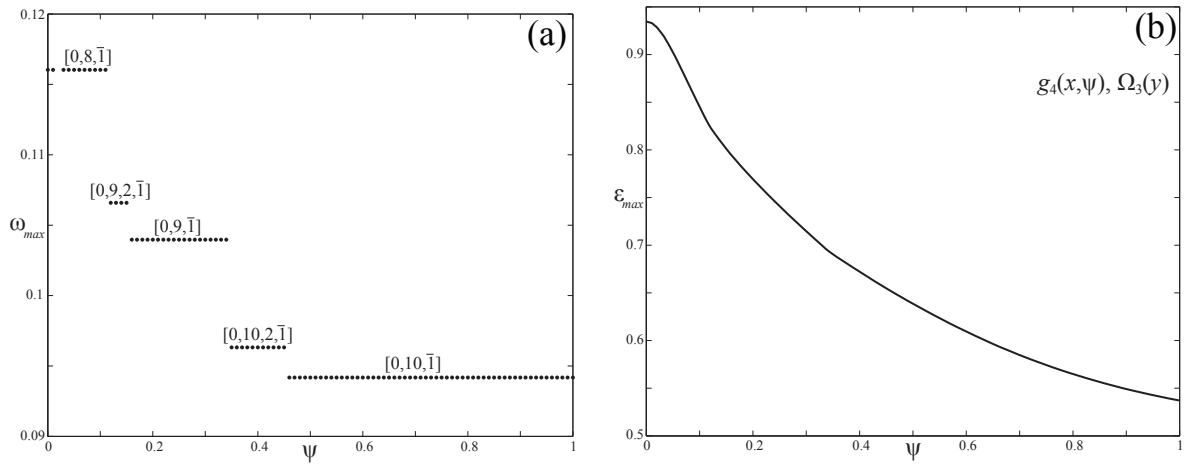

Figure 5.6: (a) $\omega_{max}(\psi)$ and (b) $\varepsilon_{cr}(\omega_{max})$ amongst 256 nobles in $[0, \frac{3}{20}]$ for the generalized standard map with $\Omega = \Omega_3$, $g = g_4$ for 100 values of $\psi \in [0, 1]$.

Finally we present an example that does not completely follow Conj. 4: the doubly-reversible, two-harmonic map (Ω_1, and g_2). As seen in Fig. 5.2, the $\varepsilon_{cr}(\omega)$ is an irregular function of ω when $\psi \in [0, \frac{\pi}{2}]$. This generates erratic behavior in ω_{max} for the same range of ψ, see Fig. 5.7. Interestingly, when $\psi \in [\frac{\pi}{2}, \pi]$ ω_{max} is piecewise constant and $\varepsilon_{cr}(\omega_{max})$ smooth as for the previous examples. Consequently, the irregular behavior in ω_{max} appears to reflect the same complex set of symmetry breaking bifurcations that are responsible for the Cantor set of cusps in the critical set for the golden circle, recall Fig. 4.4.

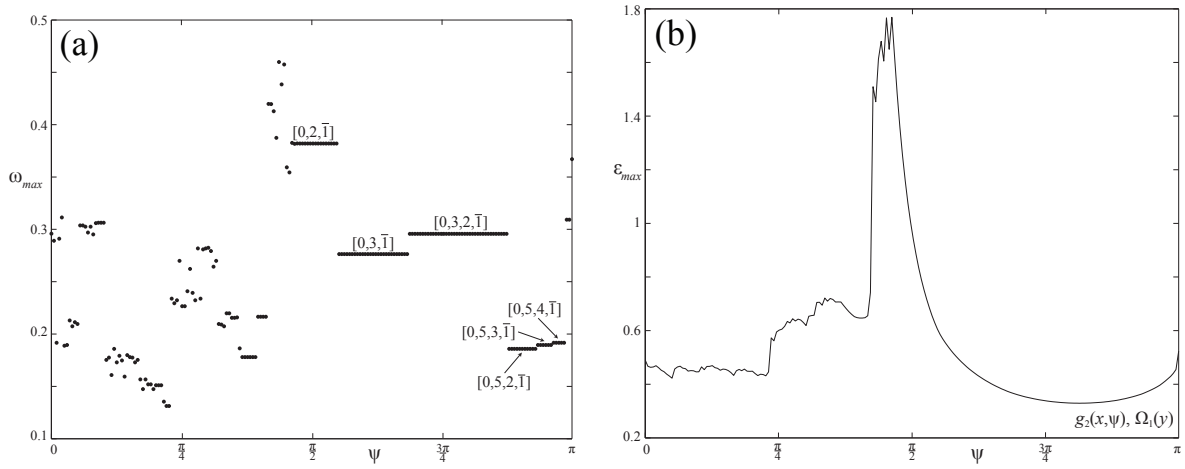

Figure 5.7: (a) $\omega_{max}(\psi)$ and (b) $\varepsilon_{cr}(\omega_{max})$ for the generalized standard map with Ω_1 and g_2 as a function of ψ, estimated using the highest peak of the critical function for 256 nobles in $[0, \frac{1}{2}]$ for each of 200 values of ψ.

Chapter 6

Spiral Tori

In §3.4.2 a method to predict the destruction of a torus in volume-preserving maps was introduced, based upon the growth of the largest singular value of the derivative of the conjugacy. In this chapter we will examine the effectiveness of this technique in both reversible and nonreversible systems.

We can compare the results from the singular value method to those from Greene's residue criterion in the reversible standard volume-preserving map, recall §2.2. Sixteen spiral mean rotation vectors were generated by adding an infinite r tail to the rational vectors from level 6 of the generalized Farey tree, see App. B, restricted to the unit square. The critical ε values for the corresponding tori were estimated using both the singular value method and Greene's criterion for orbits up to period 30,000. The close agreement of these results, shown in Table 6.1, provides significant numerical evidence of the validity of both methods, although the error estimates generally appear too small in both cases.

The results for the nonreversible ABC map (1.19) with $B = \varepsilon^2$ and $B = 2\varepsilon$ are summarized in Table 6.2. Although we cannot compare these results with Greene's residue criterion, the estimated error is of the same magnitude as that found in the standard volume-preserving map. When $B \propto \varepsilon$, ε_{cr} appears to change smoothly with B/ε, as shown in Fig. 6.1 for the $ll\overline{r}$ torus. As B grows the perturbation to the system increases, and, as expected, the torus becomes increasingly fragile, with $\varepsilon_{cr} \to 0$ as $B/\varepsilon \to \infty$.

ω	Farey Path	$\varepsilon_{cr}^{R}(r)$	$\varepsilon_{cr}^{S}(r)$	b
(.3247,.7549)	$ll\overline{r}$	0.025(4)	0262(1)	-0.5647
(.5278,.8286)	$llrrrl\overline{r}$	0.032310(2)	0.032103(2)	-0.3548
(.2068,.8439)	$llrrl\overline{r}$	0.01740(2)	0.01729(2)	-0.3805
(.1054,.6753)	$llrrll\overline{r}$	0.01267(3)	0.01228(5)	-0.5027
(.1850,.4302)	$llrl\overline{r}$	0.01242(9)	0.0124(1)	-0.9429
(.1294,.3008)	$llrlrl\overline{r}$	0.00671(4)	0.00685(8)	-1.1493
(.4809,.6370)	$llrll\overline{r}$	0.021431(6)	0.022298(2)	-0.7122
(.2451,.5698)	$llrlll\overline{r}$	0.017595(9)	0.01738(4)	-0.3743
(.5698,.3247)	$rrl\overline{r}$	.0365260(8)	0.03635(4)	-0.3924
(.6992,.5278)	$rrlrrl\overline{r}$	0.03408(2)	0.03376(1)	-0.4425
(.3630,.2068)	$rrlrl\overline{r}$	0.01051(3)	0.0105(1)	-1.1256
(.4302,.1054)	$rrlrll\overline{r}$	0.013425(6)	0.0139(2)	-1.7786
(.7549,.1850)	$rrll\overline{r}$	0.02747(3)	0.027930(5)	-1.2426
(.8286,.1294)	$rrllrl\overline{r}$	0.01324(2)	0.01332(2)	-0.9752
(.8439,.4809)	$rrlll\overline{r}$	0.02683(4)	0.02661(6)	-0.9513
(.6753,.2451)	$rrllll\overline{r}$	0.035338(4)	0.0351(1)	-0.7802

Table 6.1: The sixteen spiral mean frequencies in the unit square from level 6 of the GFT. The 3^{rd} and 4^{th} columns give $\varepsilon_{cr}(\omega)$ for the standard volume-preserving map computed by the residue method (for orbits up to period $30,000$) and the singular value method, respectively. The parentheses indicate the estimated error in last digit shown. The 5^{th} column indicates the value of b from (3.19).

ω	Farey Path	$B = 2\varepsilon$	$b_{B=2\varepsilon}$	$B = \varepsilon^2$	$b_{B=\varepsilon^2}$
(.3247,.7549)	$ll\overline{r}$	0.00651(2)	-0.6861	0.03145(5)	-2.0768
(.5278,.8286)	$llrrrl\overline{r}$	0.0055(1)	-0.7323	0.2313(8)	-0.5717
(.2068,.8439)	$llrrl\overline{r}$	0.00621(8)	-0.9936	0.03487(4)	-0.7215
(.1054,.6753)	$llrrll\overline{r}$	0.0049(2)	-1.5896	0.04333(6)	-0.8602
(.1850,.4302)	$llrl\overline{r}$	0.01100(2)	-0.3433	0.07493(8)	-0.6907
(.1294,.3008)	$llrlrl\overline{r}$	0.01037(5)	-0.4153	0.089132(9)	-0.3222
(.4809,.6370)	$llrll\overline{r}$	0.0063(3)	-0.8299	0.03430(2)	-0.4476
(.2451,.5698)	$llrlll\overline{r}$	0.009919(7)	-0.4600	0.051(2)	-0.4970
(.5698,.3247)	$rrl\overline{r}$	0.01322(2)	-0.4465	0.0248(2)	-2.1053
(.6992,.5278)	$rrlrrl\overline{r}$	0.00788(2)	-0.3772	0.02123(7)	-1.6285
(.3630,.2068)	$rrlrl\overline{r}$	0.0164(2)	-0.3044	0.03834(6)	-0.7628
(.4302,.1054)	$rrlrll\overline{r}$	0.0105(2)	-0.5506	0.002671(9)	-0.8677
(.7549,.1850)	$rrll\overline{r}$	0.0068(1)	-1.2219	0.02205(6)	-0.4839
(.8286,.1294)	$rrllrl\overline{r}$	0.0030(1)	-0.6662	0.01319(3)	-0.3132
(.8439,.4809)	$rrlll\overline{r}$	0.006071(5)	-0.4273	0.0134(2)	-1.7411
(.6753,.2451)	$rrllll\overline{r}$	0.01056(1)	-0.3776	0.0221(1)	-2.0422

Table 6.2: The sixteen spiral mean frequencies in the unit square from level 6 of the GFT. The 3^{rd} and 5^{th} columns give $\varepsilon_{cr}(\omega)$ for the ABC map computed by the singular value method with $B = 2\varepsilon$ and $B = \varepsilon^2$, respectively. The parentheses indicate the estimated error in last digit shown. The 4^{th} and 6^{th} columns indicate the value of b from (3.19).

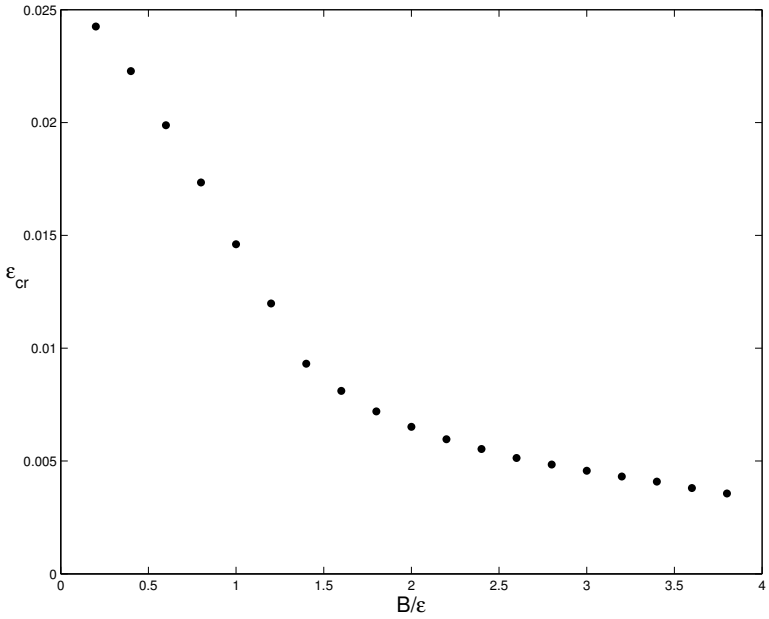

Figure 6.1: ε_{cr} for the $ll\overline{r}$ torus in the ABC map with $B \propto \varepsilon$. The critical value changes smoothly with B/ε.

6.1 B=0

Recall from §4.2 that when $B = 0$ the y and z coordinates are completely decoupled from the angle x and the system behaves as an area-preserving map with a quasi-periodically forced third dimension. The singular value method can still be exploited to predict ε_{cr} for the tori in this case, however appropriate rotation vectors must be selected. Indeed, if we attempt to compute ε_{cr} for the rotation vectors listed in Table 6.2 the resulting approximations have large errors. These errors are analogous those found in the generalized standard map for circles whose rotation numbers are drawn from quadratic rings with large discriminant, recall Chapter 5.

Rotation vectors for the $B = 0$ ABC map must be chosen such that both second component and the full vector are sufficiently irrational. The irrationality of the second component, ω_2, is fundamental as it governs the dynamics of the dominant area-preserving map defined by the y and z dimensions. Although spiral mean vectors are $\mathcal{D}_2$, the individual components may be easily approximable, ie (1.7) may not hold for $s = 1$.

We attempted to construct appropriate rotation vectors by pairing the first component from

the vectors in Table 6.2 with the noble numbers generated from the rationals located on level 4 of the Farey tree between 0 and 1. Although this pairing is not guaranteed to be $\mathcal{D}_2$, the second components will be $\mathcal{D}_1$. The error in the approximations to ε_{cr} dropped dramatically in nearly every case. Indeed, these errors are of the same magnitude as those found when computing ε_{cr} for the spiral tori in the standard volume-preserving map.

In one case, the approximation of ε_{cr} for a rotation vector consisting of a spiral mean irrational paired with a noble number had a large error. We hypothesized that this irrational vector was relatively easy to approximate with rationals. A distance between a rational $p \in \mathbb{Z}^2$ and an irrational ω with fixed denominator can be defined as a function of the denominator q,

$$d(q) = \inf_{p \in \mathbb{Z}^2} ||q\omega - p||_\infty. \tag{6.1}$$

The local minima of this distance are plotted in Fig. 6.2 for two rotation vectors that lead to small errors in approximating ε_{cr} and the one vector that had large error. The rotation vector corresponding to the estimate with large error is approximated more closely using $q = 809$ than the other rotation vectors are using $q > 50000$. This proximity to a relatively low-order resonance likely caused the large error in approximating ε_{cr}.

The dynamics of the $B = 0$ map are therefore largely two-dimensional, governed by ω_2, however the three-dimensional dynamics are still important. Both the full rotation vector ω and the second component of the vector, ω_2, must be sufficiently irrational. This property does not carry over to the ABC map with $B \neq 0$. The critical ε values were estimated in the $B = 2\varepsilon$ map for the rotation vectors comprised of spiral and noble pairs. The errors in these approximations generally grew significantly relative to the error for the spiral mean rotation vectors. In this case it is essential that the vector, not the individual components, be Diophantine.

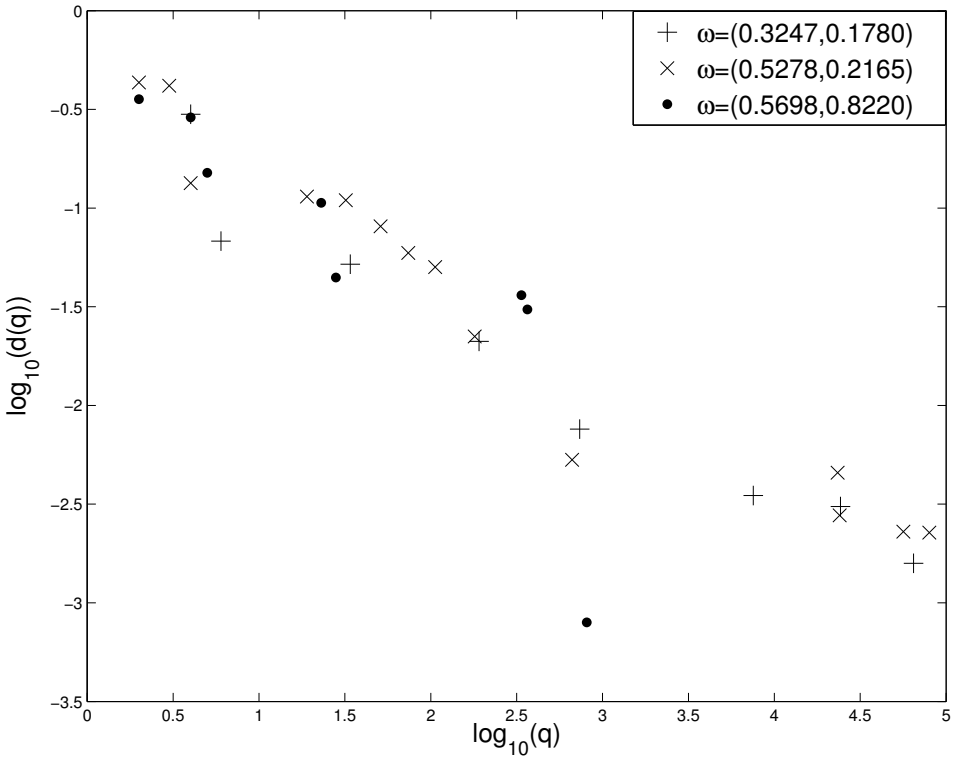

Figure 6.2: The distance (6.1) for three rotation vectors consisting of a spiral mean irrational paired with a noble number. The crosses and plusses correspond to a torus for which the approximation to ε_{cr} seems to be accurate, while the points correspond to the torus with a large error in approximating ε_{cr}.

Chapter 7

Conclusion

Our investigations into volume-preserving maps have given support for several conjectures:

In §2.2 we introduced a volume-preserving map that generalized the standard map (1.9) to three-dimensions, (2.12). The image of the frequency map $\Omega(z)$ was a one-dimensional subspace of the frequency space $\mathbb{R}^2$. Periodic orbits therefore only existed if their rotation vectors were along this curve. However, we were able to circumvent this problem by changing Ω, introducing δ as an essential parameter in the frequency map, $\Omega = \Omega(z, \delta)$.

Conjecture. *For each rational rotation vector m/n in the range of $\Omega(z, \delta)$ and for each ε, there is a δ such that (2.12) has type a (m, n)-periodic orbit.*

This conjecture is the analogue of the Poincaré-Birkhoff theorem, and seems to be open for the volume-preserving case.

Then, in §2.2.4, we exploited the fact that one of the multipliers of a symmetric orbit is always one to obtain a natural generalization of Greene's residue, (2.25). Greene found that the residue of every (m, n) periodic orbit of Chirikov's map, (1.15), behaved like $R = \mathcal{O}(\varepsilon^n)$ for $\varepsilon \ll 1$ [54]. The asymptotic behavior of the residue in volume-preserving maps is more complicated, recall §2.4.

Conjecture. *The residue (2.25) of each (m, n) orbit of (2.12) with force (2.11) grows as ε or ε^2 for $\varepsilon \ll 1$ and as ε^{n-1} or ε^n for $\varepsilon \gg 1$.*

The viability of Greene's residue criterion for volume-preserving maps was tested for an invariant torus with a rotation vector from the spiral mean algebraic field in §2.5.1. The Kim-

Ostlund generalized Farey tree, described in App. B, was employed to generate a sequence of approximating periodic orbits. We found that the residue for periodic orbits with large n underwent a dramatic shift from very small to exponentially large as ε grew, allowing us to predict the destruction of the torus with reasonable accuracy.

Conjecture. *If the residue of a sequence of symmetric (m, n)-orbits limits to zero when $m/n \to \omega$ for a Diophantine rotation vector ω, then there is a rotational invariant torus with that rotation vector. In other words, Greene's residue criterion holds.*

This conjecture is analogous to Tompaidis's theorem for the symplectic case [110].

Conjecture. *Conversely, if the residues of such a sequence are unbounded then the corresponding torus does not exist.*

This conjecture should be valid if the orbits converge to a remnant torus with positive Lyapunov exponent as shown by [44]. Of course, we do not know if such a remnant exists.

Although Greene's criteria can accurately predict the destruction of tori in volume-preserving maps the residue (2.25) is only defined for symmetric periodic orbits. Furthermore, applying Greene's criteria to nonreversible area-preserving maps is numerically expensive. We therefore explored alternative methods to determine the existence of a torus with given rotation number. In Chapter 3 we described a quasi-Newton, Fourier-based scheme to numerically compute an invariant rotational torus in a three-dimensional volume-preserving map with two angles and one action, based upon a similar algorithm for symplectic maps derived by de la Llave [35, 46, 59]. Then, in §3.4, we demonstrated that the growth of the Sobolev seminorm of the conjugacy or the largest singular value of the derivative of the conjugacy can be used to predict the destruction of a torus.

Conjecture. *If k is the embedding of an analytic rotational torus of a volume-preserving map then the seminorm $||k||_m$ (3.18) and largest singular value of Dk approach ∞ as $\varepsilon \to \varepsilon_{cr}$ asymptotically like (3.19).*

This growth can be used to approximate ε_{cr} with reasonable accuracy.

In Chapter 4 we used the algorithm developed in Chapter 3 to explore how the tori are destroyed. Aubry-Mather [85, 6] and AI [7] theory describe this breakup for area-preserving twist maps, however these theories do not easily generalize to nontwist or volume-preserving maps. The stretching in the near-critical conjugacies of circles in the generalized standard map (1.9) with various forcings g and frequency maps Ω suggested that the invariant rotational circles became cantori after their destruction.

Conjecture. *When a rotational invariant circle of the generalized standard map (1.9) is destroyed it becomes a cantorus.*

Although we were unable to surmise the topology of the invariant rotational sets for $\varepsilon > \varepsilon_{cr}$ in three-dimensional volume-preserving maps, we did gain insight into how they are destroyed.

Conjecture. *A rotational invariant torus of a three-dimensional volume-preserving map with one action and two angles is destroyed by the formation of a single or multiple "holes".*

The method to predict the destruction of tori presented in §3.4 allowed us to explore the locally and globally most robust tori in reversible and nonreversible generalized standard maps, (1.9). Greene [54] conjectured that the circle with golden mean rotation number was globally most robust in Chirikov's map (1.15). This conjecture, and the more general claim that noble numbers are locally most robust, is supported by strong numerical evidence [78, 84]. We explored the local robustness of circles with rotation numbers from different quadratic rings in the generalized standard map (1.9) with various forces and frequency maps.

Conjecture. *Rotational invariant circles of the generalized standard map (1.9) with noble rotation numbers are locally most robust.*

We then tested the noble circles to determine which was globally most robust. We found that the rotation number of the globally most robust torus behaved predictably, except in the presence of symmetry-breaking bifurcations.

Conjecture. *In the absence of symmetry-breaking bifurcations the rotation number of the globally most robust invariant circle for (1.9) is piecewise constant under continuous changes of (1.9).*

This dissertation has also motivated numerous questions for further study

(1) Is there an analogue of the dominant symmetry line for reversible maps like (2.12)? More generally, is there a pattern to the signs of the residues and their oscillations for the various symmetric families of orbits?

(2) Does the critical spiral torus have a particular threshold residue analogous to $R_{th} \approx 0.25$ for the noble tori of area-preserving maps?

(3) Is there some significance to the oscillations in sign of the residues of the approximating periodic orbits, particularly near the cusps in the critical set shown in Fig. 2.14?

(4) Do the periodic orbits that are best approximants to a Diophantine rotation vector have any special significance in approximating the corresponding invariant torus?

(5) Are there remnant tori analogous to the cantori of twist maps? The remnant tori shown in Fig. 2.13 and Fig. 4.9 appear to be similar to a Sierpinski carpet. Is this true? It is known that symplectic maps of the form (1.2) have invariant Cantor sets when $\varepsilon \gg 1$ for every rotation vector [80], but no similar results are known for volume-preserving maps.

(6) Is there a cubic field that, like the golden mean for twist maps, gives rise to locally most robust tori in the volume-preserving case? Several other fields, in addition to the spiral field that we have studied, have been proposed [71, 111, 24].

(7) More generally, is the local robustness of tori in volume-preserving maps related to the discriminant or Diophantine constant of the rotation vector?

(8) Is there an analogue of the potential for volume-preserving maps? Can the location of the main gaps be predicted?

(9) Is there a way to predict the geometry of the gaps that form in volume-preserving maps?

(10) Is the rotation vector of the globally most robust invariant circle for (2.12) is piecewise constant under continuous changes of (2.12)?

(11) Can the concepts of anti-integrability be extended to general volume-preserving maps?

The dynamics of invariant rotational tori in volume-preserving maps is an intriguing and worthwhile area of research. This dissertation has presented methods to determine their existence and, should they exist, locate them in phase space. These techniques can now be employed to explore mappings in fluid mechanics, celestial mechanics, magnetic field-line dynamics, and a multitude of other fields. I have thoroughly enjoyed this work, and look forward to building upon the foundation laid out in this thesis.

Bibliography

[1] A. Apte, R. de la Llave, and N.P. Petrov. Regularity of critical invariant circles of non-twist maps. Nonlinearity, 18:1173–, 2004. http://dx.doi.org/10.1088/0951-7715/18/3/013.

[2] A. Apte, A. Wurm, and P.J. Morrison. Renormalization and destruction of $1/\gamma^2$ tori in the standard nontwist map. Chaos, 13(2):421–433, 2003. http://dx.doi.org/10.1063/1.1555472.

[3] V.I. Arnold. Mathematical Methods of Classical Mechanics. Springer-Verlag, New York, 1978.

[4] R. Artuso, G. Casati, and D.L. Shepelyansky. Breakdown of universality in renormalization dynamics for critical invariant torus. Europhys. Lett, 15(4):381–386, 1991. http://dx.doi.org/10.1209/0295-5075/15/4/003.

[5] R. Artuso, G. Casati, and D.L. Shepelyansky. Break-up of the spiral mean torus in a volume-preserving map. Chaos Solitons Fractals, 2(2):181–190, 1992. http://dx.doi.org/10.1016/0960-0779(92)90007-A.

[6] S. Aubry. The twist map, the extended frenkel-kontorova model and the devil's staircase. Physica D, 7:240–258, 1983.

[7] S. Aubry and G. Abramovici. Chaotic trajectories in the standard map, the concept of anti-integrability. Physica D, 43:199–219, 1990.

[8] S. J. Aubry. Anti-integrability in dynamical and variational problems. Physica D, 86:284–296, 1995.

[9] C. Baesens and R. S. MacKay. Cantori for multiharmonic maps. Physica D, 69(12):59–76, 1993. http://www.sciencedirect.com/science/article/pii/0167278993901809.

[10] C. Baesens and R.S. MacKay. The one to two-hole transition in cantori. Physica D, 71:372–389, 1994.

[11] G. Birkhoff. The restricted problem of three bodies. Rendiconti del Circolo Matematico di Palermo, 39:265–334, 1915.

[12] Timothy Blass and Rafael de la Llave. Kam theory for volume-preserving maps. In Progress.

[13] O.J. Bogoyavlenskij. Extended integrability and bi-Hamiltonian systems. Comm. Math. Phys., 196:19–51, 1998. http://dx.doi.org/10.1007/s002200050412.

[14] E.M. Bollt and J.D. Meiss. Breakup of invariant tori for the four-dimensional semi-standard map. Physica D, 66(3&4):282–297, 1993. http://dx.doi.org/10.1016/0167-2789(93)90070-H.

[15] F. Borgonovi and D.L. Shepelyansky. Breaking of analyticity in 2 coupled Frenkel-Kontorova chains. Europhys. Lett., 21(4):413–418, 1993. http://dx.doi.org/10.1209/0295-5075/21/4/006.

[16] H.W. Broer, G.B. Huitema, F. Takens, and B.L.J. Braaksma. Unfoldings and bifurcations of quasi-periodic tori, volume 83. AMS, Providence, R.I., USA, 1990.

[17] H.W. Broer, George B. Huitema, and M.B. Sevryuk. Quasi-periodic motions in families of dynamical systems : order amidst chaos, volume 1645 of Lecture Notes in Mathematics. Springer, Berlin, 1996.

[18] S. Bullett. Invariant circles for the piecewise-linear standard map. Comm. Math. Phys., 107:241–262, 1986. http://projecteuclid.org/euclid.cmp/1104116023.

[19] N. Buric, I.C. Percival, and F. Vivaldi. Critical function and modular smoothing. Nonlinearity, 3:21–37, 1990.

[20] R. Calleja and R. de la LLave. Computation of the breakdown of analyticity in statistical mechanics models: numerical results and a renormalization group explanation. Journal of Statistical Physics, 141:940–951, 2010. http://www.ima.umn.edu/ calleja/Cal-Lla-10-2.pdf.

[21] R. Calleja and R. de la LLave. A numerically accessible criterion for the breakdown of quasi-periodic solutions and its rigorous justificaition. Nonlinearity, 23:2029–2058, 2010. http://www.ima.umn.edu/ calleja/Cal-Lla-10.pdf.

[22] J.H.E. Cartwright, M. Feingold, and O. Piro. Chaotic advection in three dimensional unsteady incompressible laminar flow. J. of Fluid Mech., 316:259–284, 1996. http://dx.doi.org/10.1017/S0022112096000535.

[23] J.W.S Cassels. An Introduction to Diophantine Approximation. Cambridge University Press, Cambridge, 1957.

[24] A. Celletti, C. Falcolini, and U. Locatelli. On the break-down threshold of invariant tori in four dimensional maps. Reg. & Chaotic Dyn., 9(3):227–253, 2004. http://dx.doi.org/10.1070/RD2004v009n03ABEH000278.

[25] C. Chandre and H.R. Jauslin. Strange attractor for the renormalization flow for invariant tori of Hamiltonian systems with two generic frequencies. Phys. Rev. E, 61:1320–1328, 2000.

[26] C. Chandre, J. Laskar, G. Benfatto, and H. R. Jauslin. Determination of the threshold of the break-up of invariant tori in a class of three frequency Hamiltonian systems. Physica D, 154:159–170, 2001. http://dx.doi.org/10.1016/S0167-2789(01)00268-8.

[27] C. Chandre and R.S. MacKay. Approximate renormalization with codimension-one fixed point for the break-up of some three-frequency tori. Phys. Lett. A, 275(5-6):394–400, 2000. http://dx.doi.org/10.1016/S0375-9601(00)00599-5.

[28] C-Q. Cheng and Y.-S. Sun. Existence of invariant tori in three-dimensional measure-preserving mappings. Celestial Mech. and Dyn. Astron., 47(3):275–292, 1990. http://dx.doi.org/10.1007/BF00053456.

[29] C.-Q. Cheng and Y.-S. Sun. Existence of periodically invariant curves in 3-dimensional measure-preserving mappings. Celestial Mech. and Dyn. Astron., 47:293–303, 1990. http://dx.doi.org/10.1007/BF00053457.

[30] B.V. Chirikov. A universal instability of many-dimensional oscillator systems. Phys. Rep., 52:265–379, 1979.

[31] T.W. Cusick. Formulas for some Diophantine approximation constants. Math. Ann., 197:183–188, 1972. http://dx.doi.org/10.1007/BF01428224.

[32] T.W. Cusick. The two-dimensional Diophantine approximation constant. Monatshefte fr Mathematik, 78:297–304, 1974.

[33] T.W. Cusick. The two-dimensional Diophantine approximation constant. II. Pacific. J. Math., 105(1):53–67, 1983.

[34] R. De La Llave. A tutorial on KAM theory. In Smooth ergodic theory and its applications (Seattle, WA, 1999), volume 69 of Proc. Sympos. Pure Math., pages 175–292. Amer. Math. Soc., Providence, 2001.

[35] R. de la Llave, A. González, Á Jorba, and J Villanueva. KAM theory without action-angle variables. Nonlinearity, 18:855–895, 2005. http://iopscience.iop.org/0951-7715/18/2/020/.

[36] R. de la Llave and N.P. Petrov. Regularity of conjugacies between critical circle maps: An experimental study. Experiment. Math., 11(2):219–241, 2002.

[37] D. del Castillo-Negrete, J.M. Greene, and P.J. Morrison. Area preserving nontwist maps: Periodic orbits and transition to chaos. Physica D, 91(1&2):1–23, 1996. http://dx.doi.org/10.1016/0167-2789(95)00257-X.

[38] A. Delshams and R. de la Llave. KAM theory and a partial justification of Greene's criterion for nontwist maps. SIAM J. Math. Anal., 31(6):1235–1269, 2000. http://dx.doi.org/10.1137/S003614109834908X.

[39] J.E. Dennis and R.B. Schnabel. Numerical Methods for Unconstrained Optimization and Nonlinear Equations. SIAM, Philadelphia, 1996.

[40] H.R. Dullin, H. Lomelí, and J.D. Meiss. Symmetry reduction by lifting for maps. Nonlinearity, Submitted, 2011.

[41] H.R. Dullin and J.D. Meiss. Nilpotent normal forms for a divergence-free vector fields and volume-preserving maps. Phys. D, 237(2):155–166, 2008.

[42] H.R. Dullin and J.D. Meiss. Quadratic volume-preserving maps: Invariant circles and bifurcations. SIAM J. Appl. Dyn. Sys., 8(1):76–128, 2009. http://link.aip.org/link/?SJA/8/76.

[43] H.R. Dullin and J.D. Meiss. Resonances and twist in volume-preserving mappings. Siam J. Dyn. Sys., 11:319–359, 2012. http://dx.doi.org/10.1137/110846865.

[44] C. Falcolini and R. de la Llave. A rigourous partial justification of Greene's criterion. J. Stat. Phys., 67(3/4):609–643, 1992. http://dx.doi.org/10.1007/BF01049722.

[45] L.P. Feingold, M. Kadanoff and O. Piro. Passive scalars, three-dimensional volume-preserving maps, and chaos. J. Stat. Phys., 50(3/4):529–565, 1988.

[46] Ernest Fontich, R. de la Llave, and Yannick Sire. Construction of invariant whiskered tori by a parameterization method. part i: Maps and flows in finite dimensions. J. Diff. Eqns., 246(8):3136–3213, 2009. http://www.sciencedirect.com/science/article/pii/S0022039609000655.

[47] Adam M. Fox and James D. Meiss. Greene's residue criterion for the breakup of invariant tori of volume-preserving maps. Physica D, 243(1):45–63, 2012. http://www.sciencedirect.com/science/article/pii/S016727891200245X.

[48] Adam M. Fox and James D. Meiss. Critical invariant circles in asymmetric, multi-harmonic standard maps. 2013. In Progress.

[49] Matteo Frigo. A fast fourier transform compiler. Proceedings of the 1999 ACM SIGPLAN Conference of Programming Language Design and Implementation, 1999. http://www.fftw.org/.

[50] C. Froeschlé and J.P. Scheidecker. Numerical study of a four dimensional mapping II. Astron. and Astrophys., 22:431–436, 1973.

[51] K. Fuchss, A. Wurm, A. Apte, and P. J. Morrison. Breakup of shearless meanders and outer tori in the standard nontwist map. Chaos, 16:033120, 2006. http://dx.doi.org/10.1063/1.2338026.

[52] D.L. Goroff. Hyperbolic sets for twist maps. Ergodic Theory and Dynamical Systems, 5:337–339, 1985. http://dx.doi.org/10.1017/S0143385700002996.

[53] J.M. Greene. Two-dimensional measure-preserving mappings. J. Math. Phys., 9:760–768, 1968. http://dx.doi.org/10.1063/1.1664639.

[54] J.M. Greene. A method for determining a stochastic transition. J. Math. Phys, 20(6):1183–1201, 1979. http://dx.doi.org/10.1063/1.524170.

[55] J.M. Greene, H. Johannesson, B. Schaub, and H. Suhl. Scaling anomaly at the critical transition of an incommensurate structure. Phy. Rev. A, 36(12):5858–5861, 1987. http://pra.aps.org/abstract/PRA/v36/i12/p5858_1.

[56] G.H. Hardy and E.M. Wright. An Introduction to the Theory of Numbers. Oxford Univ. Press, Oxford, 1979. Theorem 25.

[57] J. E. Howard and J. Humpherys. Nonmonotonic twist maps. Physica D, 80(3):256–276, 1995.

[58] B. Hu and J.M. Mao. Transitions to chaos in higher dimensions. In B.L. Hao, editor, Directions in Chaos, volume 1, pages 206–271. World Scientific, Singapore, 1988.

[59] G Huguet, R de la Llave, and Sire Y. Fast numerical algorithms for the computation of invariant tori in hamiltonian systems. Preprint 09-2, 2009. http://www.ma.utexas.edu/mp_arc/c/09/09-2.pdf.

[60] J. Juang, Ming-Chia Li, and Mikhail Malkin. Chaotic difference equations in two variables and their multidimensional perturbations. Nonlinearity, 21(5):1019–1040, 2008.

[61] J.A. Ketoja and R.S. MacKay. Fractal boundary for the existence of invariant circles for area-preserving maps: Observations and renormalization explanation. Physica D, 35:318–334, 1989. http://dx.doi.org/10.1016/0167-2789(89)90073-0.

[62] J.A. Ketoja and R.S. MacKay. Rotationally ordered periodic orbits for multiharmonic area-preserving maps. Physica D, 73:388–398, 1994.

[63] K. Khanin, J.L. Dias, and J. Merklof. Multidimensional continued fractions, dynamical renormalization and KAM theory. Comm. Math. Phys., 270:197–231, 2007. http://dx.doi.org/10.1007/s00220-006-0125-y.

[64] S.-H. Kim and S. Ostlund. Simultaneous rational approximations in the study of dynamical systems. Phys Rev A, 34(4):3426–3434, 1986. http://dx.doi.org/10.1103/PhysRevA.34.3426.

[65] H.T. Kook and J.D. Meiss. Periodic-orbits for reversible, symplectic mappings. Physica D, 35(1-2):65–86, 1989. http://dx.doi.org/10.1016/0167-2789(89)90096-1.

[66] S. Kurosaki and Y. Aizawa. Breakup process and geometrical structure of high-dimensional KAM tori. Prog. of Theor. Phys., 98(4):783–793, 1997. http://dx.doi.org/10.1143/PTP.98.783.

[67] J.C. Lagarias. Geodesic multidimensional continued fractions. Proc. London Math. Soc., 69:464–488, 1994.

[68] J.W.S. Lamb. Area-preserving dynamics that is not reversible. Physica A, 228:344–365, 1996.

[69] J.W.S. Lamb and J.A.G. Roberts. Time-reversal symmetry in dynamical systems: A survey. Physica D, 112:1–39, 1998. http://dx.doi.org/10.1016/S0167-2789(97)00199-1.

[70] Ming-Chia Li and Mikhail Malkin. Topological horseshoes for perturbations of singular difference equations. Nonlinearity, 4:795–811, 2006.

[71] P. Lochak. Canonical perturbation theory via simultaneous approximation. Russ. Math. Surv., 47(6):59–140, 1992. http://dx.doi.org/10.1070/RM1992v047n06ABEH000965.

[72] H. Lomelí and J.D. Meiss. Resonance zones and lobe volumes for volume-preserving maps. Nonlinearity, 22:1761–1789, 2009. http://www.iop.org/EJ/abstract/0951-7715/22/8/001/.

[73] H. E. Lomelí and R. Calleja. Heteroclinic bifurcations and chaotic transport in the two-harmonic standard map. Chaos, 16(2), 2006. http://dx.doi.org/10.1063/1.2179647.

[74] H.E. Lomelí and J.D. Meiss. Quadratic volume-preserving maps. Nonlinearity, 11(3):557–574, 1998. http://dx.doi.org/10.1088/0951-7715/11/3/009.

[75] H.E. Lomelí and J.D. Meiss. Generating forms for exact volume-preserving maps. Disc. Cont. Dyn. Sys. Series S, 2(2):361–377, 2009.

[76] H.E. Lomelí, J.D. Meiss, and R. Ramírez-Ros. Canonical melnikov theory for diffeomorphisms. Nonlinearity, 21:485–508, 2008. http://www.iop.org/EJ/abstract/0951-7715/21/3/007.

[77] R.S. MacKay. Greene's residue criterion. Nonlinearity, 5(1):161–187, 1992. http://dx.doi.org/10.1088/0951-7715/5/1/007.

[78] R.S. MacKay. Renormalisation in Area-Preserving Maps, volume 6 of Adv. Series in Nonlinear Dynamics. World Scientific, Singapore, 1993.

[79] R.S. MacKay and J.D. Meiss. Linear stability of periodic orbits in Lagrangian systems. Phys. Lett. A, 98:92–94, 1983. http://dx.doi.org/10.1016/0375-9601(83)90735-1.

[80] R.S. MacKay and J.D. Meiss. Cantori for symplectic maps near the anti-integrable limit. Nonlinearity, 5:149–160, 1992. http://dx.doi.org/10.1088/0951-7715/5/1/006.

[81] R.S. MacKay, J.D. Meiss, and I.C. Percival. Transport in Hamiltonian systems. Physica D, 13:55–81, 1984. http://dx.doi.org/10.1016/0167-2789(84)90270-7.

[82] R.S. MacKay, J.D. Meiss, and J. Stark. An approximate renormalization for the break-up of invariant tori with three frequencies. Phys. Lett. A, 190(5-6):417–424, 1994. http://dx.doi.org/10.1016/0375-9601(94)90726-9.

[83] R.S. MacKay and I.C. Percival. Converse KAM: Theory and practice. Comm. Math. Phys., 98:469–512, 1985. http://dx.doi.org/10.1007/BF01209326.

[84] R.S. MacKay and J. Stark. Locally most robust circles and boundary circles for area-preserving maps. Nonlinearity, 5:867–888, 1992. http://iopscience.iop.org/0951-7715/5/4/002.

[85] J.N. Mather. Existence of quasi-periodic orbits for twist homeomorphisms of the annulus. Topology, 21:457–467, 1982.

[86] S.W. Meier, R.M. Lueptow, and J.M. Ottino. A dynamical systems approach to mixing and segregation of granular materials in tumblers. Adv. Phys., 56(5):757–827, 2007. http://dx.doi.org/10.1080/00018730701611677.

[87] J.D. Meiss. Symplectic maps, variational principles, and transport. Rev. of Mod. Phys., 64(3):795–848, 1992. http://dx.doi.org/10.1103/RevModPhys.64.795.

[88] J.D. Meiss. Differential Dynamical Systems, volume 14 of Mathematical Modeling and Computation. Siam, Philadelphia, 2007.

[89] J.D. Meiss. Visual explorations of dynamics: the standard mapping. Pramana, Indian Academy of Sciences, 70:965–988, 2008. http://www.ias.ac.in/pramana/v70/p965/fulltext.pdf.

[90] J.D. Meiss. The destruction of tori in volume-preserving maps. Communications in Nonlinear Science and Numerical Simulation, 17:2108–2121, 2012. http://dx.doi.org/10.1016/j.cnsns.2011.04.014.

[91] I. Mezc. Break-up of invariant surfaces in action-angle-angle maps and flows. Phys. D, 154(1-2):51–67, 2001. http://dx.doi.org/10.1016/S0167-2789(01)00226-3.

[92] I. Mezc and Stephen Wiggins. A method for visualization of invariant sets of dynamical systems based on the ergodic partition. Chaos, 9(1):213–218, 1999. http://authors.library.caltech.edu/1939/1/MEZchaos99a.pdf.

[93] P. J. Morrison. Magnetic field lines, Hamiltonian dynamics, and nontwist systems. Phys. Plasmas, 7(6):2279–2289, 2000.

[94] J.K. Moser. On the theory of quasiperiodic motions. SIAM Review, 8:145–171, 1966. http://epubs.siam.org/sirev/resource/1/siread/v8/i2/p145_s1.

[95] N. Murray. Critical function for the standard map. Physica D, 52:220–245, 1991.

[96] A. Olvera and N.P. Petrov. Regularity properties of critical invariant circles of twist maps, and their universality. SIAM J. App. Math., 7:962–987, 2008. http://epubs.siam.org/doi/abs/10.1137/070687967.

[97] I.C. Percival. Variational principles for invariant tori and cantori. In M. Month and J.C. Herrera, editors, Nonlinear Dynamics and the Beam-Beam Interaction, volume 57, pages 302–310. Amer. Inst. Phys., New York, 1979.

[98] I.C. Percival. Chaotic boundary of a Hamiltonian map. Physica D, 6:67–77, 1982. http://dx.doi.org/10.1016/0167-2789(82)90005-7.

[99] O. Piro and M. Feingold. Diffusion in three-dimensional Liouvillian maps. Phys. Rev. Lett., 61:1799, 1988. http://dx.doi.org/10.1103/PhysRevLett.61.1799.

[100] J. Pöschel. A lecture on the classical KAM theorem. In Smooth ergodic theory and its applications (Seattle, WA 1999), volume 69 of Proc. Sympos. Pure Math., pages 707–732. Amer. Math. Soc., Providence, 2001.

[101] G.R.W. Quispel and H.W. Capel. Local reversibility in dynamical systems. Physica D, 112:112–116, 1998. http://dx.doi.org/10.1016/S0167-2789(97)00199-1.

[102] F. Rannou. Numerical study of discrete plane area-preserving mappings. Astron. and Astrophys., 31:289–301, 1974.

[103] J.A.G. Roberts and G.R.W. Quispel. Chaos and time reversal symmetry. order and chaos in reversible dynamical systems. Physics Letters A, 142(2-3):63–1177, 1989.

[104] G. Schmidt and J. Bialek. Fractal diagrams for hamiltonian stochasticity. Physica D, 5:397–404, 1982.

[105] M.B. Sevryuk. Reversible Systems, volume 1211 of Lecture Notes in Mathematics. Springer-Verlag, New York, 1986.

[106] S. Shinohara and Y. Aizawa. Indicators of reconnection processes and transition to global chaos in nontwist maps. Progress of Theoretical Physics, 100(2):219–233, 1998.

[107] G. Szerkeres. The search for the three dimensional approximation constant. In J.H. Loxton and A.J. Ven Der Poorten, editors, Diophantine Analysis, pages 139–146. Cambridge Univ. Press, Cambridge, 1986.

[108] J.D. Szezech, I. L. Caldas, S.R. Lopes, R.L. Viana, and P. J. Morrison. Transport properties in nontwist area-preserving maps. Chaos, 19(4):043108, 2009. http://dx.doi.org/10.1063/1.3247349.

[109] A. Thyagaraja and F.A. Haas. Representation of volume-preserving maps induced by solenoidal vector fields. Phys. Fluids, 28(3):1005–1007, 1985. http://dx.doi.org/10.1063/1.865093.

[110] S. Tompaidis. Approximation of invariant surfaces by periodic orbits in high-dimensional maps. some rigorous results. Exper. Math., 5:197–209, 1996. http://dx.doi.org/10.1080/10586458.1996.10504588.

[111] S. Tompaidis. Numerical study of invariant sets of a quasiperiodic perturbation of a symplectic map. Exper. Math., 5:211–230, 1996. http://dx.doi.org/10.1080/10586458.1996.10504589.

[112] S. Tompaidis. Approximation of invariant surfaces by periodic orbits in high-dimensional maps. In C Simó, editor, Hamiltonian systems with three or more degrees of freedom (S'Agaró, 1995), volume 533 of NATO Adv. Sci. Inst. Ser. C Math. Phys. Sci., pages 605–609. Kluwer Acad. Publ., Dordrecht, 1999.

[113] Lloyd N. Trefethen. Spectral Methods in MatLab. Software, Environments, Tools. SIAM, Philadelphia, PA, 2000.

[114] J.J.P. Veerman and F.M. Tangerman. Intersection properties of invariant manifolds in certain twist maps. Comm. Math. Phys., 139:245–265, 1991. http://dx.doi.org/10.1007/BF02352495.

[115] M.N. Vrahatis, H. Isliker, and T.C. Bountis. Structure and breakdown of invariant tori in a 4-D mapping model of accelerator dynamics. Int. J. Bif. and Chaos, 7(12):2707–2722, 1997. http://dx.doi.org/10.1142/S0218127497001825.

[116] J. Wilbrink. Erratic behavior of invariant circles in standard-like mappings. Phys. D, 26:358–368, 1987. http://dx.doi.org/10.1016/0167-2789(87)90235-1.

[117] J. Wilbrink. New fixed point of the renormalisation operator associated with the recurrence of invariant circles in generic hamiltonian maps. Nonlinearity, 3(3):567–584, 1990. http://dx.doi.org/10.1088/0951-7715/3/3/002.

[118] A. Wurm and K. Fuchss Portela. Breakup of shearless invariant tori in cubic and quartic nontwist maps. Communications in Nonlinear Science and Numerical Simulation, 2011. http://dx.doi.org/10.1016/j.cnsns.2011.03.008.

[119] Z. Xia. Existence of invariant tori in volume-preserving diffeomorphisms. Erg. Th. Dyn. Sys., 12(3):621–631, 1992. http://dx.doi.org/10.1017/S0143385700006969.

[120] J.L. Zhou, B. Hu, and Yi-Sui Sun. Universal behaviour on the break-up of the spiral mean torus. Chin. Phys. Lett, 18(12):1550–1553, 2001. http://dx.doi.org/10.1088/0256-307X/18/12/303.

[121] J.L. Zhou, B.B. Hu, and Y.-S. Sun. Break-up of three-frequency KAM tori: Determination of the critical parameters. Chinese Phys. Lett., 18(6):734–736, 2001. http://dx.doi.org/10.1088/0256-307X/18/12/303.

Appendix A

Reversors

Suppose that a map $f : M \to M$, with $M = \mathbb{T}^d \times \mathbb{R}^k$ is reversible with involutions S_1 and S_2, and let F be a lift of f to $\mathbb{R}^d \times \mathbb{R}^k$.

Note that if S is a reversor for f, then so is $S \circ f^t$ for any $t \in \mathbb{Z}$; indeed this follows because f^t is a symmetry of f. For the lift F, the translations (2.15) are also symmetries; consequently, the translation of a reversor S is also a reversor, $S \circ T_m$. Note that $S_i \circ T_m = T_{-m} \circ S_i$. These transformations generate a group

$$\langle S_1, S_2, F, T_m \rangle$$

that is contained in the reversing symmetry group of F whenever g is odd. For (2.12) with (2.7) and (2.11), the reversors were given in (2.20), This appears, as far as we know, to be the complete group.

The fixed set of S is

$$\mathrm{Fix}(S) = \{(x, z) : S(x, z) = (x, z)\} \tag{A.1}$$

As is well-known, every symmetric periodic orbit has points on the fixed sets.

Lemma 5. *If f has reversor S, then every symmetric orbit must have a point on either* $\mathrm{Fix}(S)$ *or* $\mathrm{Fix}(f \circ S)$.

Proof. Indeed, if $j = 2k$ is even then

$$(x_k, z_k) = f^{-k}(x_{2k}, z_{2k}) = f^{-k} \circ S(x_0, z_0) = S(x_k, z_k),$$

so that $(x_k, z_k) \in \mathrm{Fix}(S)$. If, on the other hand, $j = 2k - 1$ is odd, then

$$(x_k, z_k) = f^{-k+1} \circ S(x_0, z_0) = f \circ S(x_k, z_k),$$

so that $(x_k, z_k) \in \mathrm{Fix}(f \circ S)$. □

Even better, periodic orbits have points on two distinct symmetry curves separated by half of the period.

Lemma 6. *If $f : \mathbb{T}^d \times \mathbb{R}^k$ has a reversor S and Γ is a symmetric, (m, n)-periodic orbit of the lift F to the universal cover $\mathbb{R}^d \times \mathbb{R}^k$, then Γ has points on two fixed sets of reversors in the group generated by $\langle S, F, T_m \rangle$.*

Proof. Since Γ is symmetric, we can suppose that there is a point $(x_0, z_0) \in \Gamma \cap \mathrm{Fix}(S)$. When the period $n = 2\ell$ is even then, since $(x_{-\ell}, z_{-\ell}) = T_{-m}(x_\ell, z_\ell)$,

$$(x_\ell, z_\ell) = F^\ell(S(x_0, z_0)) = S(x_{-\ell}, z_{-\ell}) = S \circ T_{-m}(x_\ell, z_\ell);$$

thus $(x_\ell, z_\ell) \in \mathrm{Fix}(S \circ T_{-m})$. Similarly when $n = 2\ell - 1$ is odd, then since $(x_{-\ell+1}, z_{-\ell+1}) = T_{-m}(x_\ell, z_\ell)$,

$$(x_\ell, z_\ell) = F^\ell(S(x_0, z_0)) = F \circ S(x_{-\ell+1}, z_{-\ell+1}) = F \circ S \circ T_{-m}(x_\ell, z_\ell);$$

thus $(x_\ell, z_\ell) \in \mathrm{Fix}(F \circ S \circ T_{-m})$. □

If we denote the symmetry by S_1 and let $S_2 = f \circ S_1$, then, the lemmas imply that symmetric orbits can be found by looking for orbits that start on $\mathrm{Fix}(S_1)$ or $\mathrm{Fix}(S_2) \equiv \mathrm{Fix}(f \circ S_1)$, and "half" a period later end on one of the sets $\mathrm{Fix}(S_1 \circ T_{-m})$ or $\mathrm{Fix}(S_2 \circ T_{-m})$. The results are summarized in Table 2.1.

Appendix B

Generalized Farey Tree

The Farey tree is a recursive algorithm for generating all rationals between a given initial pair [56]. To do this, begin by regarding each $\omega \in \mathbb{R}_+$ as the direction $(\omega, 1)^T \in \mathbb{R}^2_+$ and each positive rational $\frac{m}{n}$ as the direction $(m, n)^T$. Conversely, for each vector $(u, v)^T \in \mathbb{R}^2_+$, there is an associated rotation number $\omega = u/v$. The problem of approximation is to then find a sequence of vectors $(m_\ell, n_\ell)^T$ that approach $(\omega, 1)^T$ in the sense that the two directions become parallel, i.e., $|n_\ell \omega - m_\ell| \to 0$ as $\ell \to \infty$.

The root of the Farey tree consists of the two vectors, $(0, 1)^T$ and $(1, 0)^T$, said to be at **level** zero. The interior of the cone of directions spanned by the positive linear combinations of these vectors thus represents all positive numbers. The set of directions can be mapped onto the segment of the line $u+v = 1$ in the positive quadrant, and each direction in the "level-zero" cone corresponds to a point on this segment as sketched in Fig. B.1. The next level is obtained with the mediant operation $\oplus$,

$$\begin{pmatrix} m \\ n \end{pmatrix} \oplus \begin{pmatrix} p \\ q \end{pmatrix} = \begin{pmatrix} m+p \\ n+q \end{pmatrix},$$

which is simply vector addition applied to the bounding vectors. Thus at level one there is one new **daughter** vector, $(1, 1)^T = (0, 1)^T \oplus (1, 0)^T$. The daughter divides the level-zero cone into two "level-one" cones

$$C_l = \begin{pmatrix} 1 & 0 \\ 1 & 1 \end{pmatrix}, \quad C_r = \begin{pmatrix} 1 & 1 \\ 0 & 1 \end{pmatrix},$$

where the columns represent the bounding vectors. This process can be repeated: each level-ℓ cone is divided by forming the mediant of its boundary pair. Thus the level-one cone C_l becomes the two cones C_lC_l and C_lC_r, and there are 2^ℓ cones at level ℓ.

The Farey tree is then the binary graph obtained by connecting each rational vector at level $\ell \geq 1$ with its two daughters at the next level. Each vertex has a unique **path**, $p \in \{l, r\}^{\mathbb{N}}$: the path to $(1,1)^T$ at level one is empty, and $p = l$ for the daughter $(1,2)^T$ to the "left" and $p = r$ for the daughter $(2,1)^T$ to the "right". Each level-ℓ parent has two level-$(\ell+1)$ daughters, whose paths are obtained by appending an l or r, respectively, to the parent's path. The vector corresponding to a path, $p = i_1\, i_2\, \ldots\, i_\ell$, $i_k \in \{l, r\}$ is then

$$\begin{pmatrix} m \\ n \end{pmatrix} = C_{i_1} C_{i_2} \ldots C_{i_\ell} \begin{pmatrix} 1 \\ 1 \end{pmatrix}.$$

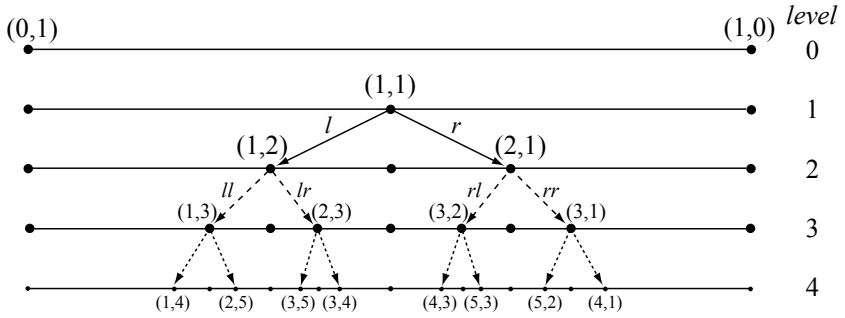

Figure B.1: First five levels of the Farey tree construction as the set of directions in the first quadrant projected onto the segment $x + y = 1$.

Since the matrices C_l and C_r are unimodular, the parallelogram formed from the two vectors bounding each cone has unit area. A consequence is that every vector on the Farey tree is coprime, $\gcd(m, n) = 1$. Moreover, each rational has a finite Farey path, and every irrational ω is obtained as the limit of an infinite path on the tree. For example, the golden mean has path $\phi = rlrlrlrl \ldots \equiv \overline{rl}$. There are also infinite paths that limit on each rational from above and below, these are the paths with infinite tails of l's and r's, respectively. There is also a simple relation between the continued fraction expansion and the Farey path, see e.g., [56].

Kim and Ostlund generalize the Farey tree to higher dimensions by regarding each vector $\omega \in \mathbb{R}^2_+$ as a direction $(\omega, 1)^T \in \mathbb{R}^3_+$ [64]. We will take the level-zero cone to be the positive octant, generated by positive linear combinations of the triplet $(1,0,0)^T$, $(0,1,0)^T$, $(0,0,1)^T$. The intersection of the cone $(u,v,w)^T \in \mathbb{R}^3_+$ with the plane $u+v+w=1$ is the equilateral triangle sketched in Fig. B.2(a). Somewhat arbitrarily, the level-one child is defined to be the mediant of two of the bounding, parent vectors; we choose $(1,1,0)^T = (1,0,0)^T \oplus (0,1,0)^T$. This creates a pair of level-one cones bounded by the child and the two parents that form an independent triplet, that is the cones

$$C_l = \begin{pmatrix} 0 & 0 & 1 \\ 1 & 0 & 1 \\ 0 & 1 & 0 \end{pmatrix}, \quad C_r = \begin{pmatrix} 0 & 1 & 1 \\ 0 & 0 & 1 \\ 1 & 0 & 0 \end{pmatrix}. \tag{B.1}$$

As shown in Fig. B.2(a), the line connecting the unused parent, $(0,0,1)^T$ to the child, $(1,1,0)^T$ divides the equilateral triangle into "left" and "right" triangles. To continue the process, a new child in each cone is obtained by applying the mediant operation to the two oldest parents (those generated from the earliest levels), and each cone is divided into two, using the resonance line connecting the child and its youngest parent. The construction up to level three is shown in Fig. B.2(a).

Projecting the cones onto the plane $w=1$ gives the frequency plane, as shown in Fig. B.2b. Each point ω in this plane represents a direction $(\omega, 1)$; here we show only rotation vectors within the unit square $[0,1]\times[0,1]$; these correspond to directions in the cones rrl and llr of the full tree.

This binary, recursive procedure assigns a path $p \in \{l,r\}^{\mathbb{N}}$ to each vertex below level one by following the sequence of dividing lines from $(1,1,0)^T$: a turn to the "right" appends an r to the path and a turn to the left, an l. Thus, for example the path rrr corresponds to $(2,1,1)^T$ and lrl to $(0,2,1)^T$. Just as for the Farey tree, the vector corresponding to a path p is

$$\begin{pmatrix} m_1 \\ m_2 \\ n \end{pmatrix} = C_{i_1} C_{i_2} \ldots C_{i_\ell} \begin{pmatrix} 1 \\ 1 \\ 0 \end{pmatrix}, \tag{B.2}$$

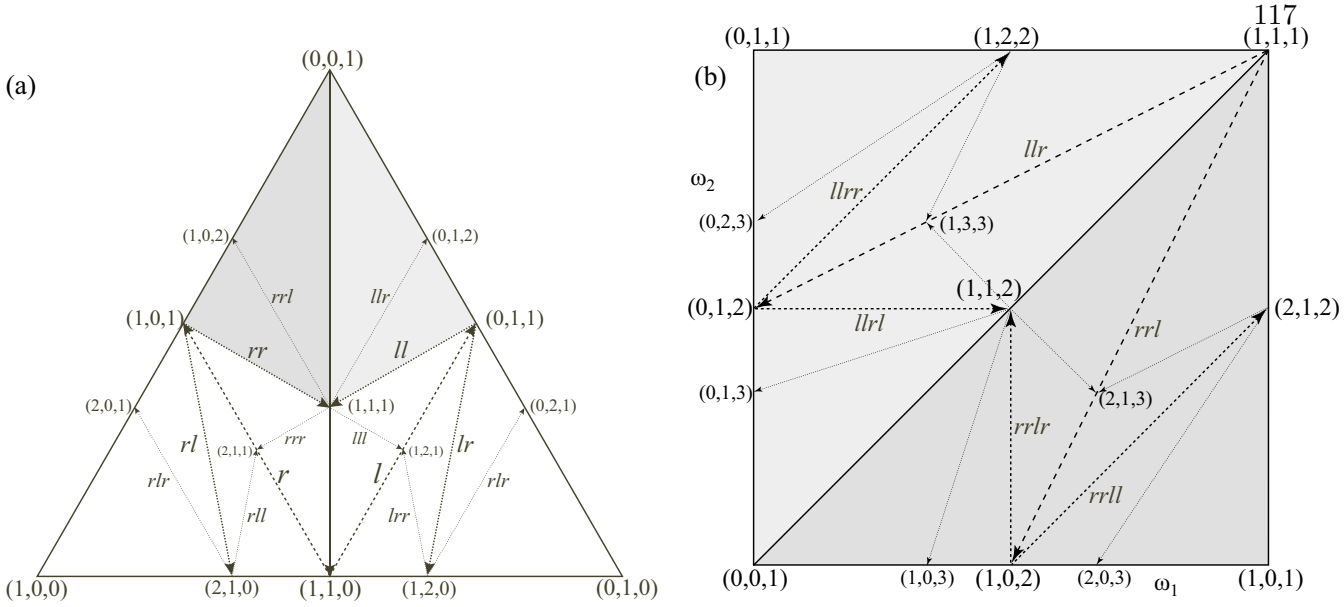

Figure B.2: (a) First three levels of the generalized Farey tree projected on the plane $x+y+z=1$ in homogeneous coordinates. The two shaded triangles correspond to rotation vectors in $[0,1]^2$. (b) Projection of the two level-three cones, rrl and llr, onto the plane $w=1$, and three additional levels of the tree.

using the matrices (B.1).

Since the matrices C_i are unimodular, the three vectors that bound each cone define a parallelepiped with volume one. A consequence is that every vector on the tree is coprime, $\gcd(m_1, m_2, n) = 1$. Moreover it can be shown that every coprime vector in the positive octant has a finite path on the tree. One defect of this construction, however, is that every integer vector in the interior of the positive octant has two finite paths; for example, $rrlll$ and $rrlrr$ both lead to $(2,1,3)^T$.[1] Just as for the Farey tree, however, every incommensurate direction has a unique, infinite path. There are also infinite paths that limit on rational directions; for example, any path $p = h\overline{lr}$ with a periodic lr tail and arbitrary head h.

Accounting for the duplication, there are

$$2^\ell + [5 - (-1)^l]2^{\lfloor \frac{\ell}{2} \rfloor - 1} + 1$$

unique directions on the tree up to level ℓ (including the initial triplet). In Fig. 2.7(a) we show

[1] If (m,n) lies on a level-ℓ dividing line then its two paths are those obtained by exchanging l and r for all entries beyond level ℓ.

the 2140 unique rotation vectors in the rrl and llr cones up to level 13. The boundaries of each cone at each level correspond to resonances $p \cdot \omega = q$, and these give rise to the isolated lines in the figure. Just as for the Farey tree, the sampling of rotation vectors is nonuniform, tending to avoid low-order resonances.

Appendix C

Algebraic Fields

KAM theory suggests that the most robust invariant tori should have Diophantine rotation vectors. One way to construct these is to use integral bases of algebraic fields. Recall that $\alpha \in \mathbb{C}$ is an **algebraic number** of degree n if it is a root of an n^{th}-degree polynomial with rational coefficients, but not of any such polynomial of lower degree. The **algebraic field** generated by α is

$$\mathbb{Q}(\alpha) = \left\{ \sum_{i=0}^{n-1} a_i \alpha^i : a_i \in \mathbb{Q} \right\}.$$

For example, the golden mean ϕ, the larger root of $\phi^2 - \phi - 1 = 0$, is a quadratic irrational and $\mathbb{Q}(\phi) = \{a + b\phi : a, b \in \mathbb{Q}\}$. The ring of integers $\mathbb{Z}(\alpha) \subset \mathbb{Q}(\alpha)$ consists of those elements that are roots of monic polynomials, $x^n + p_1 x^{n-1} + \ldots + p_n$, with $p_i \in \mathbb{Z}$. The ring is an n-dimensional vector space over $\mathbb{Z}$, and a basis $\{\alpha_1, \ldots, \alpha_n\}$ for this space is called an **integral basis**. In general, integral bases give rise to Diophantine rotation vectors.

Theorem 7 ([23, 31]). *If $(\omega, 1) \in \mathbb{R}^{d+1}$ is an integral basis of a real algebraic field of degree $d+1$, then $\omega \in \mathcal{D}_d$.*

For example, $(\phi, 1)$ is a basis for $\mathbb{Q}(\phi)$, thus $\mathbb{Z}(\phi) = \{q\phi + p : q, p \in \mathbb{Z}\}$. Every integral basis for $\mathbb{Z}(\phi)$ is of the form $(\alpha_1, \alpha_2) = (\phi, 1)M$, where $M \in SL(2, \mathbb{Z})$. The ratios, $\omega = \alpha_1/\alpha_2$ of these integral bases are precisely the noble numbers, conjectured to correspond to the locally most robust invariant circles of twist maps.

As discussed in §2.5.1, we study the cubic field $\mathbb{Q}(\sigma)$ generated by the real solution σ of

(2.28). We will denote the three roots of (2.28) by $(\sigma_0, \sigma_1, \sigma_2)$; here

$$\begin{aligned} \sigma = \sigma_0 &\approx 1.3247179572447460, \\ \sigma_{1,2} = \frac{1}{\sqrt{\sigma}} e^{\pm i\theta}, &\quad \theta = \arccos\left(-\tfrac{1}{2}\sigma^{\frac{3}{2}}\right) \approx 2.437734932288317. \end{aligned} \tag{C.1}$$

The spiral mean, like ϕ, is a "Pisot-Vijayaraghavan" (PV) number: a root of a monic polynomial with exactly one root outside the unit circle. Indeed, ϕ and σ are the smallest quadratic and cubic PV numbers, respectively. The discriminant of (2.28) is square-free, $\Delta = -23$, so the set $\{\sigma^2, \sigma, 1\}$ is an integral basis for the cubic field $\mathbb{Q}(\sigma)$.

For our purposes, it is providential that the integer ring $\mathbb{Z}(\sigma)$ is naturally related to the generalized Farey tree construction of App. B. Indeed the polynomial (2.28) is the characteristic polynomial for both cone matrices C_l and C_r of (B.1), and their maximal eigenvectors,

$$v_{\bar{l}} = \begin{pmatrix} 1 \\ \sigma^2 \\ \sigma \end{pmatrix}, \quad v_{\bar{r}} = \begin{pmatrix} \sigma^2 \\ 1 \\ \sigma \end{pmatrix}, \tag{C.2}$$

are in $\mathbb{Z}(\sigma)$. Moreover, since every entry of the fifth powers of both matrices (B.1) is positive, these matrices are irreducible in the Perron-Frobenius sense. As a consequence, for any $v \in \mathbb{R}^3_+$, $C_i^\ell v \to c\sigma^\ell v_i$ as $\ell \to \infty$. Thus by (B.2), the directions $v_{\bar{l}}$ and $v_{\bar{r}}$ correspond to the paths $p = l^\infty \equiv \bar{l}$ and $r^\infty \equiv \bar{r}$, respectively.

As an example, the sequence of integer vectors (m_ℓ, n_ℓ) with paths $p = r^\ell$ are

$$\begin{pmatrix} 1 \\ 1 \\ 0 \end{pmatrix}, \begin{pmatrix} 1 \\ 0 \\ 1 \end{pmatrix}, \begin{pmatrix} 1 \\ 1 \\ 1 \end{pmatrix}, \begin{pmatrix} 2 \\ 1 \\ 1 \end{pmatrix}, \begin{pmatrix} 2 \\ 1 \\ 2 \end{pmatrix}, \begin{pmatrix} 3 \\ 2 \\ 2 \end{pmatrix}, \begin{pmatrix} 4 \\ 2 \\ 3 \end{pmatrix}, \ldots, \begin{pmatrix} n_{\ell+1} \\ n_{\ell-1} \\ n_\ell \end{pmatrix} \cdots. \tag{C.3}$$

It is not hard to see that the sequence of periods $\{n_0, n_1, \ldots\}$ satisfies the recurrence

$$n_{\ell+3} = n_{\ell+1} + n_\ell, \quad n_0 = 0,\ n_1 = n_2 = 1, \tag{C.4}$$

which has the solution

$$\begin{aligned} n_\ell &= a_0\sigma^\ell + a_1\sigma_1^\ell + a_2\sigma_2^\ell, \\ a_i &= \tfrac{1}{23}(3\sigma_i^2 + 7\sigma_i - 2). \end{aligned} \tag{C.5}$$

The directions of Farey sequence (C.3), $m_\ell/n_\ell = (n_{\ell+1}/n_\ell, n_{\ell-1}/n_\ell)$, limit on the rotation vector

$$\omega = (\sigma, 1/\sigma) = (\sigma, \sigma^2 - 1).$$

Unlike the equivalent sequence for the golden mean, these successive approximants include rotation vectors that are not "best" approximants to ω. Recall that a rational m/n is a best approximant to ω if

$$\|n\omega - m\| = \min_{0<q\leq n} \min_{p\in\mathbb{Z}^d} \|q\omega - p\| \tag{C.6}$$

for some norm $\|\ \|$. The sequence of best approximants depends upon the choice of norm and, unlike the classical Farey tree, it is not known if the generalized Farey tree gives all of the best approximants. However, up to period $50,000$, the best approximants to $v_{\bar{r}}$ in the 1, 2 and ∞ norms are the same; they have the periods

$$n_\ell \in \{1, 3, 9, 12, 37, 114, 151, 465, 1432, 1897, 5482, 17991, 23833\}.$$

Moreover, we found that all of the best approximants for these three norms can be found in the Farey sequence (C.3) up to at least period 10^6.

Appendix D

Application of Greene's Residue Criteria for Area-Preserving Maps

Greene conjectured that periodic orbits in the neighborhood of an invariant circle should be stable. Indeed, a sequence of periodic orbits should limit upon a circle only if their Lyapunov exponents converge to zero. Conversely, if the limit of a family of periodic orbits has nonzero Lyapunov exponents, then the invariant circle should no longer exist. This method is known as **Greene's residue criterion**. Although initially presented as a conjecture, some aspects of it have been rigorously proven [77, 44, 38].

A type-(m, n) periodic orbit of f is an orbit of the lift, $(x_{t+1}, y_{t+1}) = F(x_t, y_t)$, such that $(x_n, y_n) = (x_0 + m, y_0)$. When f is area-preserving, the product of the multipliers of any periodic orbit must be 1. The stability of a periodic orbit is therefore completely determined by the trace of the Jacobian Df. Greene characterized this stability through a quantity he called the **residue**

$$R = \tfrac{1}{4}(2 - \mathrm{tr}(Df^n(x_0, y_0)).$$

If $0 < R < 1$, the orbit is linearly stable.

Greene conjectured that an invariant circle with rotation number ω will exist if and only if the residues R_j of a sequence of type (m_j, n_j) periodic orbits that approximate the circle,

$$\lim_{j\to\infty} \frac{m_j}{n_j} = \omega,$$

are bounded:

$$\lim_{j\to\infty} |R_j| \leq \infty.$$

Rational sequences that approximate ω can be obtained by truncating either the Farey tree or continued fraction expansion of ω, recall App. B. To implement the criterion, we compute each periodic orbit using a root-finding method and continuation in ε. This computation is simplified when the map is reversible, see App. E, since the computation can be reduced to a one-dimensional secant method. A threshold residue, R^{th}, is selected, and the parameter value ε_j^{th}, such that $|R_j| = R^{th}$ is found, also using the secant method. The choice of R^{th} is arbitrary; however Greene found that for the golden mean, convergence was fastest with the choice $R^{th} = 0.25$ [54]. This is the value we use.

The approximation of ε_{cr} can be improved by extrapolation. The renormalization theory implies that for noble circles of twist maps,

$$\varepsilon_j^{th} \sim \varepsilon_{cr} - A\delta^{-j},$$

for some constants A and δ [78]. This leads to a three-point extrapolation scheme: given three sequential approximants, we estimate

$$\begin{aligned}
\delta &= \frac{\varepsilon_j^{th} - \varepsilon_{j-1}^{th}}{\varepsilon_{j+1}^{th} - \varepsilon_j^{th}}, \\
A &= \frac{\delta^{j+1}}{\delta - 1}(\varepsilon_{j+1}^{th} - \varepsilon_j^{th}), \\
\varepsilon_{cr} &= \varepsilon_j^{th} + A\delta^{-j}.
\end{aligned}$$

Extrapolation significantly improves the accuracy of the estimation of the critical parameter. For orbits up to period 30000, the values of ε_j^{th} generally converged to $3-4$ digits, but after extrapolation, the last several estimates of ε_{cr} agreed to $4-8$ digits.

Appendix E

Symmetries and Reversors of the Generalized Standard Map

In this appendix, we recall some of the symmetries and reversors of the generalized standard map (1.9). Of course, any map f is a symmetry of itself. In addition, when f is a map on the cylinder, it commutes with integral rotations. Specifically, if

$$T_{m,n}(x,y) = (x+m, y+n), \quad m,n \in \mathbb{Z}$$

then $T_{1,0}$ is a symmetry of f, or more properly of its lift, F, to the universal cover obtained by letting $x \in \mathbb{R}$. Since the composition of two symmetries is also a symmetry, $F^k \circ T_{m,0}$ is also a symmetry of F.

Certain special cases of (1.9) have additional symmetries and reversors. We say that a function g is odd about α if

$$g(\alpha + x) = -g(\alpha - x), \text{ (odd about } \alpha).$$

If the force in (1.9) is odd, then this map is reversed by the involution

$$S_1(x,y) = (2\alpha - x, y + \varepsilon g(x)). \tag{E.1}$$

Note that when g is periodic and odd about α, then it is also odd about $\frac{1}{2} + \alpha$; the corresponding reversor is $T_{1,0} \circ S_1$. Since is the line $x = \alpha$, Every rotational invariant circle intersects $\mathrm{Fix}(S_1) = \{(\alpha, y) : y \in \mathbb{R}\}$; the consequences for the conjugacy are discussed in App. F. Cases studied in this paper with this reversor are shown in Table E.1.

Similarly, if the frequency map Ω is odd about a point β, then (1.9) is reversible under the involution

$$S_2(x, y) = (x, 2\beta - y - \varepsilon g(x)), \tag{E.2}$$

This reversor maps an invariant circle with rotation number ω onto one with rotation number $-\omega$. A consequence is that these circles have the same critical parameter set: $\varepsilon_{cr}(-\omega) = \varepsilon_{cr}(\omega)$.

Chirikov's standard map, (1.9) using (1.11) and (1.15), has both sets of reversors since Ω and g are both odd about zero ($\alpha = \beta = 0$): it is "doubly reversible." Another way of viewing this is to note that this map has the inversion $I_1(x, y) = (2\alpha - x, 2\beta - y)$ as a symmetry. This is not independent of the reversors since $I = S_1 \circ S_2$.

An additional symmetry of maps, like Chirikov's map, with $\Omega(y) = y$ is a translation symmetry in the momentum direction: f commutes with the vertical translation $T_{0,1}$. A consequence is that $\varepsilon_{cr}(\omega) = \varepsilon_{cr}(\omega + n)$ for integer n. Combining this with the inversion implies that for Chirikov's map, $\varepsilon_{cr}(\omega) = \varepsilon_{cr}(1 - \omega)$; thus, one can limit the rotation numbers studied to $\omega \in [0, \frac{1}{2}]$. The known symmetries of Chirikov's map are summarized in the first line of Table E.1.

The map (1.9) also has a reversor when **both** g and Ω are even, e.g.,

$$g(\alpha + x) = g(\alpha - x), \text{ (even about } \alpha).$$

When g is even about α **and** Ω is even about β, (1.9) has the reversor

$$S_3(x, y) = (2\alpha - x, 2\beta - y - \varepsilon g(x)) \tag{E.3}$$

Note that this reversor is orientation preserving, and its fixed set is a point. This reversor maps an invariant circle with rotation number ω and positive twist is onto a circle with the same rotation number but negative twist. Examples that we study, recall Table E.1, include the nontwist maps with Ω_2, which is even about 0, and forces g_1 or g_3, which are even about $\frac{1}{4}$ and $\frac{3}{4}$.

Finally, when Ω is even and g has the odd-translation symmetry, $g(x + \frac{1}{2}) = -g(x)$, the map (1.9) commutes with the symmetry

$$I_2(x, y) = (x + \tfrac{1}{2}, -y). \tag{E.4}$$

This is the case for the standard nontwist map, i.e., using the Chirikov's force (1.15), and the frequency map (1.16). This symmetry was exploited in many studies of the breakup of shearless tori [106].

When none of the above symmetries of g and/or Ω hold, then the map (1.9) is, as far as we know, not reversible, and its complete symmetry group is $\langle f, T_{1,0} \rangle$. One example of this is due to Rannou [102]; however, while it is conjectured that this map is not reversible [78, 103], as far as we know this question is still open.

	Map					$\mathcal{G}$	
Force	Odd	Even	Ω	Odd	Even	Reversors	Symmetries
g_1	$0, \frac{1}{2}$	$\frac{1}{4}, \frac{3}{4}$	Ω_1	0		S_1, S_2	$I_1, T_{0,1}$
			Ω_2		0	S_1, S_3	I_2
g_2	$0, \frac{1}{2}$		Ω_1	0		S_1, S_2	$I_1, T_{0,1}$
			Ω_2		0	S_1	
g_3		$\frac{1}{4}, \frac{3}{4}$	Ω_1	0		S_2	$T_{0,1}$
			Ω_2		0	S_3	
g_4			Ω_1	0		S_2	$T_{0,1}$
			Ω_3				
g_5			Ω_1	0		S_2	$T_{0,1}$

Table E.1: Known generators of the reversing symmetry groups for various maps of the standard form (1.9), with forces g_1, (1.15), g_2, (4.2), and g_3, (4.3), and frequency maps Ω_1, (1.11), Ω_2, (1.16), and Ω_3, (4.4). The "odd" and "even" columns give the points about which the functions are odd or even, if any. The "trivial" symmetries f and $T_{1,0}$ are omitted.

Appendix F

Symmetries of the Conjugacy

Recall that a homeomorphism S is a symmetry of f if $f \circ S = S \circ f$, and is a reversor if $f \circ S = S \circ f^{-1}$. The collection of reversors and symmetries of f is its reversing-symmetry group $\mathcal{G}$ [69]. Symmetries or reversors act on the conjugacy k to produce additional conjugacies [96].

Lemma 8. *Suppose that $k : \mathbb{S} \to M$ is a conjugacy (3.1) for $f : M \to M$ with rotation number ω. Then if S is a symmetry of f, $\tilde{k} = S \circ k$ also solves (3.1), and if S is a reversor, $\tilde{k} = S \circ k \circ R$ solves (3.1), where $R(\theta) = -\theta$.*

Proof. When S is a symmetry, (3.1) implies that

$$f \circ S \circ k = S \circ f \circ k = S \circ k \circ T_\omega.$$

Thus $\tilde{k} = S \circ k$ is also a solution to (3.1). When S is a reversor, then the inverse of (3.1) implies

$$f \circ S \circ k \circ R = S \circ f^{-1} \circ k \circ R = S \circ k \circ T_{-\omega} \circ R = S \circ k \circ R \circ T_\omega.$$

Thus $\tilde{k} = S \circ k \circ R$ solves (3.1).

□

A symmetry or a reversor may map one invariant torus onto another, but if it maps a circle onto itself, then Lem. 8 and Lem. 4 imply that the conjugacy itself is symmetric up to a shift. One simple reversible example corresponds to the map (1.9) when g is odd, see App. E.

Corollary 9. *When (1.9) is a twist map, g is odd about α, k is a continuous conjugacy, and ω is irrational, then there is a φ such that $k_x - \alpha$ is odd about φ, and k_z is even about $\varphi + \frac{1}{2}\omega$.*

Proof. For this case we use the reversor (E.1) of App. E. The new conjugacy given by Lem. 8,

$$\tilde{k}(\theta) = S_1 \circ k(-\theta) = (2\alpha - k_x(-\theta), k_z(-\theta) + \varepsilon g(k_x(-\theta))\,, \tag{F.1}$$

is continuous and has degree-one, so that $\tilde{k}(\mathbb{S})$ is an invariant circle of f with rotation number ω. When (1.9) is a twist map, it has at most one rotational invariant circle for each ω, therefore $\tilde{k}(\mathbb{S}) = k(\mathbb{S})$, and Lem. 4 thus implies that $\tilde{k}(\theta) = k(\theta + 2\varphi)$ for some φ.

Consequently, the x-coordinate of (F.1) gives

$$k_x(\theta + 2\varphi) = 2\alpha - k_x(-\theta).$$

Setting $\xi = \theta + \varphi$, then gives $k_x(\varphi + \xi) - \alpha = -(k_x(\varphi - \xi) - \alpha)$; therefore, $k_x - \alpha$ is odd about φ.

Since the composition of a symmetry and a reversor is a reversor, a second reversor for (1.9) is $f(S_1(x, z)) = (2\alpha - x + z, z)$. Composing (F.1), with f and using (3.1) this gives

$$\tilde{k}(\theta + \omega) = f(\tilde{k}(\theta)) = (f \circ S_1)(k(-\theta)).$$

Again using $\tilde{k}(\theta) = k(\theta + 2\varphi)$, the z-component of the above equation gives $k_z(\theta + \omega + 2\varphi) = k_z(-\theta)$, which implies the evenness assertion. □

A similar relation holds for the map (2.12) with g given by (2.11).

Corollary 10. *When k is a continuous conjugacy for (2.12) such that the force g is odd about 0, and ω is irrational, then there is a $\varphi \in \mathbb{R}^2$ such that k_x and k_y are odd about φ, and k_z is even about $\varphi + \frac{1}{2}\omega$.*

Proof. For this case we use the reversor S_1 from (2.20). The new conjugacy given by Lem. 8,

$$\tilde{k}(\theta) = S_1 \circ k(-\theta) = (-k_x(-\theta), k_z(-\theta) - \varepsilon g(k_x(-\theta), k_y(-\theta))\,, \tag{F.2}$$

is continuous and has degree-one, so that $\tilde{k}(\mathbb{S})$ is an invariant torus of f with rotation number ω. (2.12) has at most one rotational invariant torus for each ω, therefore $\tilde{k}(\mathbb{S}) = k(\mathbb{S})$, and Lem. 4 thus implies that $\tilde{k}(\theta) = k(\theta + 2\varphi)$ for some φ.

Consequently, the x and y coordinates of (F.2) give

$$k_x(\theta + 2\varphi) = -k_x(-\theta),$$

$$k_y(\theta + 2\varphi) = -k_y(-\theta)$$

Setting $\xi = \theta + \varphi$, then gives

$$k_x(\varphi + \xi) = -(k_x(\varphi - \xi)),$$

$$k_y(\varphi + \xi) = -(k_y(\varphi - \xi))$$

therefore, k_x and k_y are odd about φ.

Since the composition of a symmetry and a reversor is a reversor, a second reversor for (2.12) is $f(S_1(x, z)) = (-x + z, z)$. Composing (F.1), with f and using (3.1) this gives

$$\tilde{k}(\theta + \omega) = f(\tilde{k}(\theta)) = (f \circ S_1)(k(-\theta)).$$

Again using $\tilde{k}(\theta) = k(\theta+2\varphi)$, the z-component of the above equation gives $k_z(\theta+\omega+2\varphi) = k_z(-\theta)$, which implies the evenness assertion. □

We will use these results as a numerical check on our solutions of (3.1). While is seems difficult to check that a function is "odd" or "even" about some unknown point φ, the Fourier coefficients of such a conjugacy, (3.2), must obey

$$\begin{aligned} \hat{k}_{x0} &= \alpha - \varphi, \\ \Re(\hat{k}_{xj} e^{2i\pi j\varphi}) &= 0, \\ \Im(\hat{k}_{zj} e^{2i\pi j(\varphi+\frac{1}{2}\omega)}) &= 0, \end{aligned} \tag{F.3}$$

for (1.9) and

$$\begin{aligned} \hat{k}_{x0} &= -\varphi_1, \\ \hat{k}_{y0} &= -\varphi_2, \\ \Re(\hat{k}_{xj} e^{2i\pi j\cdot\varphi}) &= 0, \\ \Re(\hat{k}_{yj} e^{2i\pi j\cdot\varphi}) &= 0, \\ \Im(\hat{k}_{zj} e^{2i\pi j\cdot(\varphi+\frac{1}{2}\omega)}) &= 0, \end{aligned} \tag{F.4}$$

for (2.12).